4-12-2005

Detection of Residual Stress in Multi-Crystalline Silicon Wafers Using Swept-Sine Frequency Response Data

Shawn R. Best
University of South Florida

Detection of Residual Stress in Multi-Crystalline Silicon Wafers

Using Swept-Sine Frequency Response Data

by

Shawn R. Best

A thesis submitted in partial fulfillment
of the requirements for the degree of
Master of Science in Mechanical Engineering
Department of Mechanical Engineering
College of Engineering
University of South Florida

Major Professor: Daniel P. Hess, Ph.D.
Glen Besterfield, Ph.D.
Tom Eason, Ph.D.

Date of Approval:
April 12, 2005

Keywords: audible, modes, resonance, photovoltaic, rectangular

ACKNOWLEDGMENT

I would like to thank Dr. Daniel P. Hess, Ph.D. for taking me as his graduate student and providing me with the tools and guidance to accomplish my goals as a Master's student at the University of South Florida. I would like to thank Sue Britten and Shirley Trevort of Mechanical Engineering for always being there to lend a helping hand. I would like to thank Dr. Glen Besterfield, Ph.D. for constantly reminding me that my education is priority number one and for leading me into the career that I possess today. I would like to thank the professors of the Mechanical Engineering Department of the University of South Florida for giving me the tools and skills to succeed as an engineer. I would like to thank Robert Smith and Tom Gage of the Engineering Machine Shop for all of their help and assistance. I would like to thank Dr. Serguei Ostapenko, Ph.D. for his support in completing this thesis.

I would like to acknowledge BP Solar and RWE Schott Solar Inc. for their role in my thesis. This work was supported in part by DOE/NREL subcontract AAT-2-31605-06.

TABLE OF CONTENTS

LIST OF TABLES

LIST OF FIGURES

DETECTION OF RESIDUAL STRESS IN MULTI-CRYSTALLINE SILICON WAFERS USING SWEPT-SINE FREQUENCY RESPONSE DATA

Shawn R. Best

ABSTRACT

This thesis presents audible vibratory mode data obtained by mechanically exciting acoustic modes in mc-Si wafers grown by EFG technique with various levels and distributions of residual stress. Stress maps obtained using scanning infrared polariscopy are presented, illustrating the variation of residual stress.

Modal analyses of the wafers are performed using the finite element method and are in remarkably good agreement with the measured frequency response data. The calculated mode shapes were further validated through classic Chladni type patterns.

The vibratory data is found to correlate with the residual stress measurements. The data is fit with both linear and quadratic models with correlation coefficients of 0.8. The results reveal a dependence of wafer audible mode frequencies on residual stress level that may be useful for solar cell mechanical quality control and breakage inspection.

CHAPTER 1

INTRODUCTION

1.1 Overview

The extraordinary growth of the photovoltaic market over the past decade has sparked interest in the manufacturing and defect analysis of silicon wafers, the fundamental building block of solar cells. The silicon wafers of interest, as pertaining to this thesis, are boron doped multi-crystalline silicon (mc-Si) wafers grown by Edge-defined Film-fed Growth (EFG) technique. These wafers have the possibility of meeting both requirements set forth by the photovoltaic industry of low-cost production and high efficiency.

1.2 Background

In the production of multi-crystalline silicon (mc-Si) ribbons and tubes, applied thermo-elastic stress may exceed levels of 100 MPa. The residual stress level and its spatial distribution in wafers cut from the ribbons depend on growth speed, thickness, and temperature gradients present during growth [1]. Additional stress may arise in wafers when processing into solar cells, e.g., from bulk defect precipitates, thin film deposition such as a Si_3N_4 anti-reflecting coating, Al-backside contact firing, and wafer handling. Such stresses create slip dislocations, which alter wafer stiffness, thus enhancing wafer breakage and yield reduction in solar cell production lines potentially costing millions over a years span. Specifically for wafers used in solar cell applications, this stress

promotes various types of defect reactions, such as precipitation of residual impurities at dislocations, which deteriorate the electronic quality of the solar-grade mc-Si wafers [2].

There exists a need in the solar cell industry for methods of non-contact and non-destructive in-line and off-line monitoring of wafer residual stresses in as-grown as well as processed mc-Si wafers. Scanning optical polariscopy, X-ray diffraction, TEM and micro-Raman spectroscopy have been used with some success [3] as well as scanning infrared polariscopy based on the photo-elastic effect in stressed solids [4]. Laser measurement of the change in wafer curvature resulting from process steps such as thin film deposition has also been used to assess residual stress [5]. More recently, ultrasonics has been investigated for use in real-time diagnostics of defects in Cz-Si and mc-Si wafers [6, 7].

1.3 Thesis Outline

In this thesis, audible vibratory modes of mc-Si wafers arising from mechanical excitations of the wafer are used to diagnose residual stress. Chapter 2 describes the test apparatus and equipment used in this thesis, and explains the test procedure for performing the tests. Chapter 2 also gives general background information on frequency response and coherence. The test specimens used in this thesis are described in Chapter 3 and illustrates representative stress maps and frequency response plots of the wafers. The data extracted from the frequency response plots is analyzed and discussed in Chapter 3. The conclusions are found in Chapter 4 and the references and appendices follow.

CHAPTER 2

TEST APPARATUS AND EXPERIMENTS

2.1 Introduction

This chapter describes the test apparatus which consists of the test fixture and test equipment. Following those descriptions is the test procedure used for this thesis. Frequency response and coherence are also explained to help the reader understand the data presented.

The residual stress associated with the mc-Si wafers is thought to have a direct effect on the stiffness of the wafer. If this hypothesis is true, and knowing that stiffness directly affects the frequency response of an object, the stress would also have an effect on the frequency response and mode shapes of the wafers. To test this hypothesis, the residual stress of each wafer was measured using Scanning Infrared Polariscopy. Next, the frequency response and coherence of each wafer was measured and then compared to the residual stress data.

2.2 Test Apparatus

The vibration measurement test setup is illustrated in Figure 1. The test fixture is a custom part machined out of aluminum 6061-T6 with a Danco Company #74 o-ring (Stock #35719B) attached with super glue at the fixture and test wafer interface. The rubber o-ring between the aluminum fixture and the test specimen is needed due to the lack of flatness inherent to the wafers. Without the o-ring, the wafers would move bilaterally atop the fixture causing chatter, thus leading to unusable data. The o-ring adds

damping to the system, but its effect on the frequency response of the wafers was found to be constant. The aluminum fixture is fitted with a 3/8" x ¼" I.D. hose barb to MIP adapter. The adapter and o-ring combination are used to secure the test specimen to the fixture using a one phase induction motor vacuum pump (SaveVac 85) and Tygon Laboratory and Vacuum Tubing Formulation R-3603 (Part Number AAC00029). This allows us to secure the test specimen to the fixture without constraining the edges of the specimen.

The aluminum fixture is mounted onto an electrodynamic vibration generator, (Vibration Test Systems model number VG 100M-4 vibrator with trunion). The electromagnetic vibration generator, also referred to as a shaker, is fitted with a Low Noise B-1 Blower which is used to keep the shaker coil cool. The blower is incorporated with a sound absorption system to reduce its noise level.

A piezoelectric accelerometer (PCB Piezotronics Model #333B32) is mounted onto the fixture for shaker control. Its range of operation is between 0.5-3000 Hz and its sensitivity is 94.5 mV/g. The sensitivity of the accelerometer is entered into the SigLab software so that the signal can be converted to useful measurements. The accelerometer is connected to input channel 1 and is used as the reference value when calculating frequency response.

A sound level meter (Quest Technologies Model 2900) is mounted to a tripod and positioned 2cm +/- 0.2cm above the test specimen to record the audible modes. The sound level meter has a full output range of +/- 5 V_{pk} (3.16 V_{rms}). The sound level meter is limited in its function as it can only be set to read sound pressure for a 60 dB range. Since we are interested in the peak amplitudes, the microphone is set to read 60-120 dB.

With this being said, the sensitivity of the sound level meter is 5V/120 dB. This sensitivity is used in the SigLab software to convert the sound level meter signal to decibels. A 6ft shielded, 1/8" mono miniplug to RCA phono plug, fitted with a gold-plated RF adapter (accepts phono plug, fits BNC jack) is plugged into the sound level meter AC output and runs to input channel 3 of the SigLab hardware. The measurement from the sound level meter is the output of our test specimens and is referred to as the Response Channel.

A SigLab dynamic signal analyzer (DSP/MTS Technology Inc. Model 20-42) used in conjunction with SigLab and MatLab R12 software (DSP/MTS Technology Inc.) is used to apply a swept-sine input to the test specimen and to record the fixture input acceleration and the resulting sound pressure response. The analyzer consists of 4 input channels and 2 output channels. All the channels are fitted with BNC connections. The analyzer calculates the frequency response with the fixture acceleration defined as the input (reference channel) and the sound pressure as the output (response channel).

The output of the dynamic signal analyzer must be amplified in order to apply the correct amount of voltage to the shaker. A Techron Power Supply Amplifier (Model #7541) is connected to the output channel 1 of the dynamic signal analyzer and is used to drive the shaker. The amplifier settings were adjusted to supply a significant amount of power to the shaker without causing the wafer to be forced into its nonlinear region. The amplifier is set to constant voltage and the level control set to 475 (0-1000 range).

2.3 Test Procedure

Prior to any testing, the SigLab hardware must first be powered up. After powering up the SigLab hardware, the vss software of SigLab can be initiated. The SigLab vss setup files used in this thesis can be found in Appendix C. Then the amplifier can be powered up and the B-1 Blower set to low.

The mc-Si wafer is centered on the cylindrical test fixture, utilizing a centering fixture to ensure a consistent location +/-0.2cm from test to test. The solar cell is held in place with application of a weak vacuum at its center utilizing the SaveVac85 pump. No visible wafer bending was observed after application of this negative pressure.

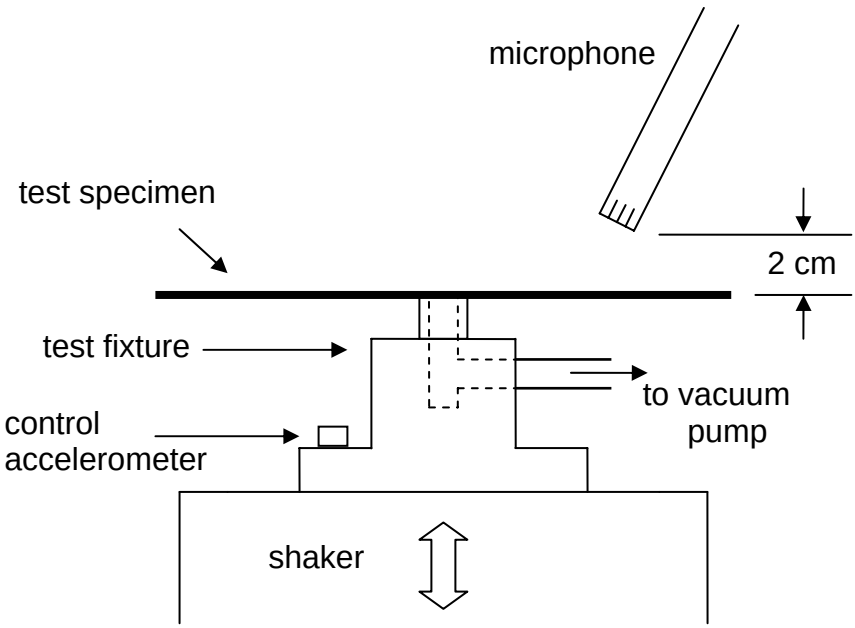

Figure 1. 2-Dimenional sketch of test fixture, test equipment, and test specimen.

2.4 Frequency Response and Coherence

The frequency response function, also known as the transfer function, is a complex function of frequency that contains both magnitude and phase information and is presented graphically using magnitude and phase versus frequency plots. Swept-sine is a method of measuring the frequency response function of a dynamic system. Swept-sine frequency response utilizes a sine wave as the system excitation and is stepped through the frequency range of interest. The reference channel (always channel 1 in vss) measures the excitation signal while the response channels measure the output of the system(s) under test. All input channels are measured using a narrow-band tracking filter whose pass-band is centered on the excitation frequency of each step. The tracking filter helps reduce the effects of system noise. The ratio of the sine wave amplitudes (Response Channel/ Reference Channel) is displayed as the transfer function magnitude. The computation is actually the ratio of the cross-spectrum and the reference auto-spectrum which is complex and contains both magnitude and phase information.

The coherence is a function of frequency. It provides a measurement of the power in the sound pressure that is caused by the power in the fixture acceleration. A coherence of 1 means that all of the measured sound pressure is caused by the acceleration input; whereas a coherence of 0 means that none of the sound pressure is caused by the input. The excellent (i.e., near unity) coherence shown in Figure 3 was found in all tests.

CHAPTER 3

EFG SOLAR CELL TEST RESULTS

3.1 Test Specimens

A set of 10cm x 10cm as-grown mc-Si wafers produced by the Edge-defined Film-fed Growth (EFG) method [8] with a nominal thickness of 340 micron was used in this study. All wafers were initially screened for defects such as microcracks at the wafer edge, which could affect the excited vibratory modes, using high resolution Scanning Acoustic Microscopy (SAM). A threshold crack length of 10 microns at the wafer periphery was used to exclude samples from this study [7]. The acoustic microscopy also was used to measure wafer thickness required for both the optical polariscopy and vibration measurements and analyses.

3.2 Residual Stress

Following SAM inspection, the wafers were measured with scanning infrared polariscopy to assess the level and distribution of in-plane stress using a method described elsewhere [4]. Stress maps of the twelve test wafers were obtained from this infrared polariscopy. They can be found in Appendix B. Representative stress maps are presented in Figure 2. Each of the stress maps in Figure 2 uses a grid of 100x100 data points to cover the 10 cm square wafer. Figure 2a shows an example of a wafer with a fairly uniform stress distribution over most of the wafer (sample 16). In contrast, significant non-uniform variation in the residual stress distribution is observed within wafer sample 22 as illustrated in Figure 2b.

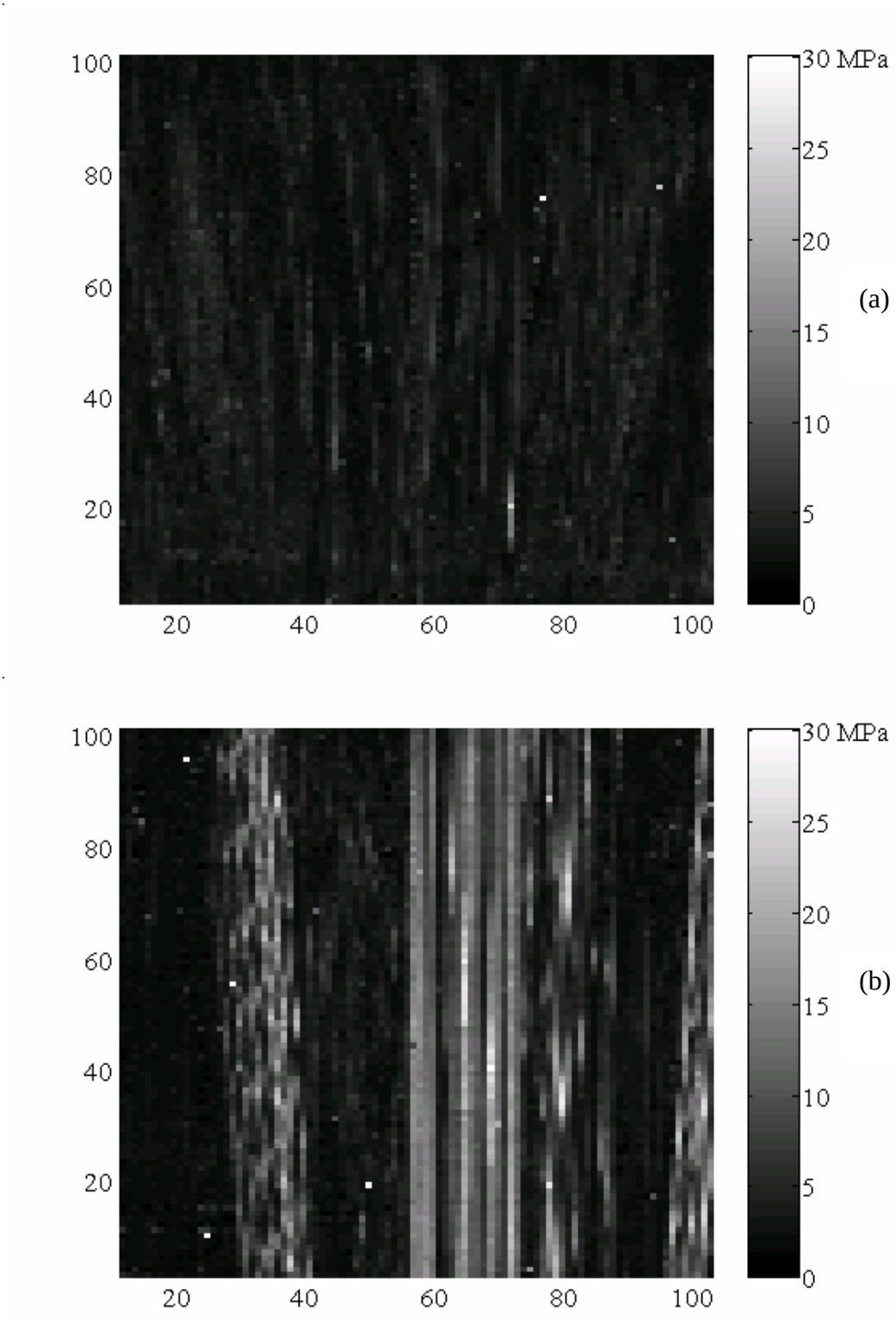

Figure 2. Representative residual stress maps for a 10cm x 10cm EFG wafer: a) with a relatively uniform distribution (sample 16), and b) with a non-uniform distribution (sample 22).

Potential single number descriptors have been identified to quantify the stress maps. These include average stress, peak stress, average of lowest ten percent stress, average of highest ten percent stress, average of highest five percent stress, and average of highest one percent stress. Table 1 summarizes the computed values of these descriptors for the twelve test wafers. The m-file, new_percent.m, used to extract these descriptors from the raw stress data can be found in Appendix A along with other m-files used for data analysis in this thesis.

Table 1. Potential descriptors for residual stress in wafers.

Sample Number	Thickness [microns]	Average Stress [MPa]	Peak Stress [MPa]	High Stress (1%) [MPa]	High Stress (5%) [MPa]	High Stress (10%) [MPa]	Low Stress (10%) [MPa]
13	348	5.06	28.58	21.47	17.20	15.17	1.39
14	341	4.37	31.37	19.47	15.43	13.38	1.45
15	340	4.10	29.46	20.29	14.03	11.32	1.27
16	366	2.81	25.01	8.46	6.03	5.28	1.48
17	369	3.33	30.57	16.83	11.27	8.87	1.41
18	356	4.58	37.78	18.54	14.66	12.64	1.28
19	343	4.11	29.56	20.85	16.42	13.62	1.19
20	349	4.93	28.66	20.72	17.11	15.00	1.55
21	344	5.38	44.77	25.58	18.61	15.46	1.60
22	346	5.65	29.17	23.45	18.82	16.60	1.35
23	347	4.36	29.84	21.55	17.08	14.44	1.32
24	344	4.10	29.54	22.37	17.56	13.93	1.28

3.3 Frequency Response Measurements

3.3.1 Overview

The shaker was used to excite the twelve solar cell wafers, numbered 13 thru 24, and the frequency response of each wafer was recorded. The wafers were tested over

three various ranges explained later in detail. The order in which they were tested was randomized to minimize any type of creep or bias measurements. The randomization tables and run order for the broadband range tested can be found in Appendix D.

3.3.2 Broadband Range 400-1800 Hz

Initially, the 12 specimens were swept-sine tested once each from 400 Hz to 1800 Hz with a tracking bandwidth of 10 Hz. The broadband range produced similar curves for all of the wafers, with the exception of specimens 15 and 22. The curves that are similar to the norm will be referred to as "normal" curves. The plots of these "normal" curves are similar in shape but vary in resonance frequency and peak amplitude. Figure 3 is the broadband frequency response of specimen 20 and is representative of a "normal" curve. The "normal" plot is well defined by two separated resonance frequencies, smooth lines, and a phase change of 180 degrees at resonance.

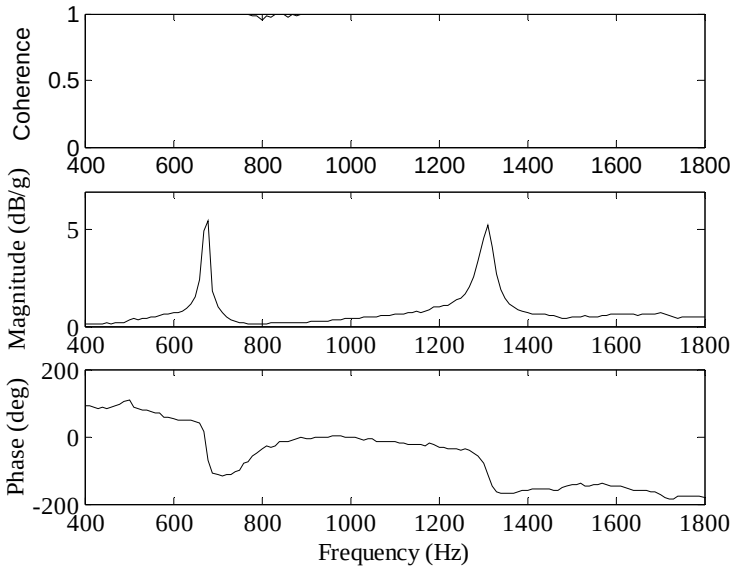

Figure 3. Frequency response of solar cell 20 symbolizing a "normal" curve over the broadband range.

Figure 4 is a plot of the frequency response of solar cell 15. At the lower resonance frequency, there appears to be two audible modes in the 650-750 Hz range. This split may be attributed to asymmetric distribution of residual stress within the wafer illustrated in figure 5.

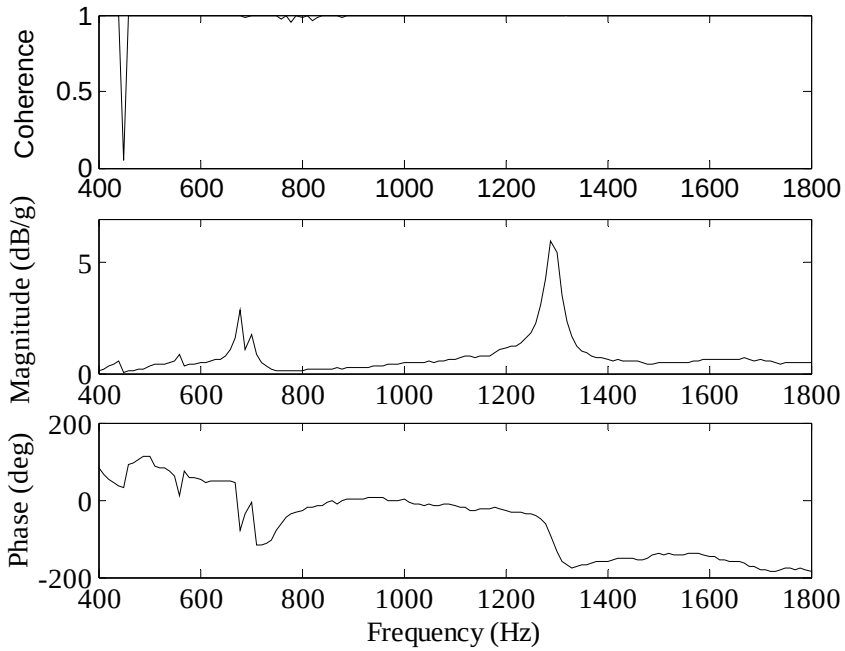

Figure 4. Plot of the frequency response of solar cell 15 with a split in the lower resonance frequency.

The frequency response plot and stress map of solar cell 22 have similar characteristics as that of solar cell 15 and therefore the same assumption of asymmetric distribution of residual stress also applies. Frequency response plots over the 400-1800 Hz broadband range of all the specimens used in this thesis can be found in Appendix E.

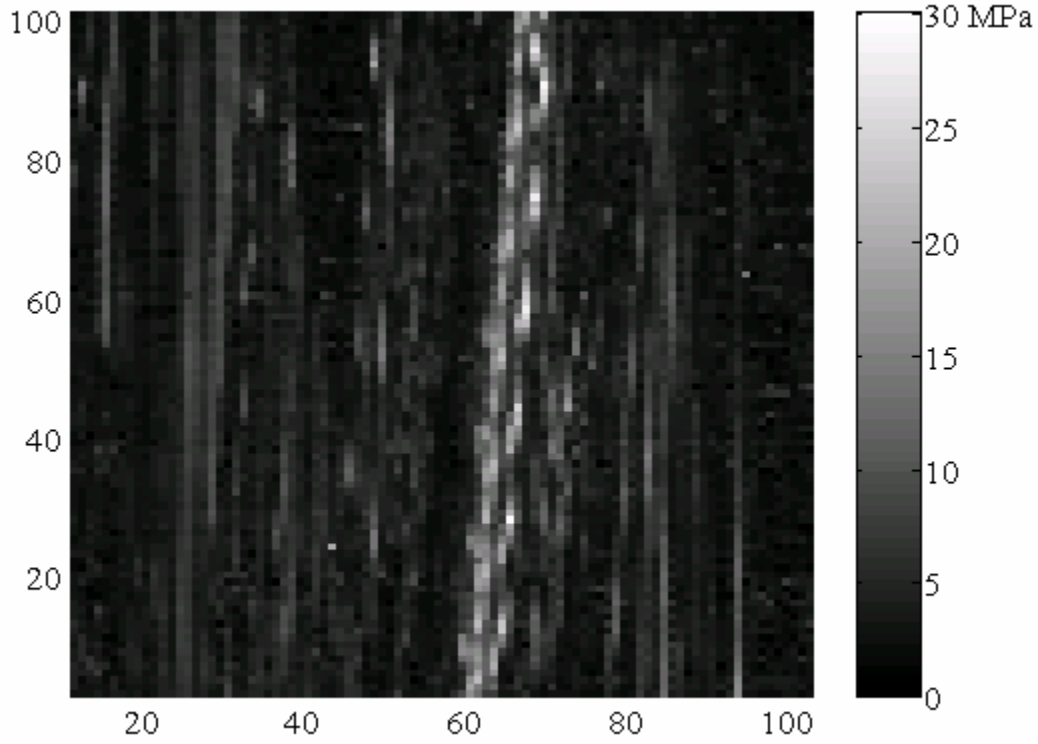

Figure 5. Stress map of specimen 15 illustrating asymmetric distribution of residual stress.

The main purpose of analyzing the frequency response of the wafers over the broadband range was to obtain a global view of the dynamics, and to identify narrowband ranges to zoom in on for better resolution. Table 2 summarizes the frequency response data obtained over the broadband range. It contains frequency response data for the twelve specimens and the range to zoom-in on for more precise data at resonance.

Table 2. Response data of solar cells over the broadband range including range to zoom-in for further investigation.

Specimen Number	Low Resonance Frequency	Peak Amplitude	High Resonance Frequency	Peak Amplitude	Low Frequency Range	High Frequency Range
13	700	4.84	1340	4.40	640-740	1230-1400
14	660	4.77	1290	4.90	600-720	1200-1350
15	680	2.86	1290	5.99	600-750	1200-1350
16	700	7.03	1380	4.52	650-750	1300-1450
17	700	5.32	1390	4.39	650-750	1260-1460
18	700	5.68	1360	4.45	640-740	1250-1450
19	670	5.38	1290	5.06	600-720	1200-1380
20	680	5.49	1310	5.23	600-750	1200-1400
21	670	6.29	1310	4.97	600-720	1200-1400
22	690	5.33	1320	4.75	650-750	1200-1400
23	680	7.27	1310	5.20	620-720	1200-1400
24	670	6.52	1340	4.35	600-720	1200-1400

3.3.3 Narrowband Ranges

As stated earlier, the narrowband ranges were established for the purpose of zooming-in on the resonance frequencies to better distinguish the differences between the solar cell wafers. The information obtained over the broadband range led to the determination of the narrow-band frequency ranges of 600-750 Hz for the first resonance frequencies and 1200-1450 Hz for the second resonance frequencies. These ranges were chosen because they capture all of the wafers first and second resonance frequencies, respectively. The capturing of all wafers in one range is beneficial to the experimenter in that it allows for no necessary changes in the parameters of the SigLab software from wafer to wafer during the experiment. The tracking bandwidth for both ranges was set at 2-Hertz so that better accuracy could be obtained. The wafers were randomly run three times over each narrowband range in order to account for the induced variability caused

by the experimenter when positioning the solar cell wafers on the fixture. The randomization tables and run order for each narrowband range can be found in Appendix F. The SigLab parameters for each range can be found in Appendix C of this thesis.

3.3.4 Narrowband Range 600-750 Hz

The 600-750 Hz narrowband range produced similar results to that of the broadband range in the sense that all solar cell specimens appear to be normal with the exception of solar cells 15 and 22. It should be noted that solar cell 14, although not as significant as 15 and 22, also displayed some "abnormal" attributes. Figure 6 shows a representative "normal" curve for the 600-750 Hz range. Again, it differs from other "normal" curves with respect to amplitude and frequency. Figure 7 and 8 are frequency response plots of solar cell wafers 15 and 22, respectively. It is noted that with the narrow-band, there are three peaks about the resonance frequency. Referring back to Figure 2, there are only two peaks at the lower resonance frequency. This alone justifies the use of narrowband ranges to produce more precise plots around the areas of interest.

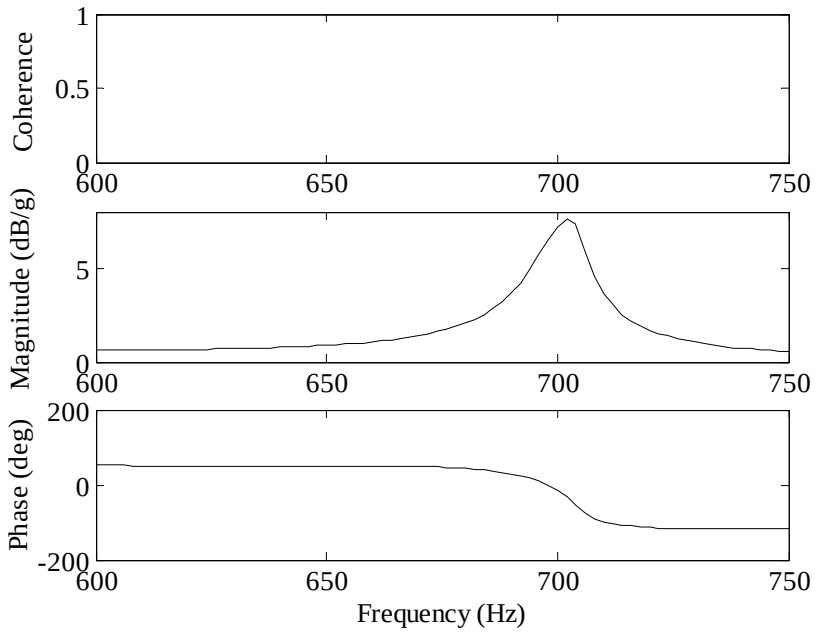

Figure 6. Plot of the frequency response of solar cell 16, symbolizing a "normal" plot over the narrowband range of 600 -750 Hz.

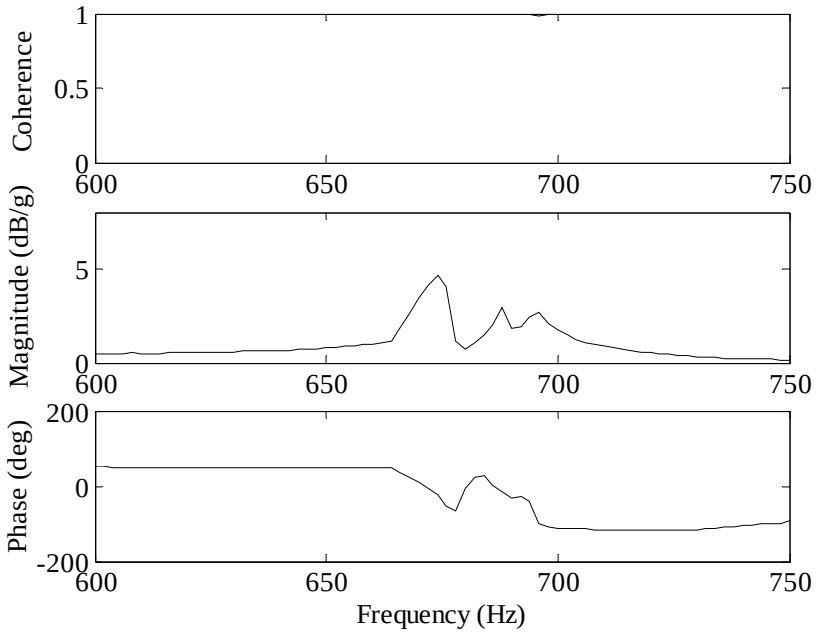

Figure 7. Plot of the frequency response of solar cell 15 over the narrowband range of 600-750 Hz with multiple splits in the resonance frequency.

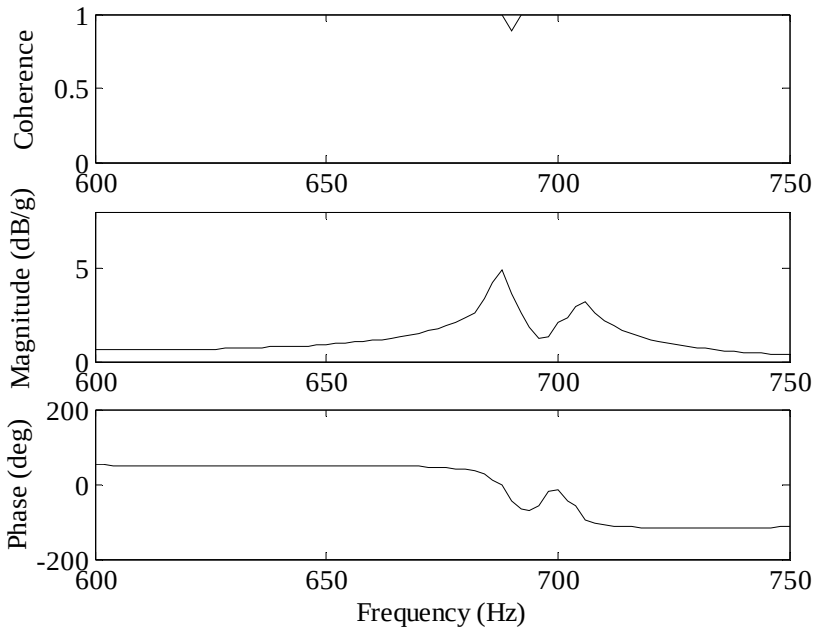

Figure 8. Plot of the frequency response of solar cell 22 over the narrowband range of 600-750 Hz with a split in the resonance frequency.

Figures 6 thru 8 can be found in Appendix G along with the other solar cells coherence and frequency response plots for the narrowband range of 600-750 Hz. The resonance frequencies and peak amplitudes were extracted from these graphs and are summarized in Table 3 and Table 4, respectively. In addition to Table 3 and Table 4, Figures 9 and 10 are graphical summaries of the mean, minimum, and maximum resonance frequencies and peak amplitudes for all 12 wafers in the specified range of 600-750 Hz. The mean value is used as a label for each wafer.

Table 3. Resonance frequency of solar cell specimens 13–24 over the narrowband range of 600-750 Hz.

Specimen Number	Resonance Frequency [Hz]			Mean [Hz]
	Test 1	Test 2	Test 3	
13	698	702	702	701
14	662	664	660	662
15	674	674	674	674
16	702	702	704	703
17	706	706	706	706
18	696	698	696	697
19	672	672	674	673
20	678	678	678	678
21	672	672	674	673
22	688	688	688	688
23	680	678	678	679
24	672	672	672	672

Table 4. Peak amplitude at resonance of solar cell specimens 13–24 over the narrowband range of 600-750 Hz.

Specimen Number	Peak Amplitude [dB/g]			Mean [dB/g]
	Test 1	Test 2	Test 3	
13	6.62	6.75	6.80	6.73
14	5.53	5.61	4.48	5.21
15	4.62	4.73	4.68	4.68
16	7.64	7.76	7.52	7.64
17	6.43	6.34	6.29	6.35
18	6.21	6.41	6.32	6.31
19	5.48	5.77	5.52	5.59
20	7.32	7.14	7.01	7.16
21	6.30	6.41	6.14	6.28
22	4.93	4.75	5.28	4.99
23	7.37	7.47	7.38	7.41
24	7.24	7.02	7.30	7.19

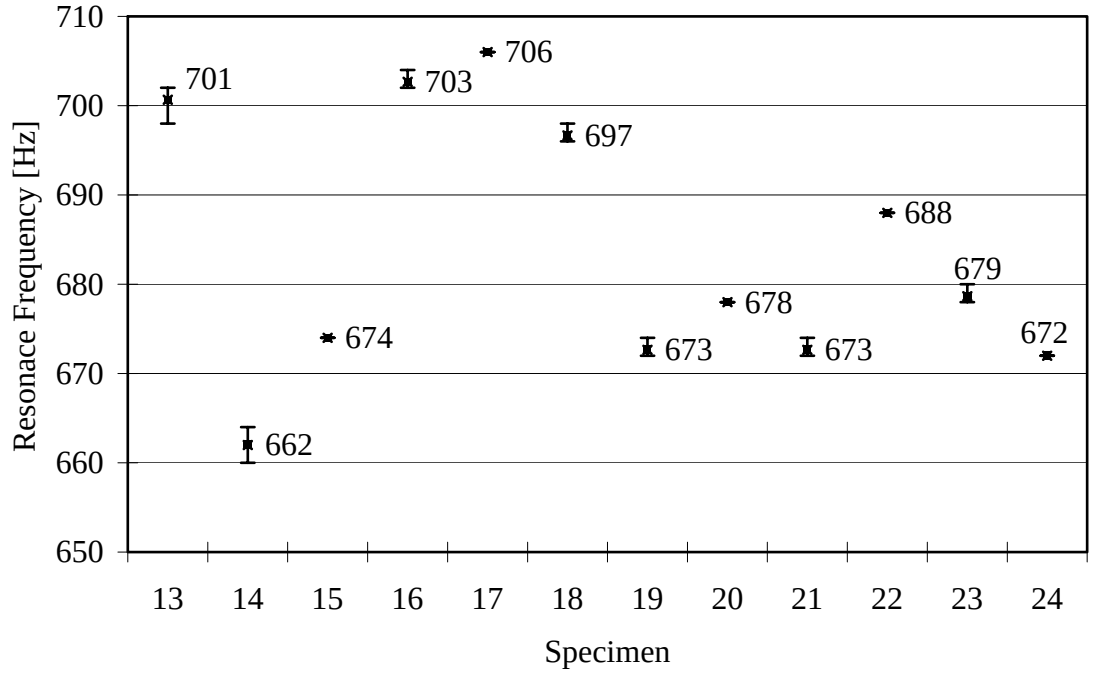

Figure 9. The mean, minimum and maximum resonance frequencies of solar cell wafers 13-24 over the narrowband range of 600-750 Hz.

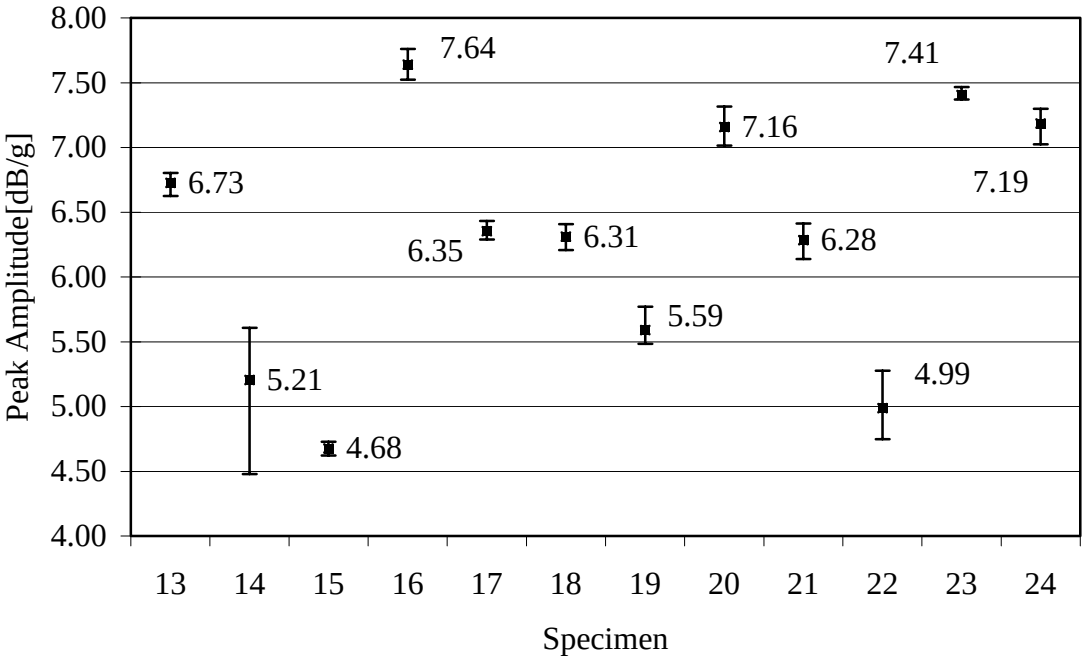

Figure 10. The mean, minimum and maximum peak amplitude of solar cell wafers 13-24 over the narrowband range of 600-750 Hz.

3.3.5 Narrowband Range 1200-1450 Hz

The narrowband range of 1200 to 1450 Hz produced "normal" graphs for all eleven of the twelve wafers. Figure 11 is a plot of solar cell 15 over the 1200-1450 Hz range. Remember that solar cell wafers 15 and 22 were considered to be abnormal in the 600-750 Hz range discussed earlier.

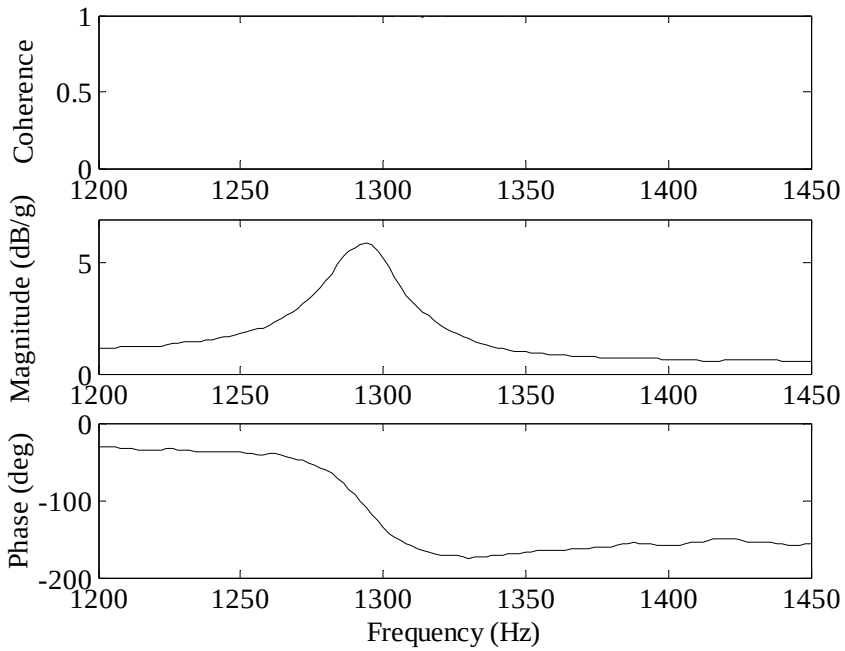

Figure 11. Plot of the frequency response of solar cell 15 over the narrowband range of 1200 to 1450 Hz representing a "normal" curve over the high frequency range.

Solar cell specimen 13 was the only wafer that graphically displayed a split about the resonance frequency over the narrowband range of 1200-1450 Hz. During testing, solar cell 13 made an "abnormal" whistle when resonating. Unlike the other specimens that gradually climbed a pitch scale while approaching resonance and then steadily declined, specimen thirteen displayed a fluctuating pitch about resonance. Figures 12 and

13 are the frequency response plot and stress map of solar cell 13, respectively. The stress map, Figure 13, displays a profound angular distribution of residual stress in addition to the vertical distribution existing in other specimens.

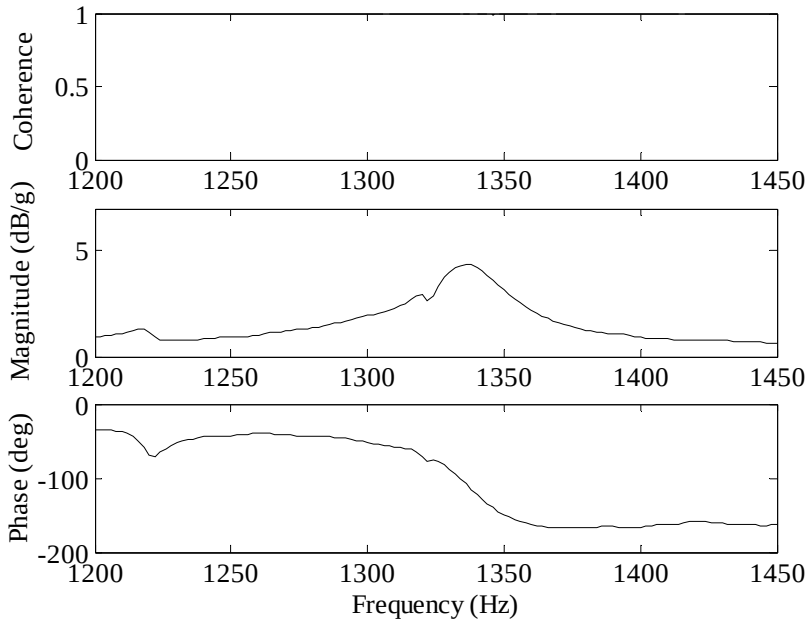

Figure 12. Plot of the frequency response of solar cell 13 over the narrowband range of 600-750 Hz with a minor split in the resonance frequency.

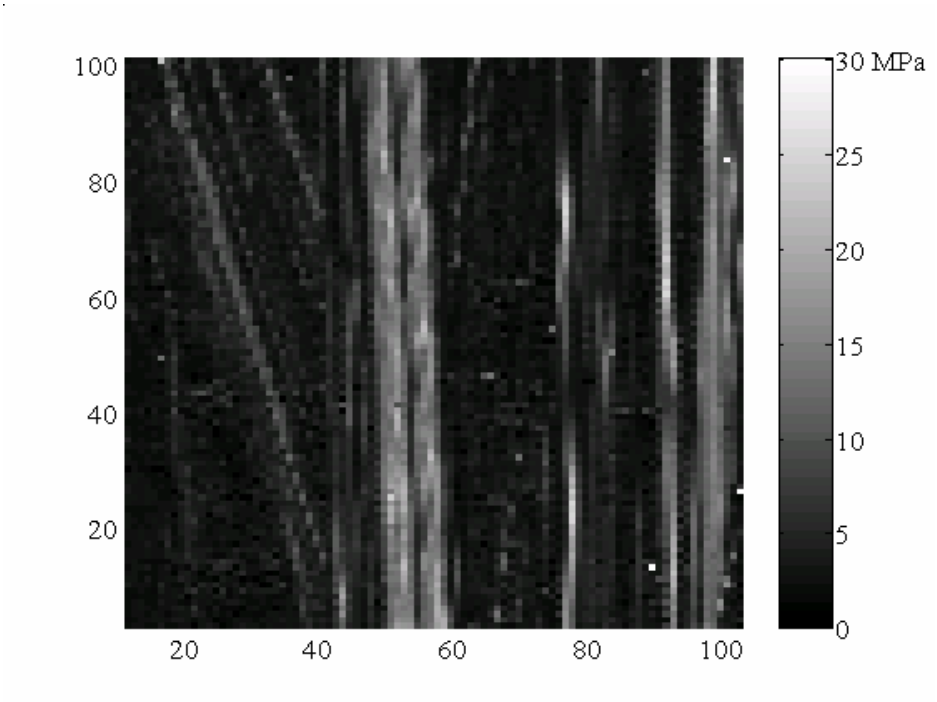

Figure 13. Stress map of solar cell 13 illustrating high levels of non-uniform distribution of residual stress with a profound angular distribution.

The frequency response plots over the narrowband range of 1200-1450 Hz for all solar cell specimens can be found in Appendix H. Table 5 and Table 6 summarize the data obtained from the frequency response plots found in Appendix H. In addition to Table 5 and Table 6, Figures 14 and 15 are graphical summaries of the mean, minimum, and maximum resonance frequencies and peak amplitudes for all 12 wafers in the specified range of 1200-1450 Hz.

Table 5. Resonance frequency of solar cell wafers 13–24 over the narrowband range of 1200-1450 Hz.

Specimen Number	Resonance Frequency [Hz]			Mean [Hz]
	Test 1	Test 2	Test 3	
13	1336	1340	1334	1337
14	1284	1290	1284	1286
15	1294	1294	1294	1294
16	1380	1380	1380	1380
17	1388	1388	1384	1387
18	1364	1364	1364	1364
19	1296	1298	1300	1298
20	1312	1312	1310	1311
21	1312	1314	1316	1314
22	1324	1316	1316	1319
23	1310	1310	1314	1311
24	1342	1346	1346	1345

Table 6. Peak amplitude at resonance of solar cell wafers 13–24 over the narrowband range of 1200-1450 Hz.

Specimen Number	Peak Amplitude [dB/g]			Mean [dB/g]
	Test 1	Test 2	Test 3	
13	4.34	4.64	4.46	4.48
14	5.38	5.50	5.16	5.35
15	6.59	5.91	5.90	6.13
16	4.48	5.19	5.01	4.89
17	4.89	4.78	4.66	4.78
18	4.62	4.92	4.92	4.82
19	5.72	5.88	5.87	5.83
20	5.43	5.38	5.58	5.46
21	5.22	5.23	5.28	5.25
22	5.03	5.20	5.19	5.14
23	5.53	5.21	5.41	5.38
24	4.66	4.89	4.55	4.70

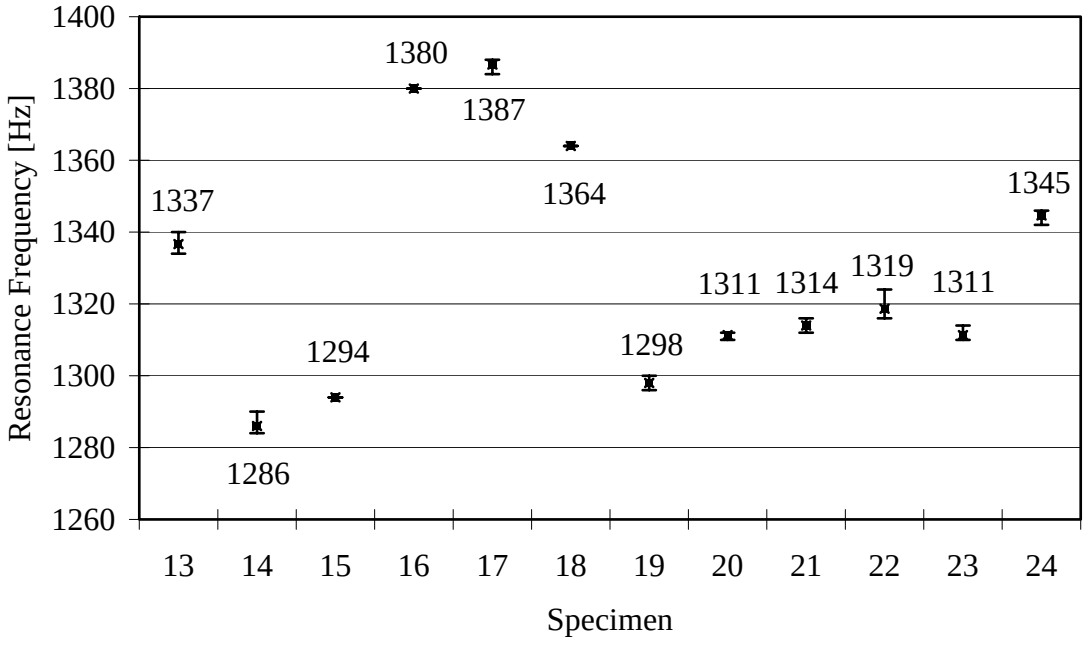

Figure 14. The mean, minimum and maximum resonance frequencies of solar cell wafers 13-24 over the narrowband range of 1200-1450 Hz.

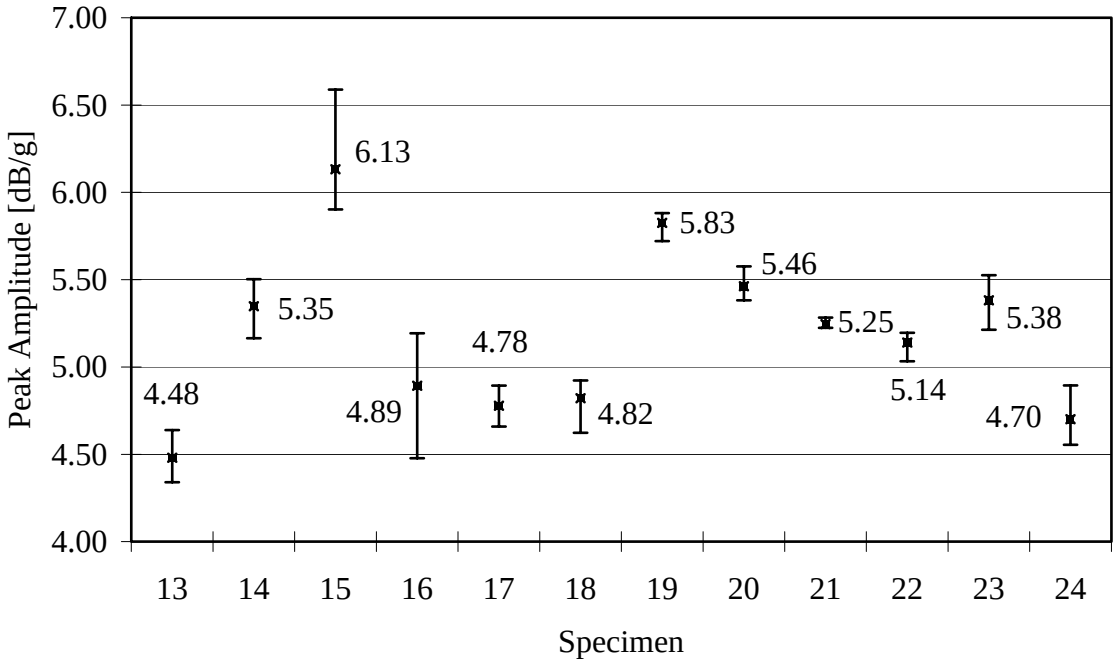

Figure 15. The mean, minimum and maximum peak amplitude of solar cell wafers 13-24 over the narrowband range of 1200-1450 Hz.

3.4 Analysis

Frequency response data were obtained for all of the twelve 10cm x 10cm wafers. Two dominant audible vibratory modes where found over the 400-1800 Hz range explored. A summary of the dominant audible natural frequencies and corresponding amplitudes for all twelve test samples is provided in Table 7. The low-frequency mode is in the 662 to 706 Hz range and the high-frequency mode is in the 1286 to 1387 Hz range. These frequencies and amplitudes are found to vary from wafer to wafer, but remain repeatable from test to test. In addition, mode splitting was observed for the low frequency mode in the frequency response data for wafers 15 and 22 as illustrated in Figure 7. This characteristic may be attributed to non-uniform residual stress or other defects in the wafer.

Table 7. Average dominant audible vibration mode test data.

	Low Mode		High Mode	
Specimen Number	Natural Frequency [Hz]	Peak Amplitude [dB/g]	Natural Frequency [Hz]	Peak Amplitude [dB/g]
13	701	6.73	1337	4.48
14	662	5.21	1286	5.35
15	674	4.68	1294	6.13
16	703	7.64	1380	4.89
17	706	6.35	1387	4.78
18	697	6.31	1364	4.82
19	673	5.59	1298	5.83
20	678	7.16	1311	5.46
21	673	6.28	1314	5.25
22	688	4.99	1319	5.14
23	679	7.41	1311	5.38
24	672	7.19	1345	4.70

Modal analyses of the wafers are performed using the finite element method. The wafer is modeled with shell elements with the center 12.7mm (0.5") diameter fixed. The material is modeled as isotropic with a modulus of 170 GPa, a Poisson's ratio of 0.27 and a density of 2.329 kg/m^3.

The analysis predicts nineteen vibratory modes over the 0 to 2,000 Hz range. However, most of these mode shapes exhibit asymmetry and are not efficient sound radiators. Two symmetric mode shapes are found at 668Hz and 1316Hz. These mode shapes are illustrated in Figures 16. The inherent symmetry in these two modes makes them the dominant audible modes in the frequency range considered.

The calculated modal frequencies of 668Hz and 1316Hz are in remarkably good agreement with the measured data summarized in Table 7, especially considering the simple isotropic material model assumed in the finite element analysis.

The calculated mode shapes were further validated through classic Chladni type patterns presented in Figure 17. These were obtained by sprinkling fine sand on the wafer while exciting the sample at each audible mode frequency. The sand collects at the nodal lines of the mode shapes. A comparison of the nodal lines from the calculated mode shapes in Figure 16 with the nodal sand lines in Figure 17 shows there is excellent agreement.

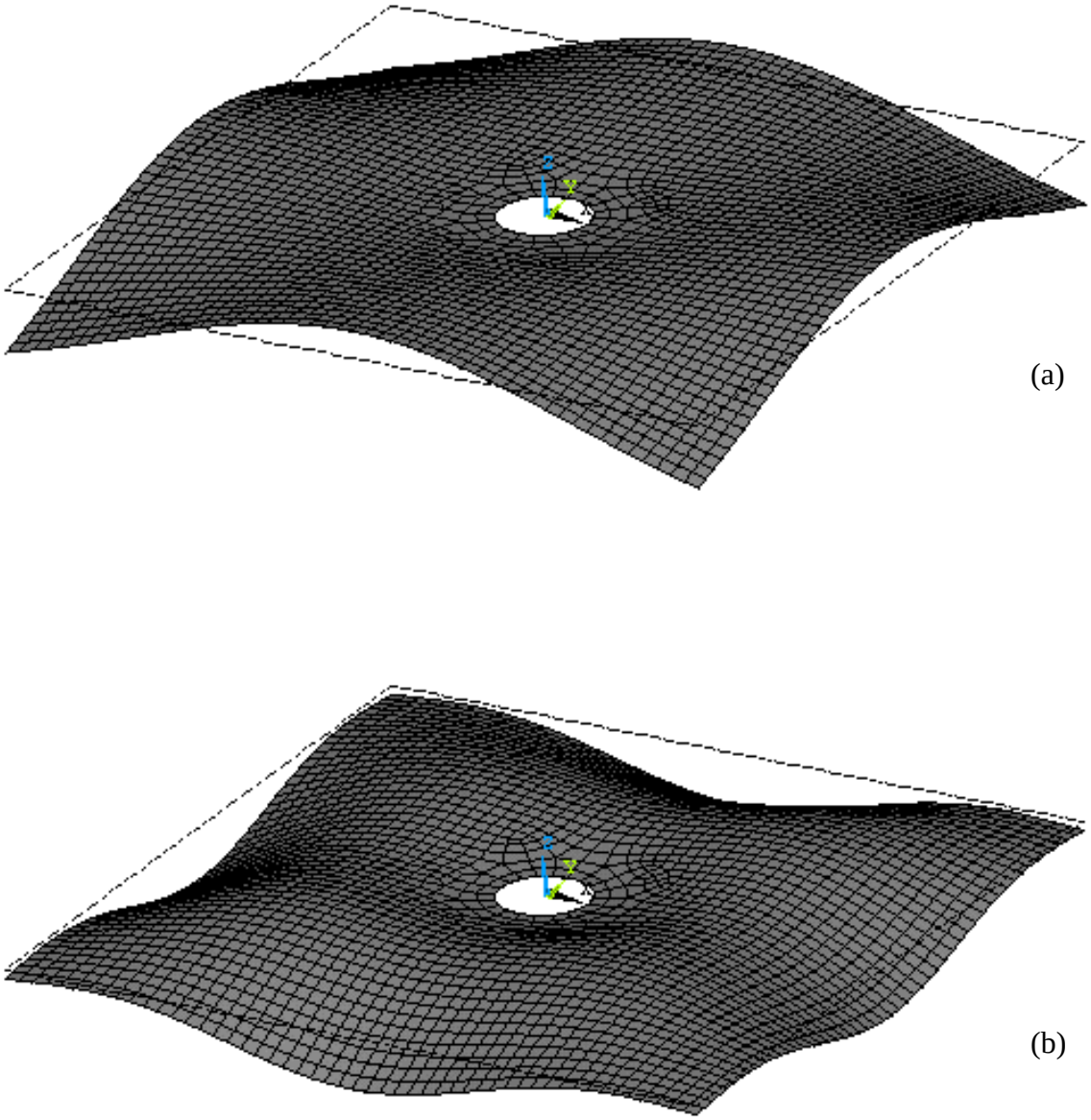

Figure 16. Computed audible mode shapes: a) low frequency, 668 Hz and b) high frequency, 1316 Hz.

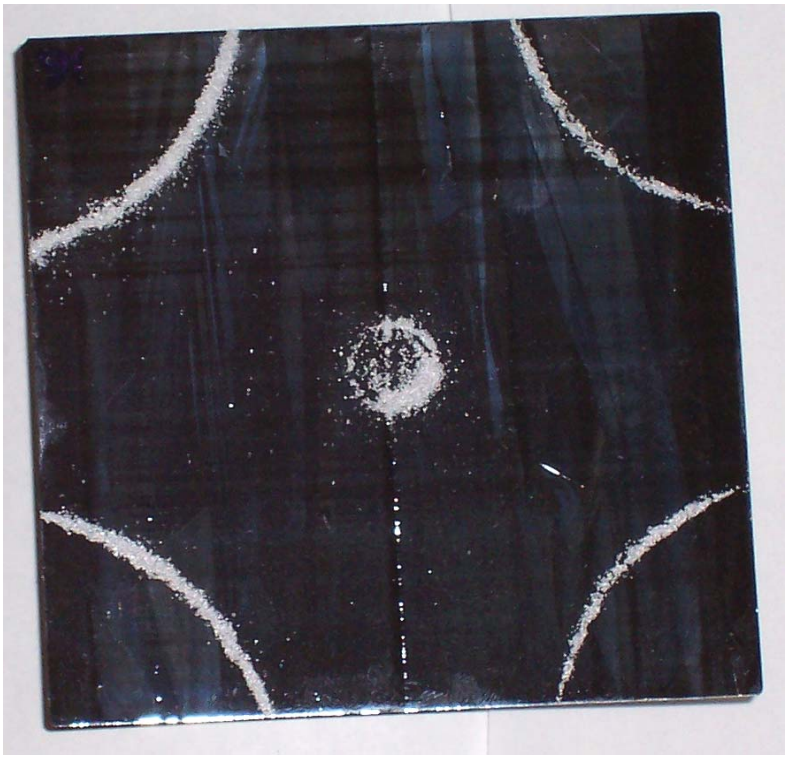

(a)

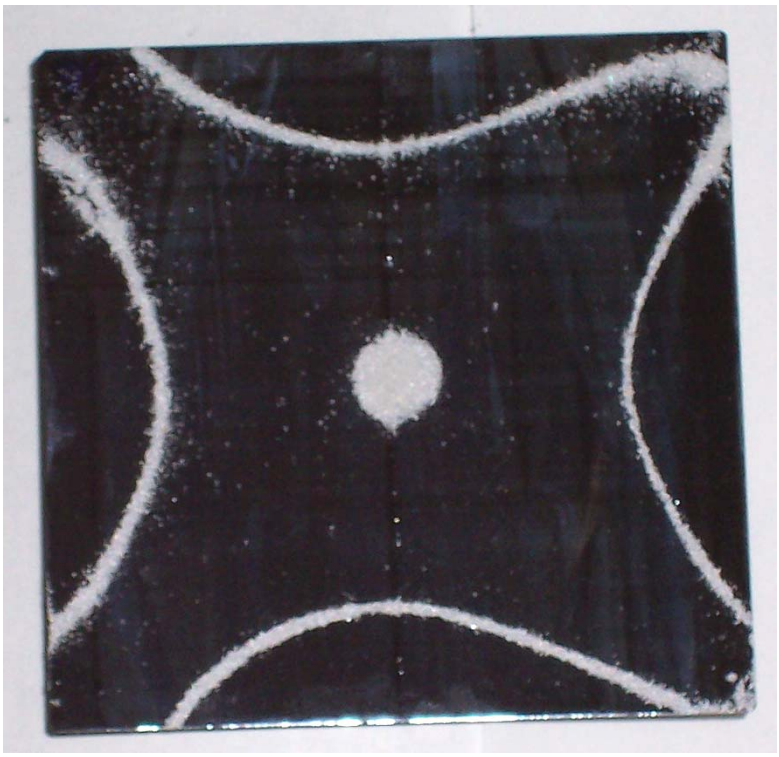

(b)

Figure 17. Chladni sand patterns for audible mode shapes: a) low frequency, 703 Hz and b) high frequency, 1380 Hz (sample 16).

3.5 Discussion

The measured low audible mode frequency data is plotted against the average of the highest ten percent residual stress descriptor in Figures 18 and 19. To factor out wafer thickness variation on natural frequency, the frequency data are normalized by thickness to the three-halves power [9] in the plots in Figures 18 and 19. Wafer thickness data for all specimens is included in Table 1. This normalized frequency and residual stress data is fitted to a linear model in Figure 18 and to a quadratic model in Figure 19. The plot shows that the vibration data correlates reasonably well with the stress data with correlation coefficients of 0.8. Note that data from sample 15 is not included in these fits because it appears as an outlier; with sample 15 data included the correlation coefficients drop to 0.6.

The data and models show a notable dependency of the audible mode frequencies on the residual stress. The audible frequencies increase with increasing stress suggesting that increasing residual stress increases wafer stiffness. Similar analyses with the high audible mode frequency data showed this trend but with lower correlation coefficients of 0.5.

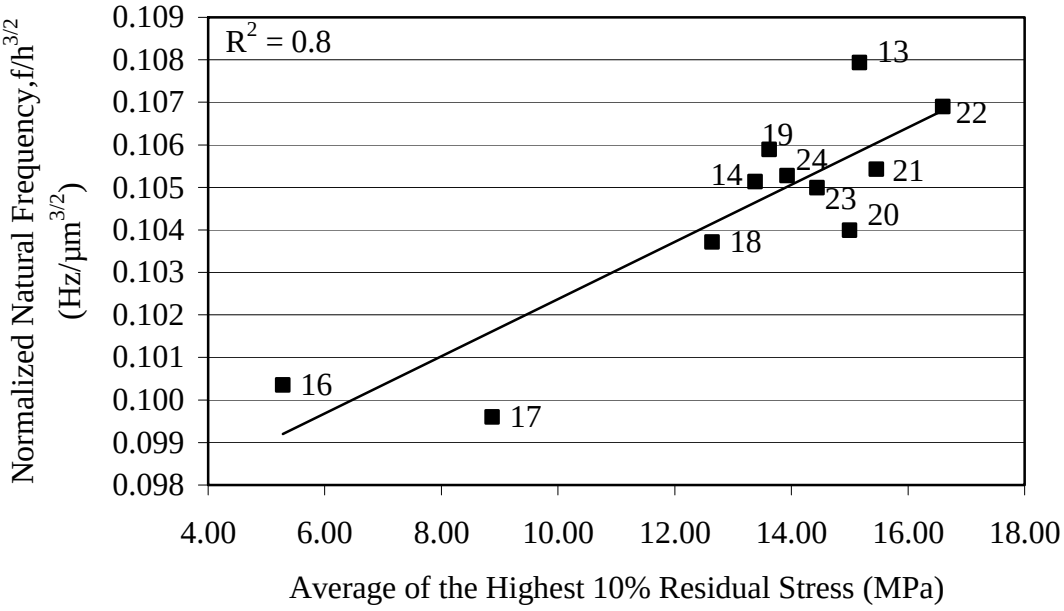

Figure 18. Linear correlation of normalized low audible mode frequency with residual stress.

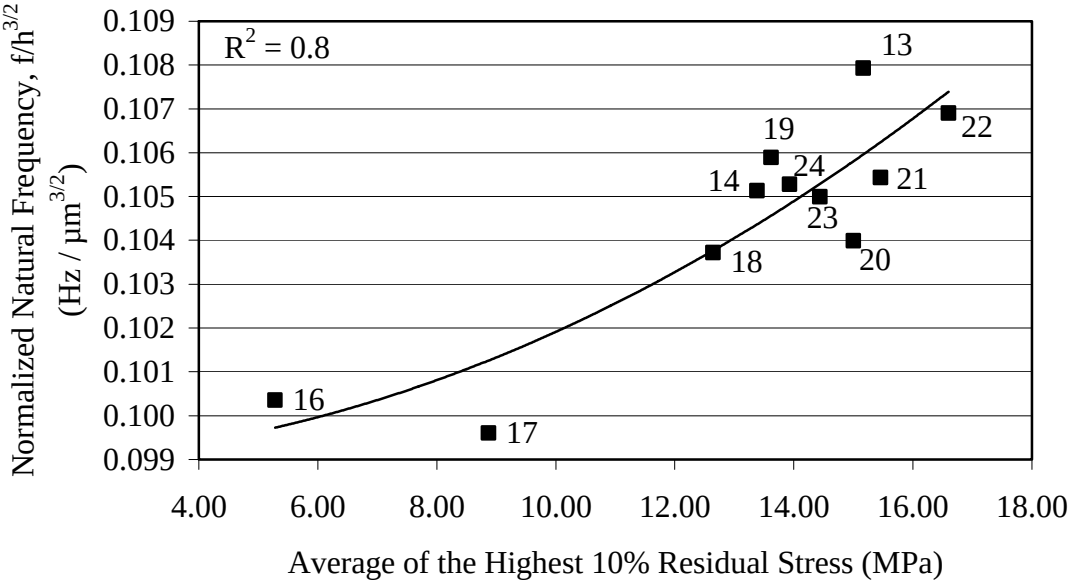

Figure 19. Quadratic correlation of normalized low audible mode frequency with residual stress.

CHAPTER 4

CONCLUSIONS

Audible vibratory mode data from a set of EFG mc-Si wafers with various levels and distributions of residual stress has been presented. The audible modes have been found to exhibit symmetry compared to non-audible vibratory modes. Mode splitting has been found in frequency response measurements of wafers with non-uniform residual stress distributions. Analysis of this vibratory data and the wafer residual stress measurements has shown reasonably good correlation for both linear and quadratic models. The audible natural frequencies of the wafers have been found to increase with increasing stress.

Currently, further research into the relationship between residual stress of silicon wafers and frequency response data is being conducted at the University of South Florida. The investigations include other types of silicon wafers ranging in thickness, shape, size, and growth technique. Impact testing is also being explored as a quicker alternative to swept-sine testing.

Stress diagnostics utilizing frequency response data has the ability of meeting both requirements of low-cost production and high efficiency in the manufacturing of silicon wafers. The results show promise for a fast and reliable metrological tool for in-line diagnostics of wafers with less than optimum properties due to as-grown and process-induced defects.

REFERENCES

1. Y. Kwon, S. Danyluk, L. Bucciarelli and J. P. Kalejs 1987 *J. Crystal Growth* 82, 221-227. Residual stress measurement in silicon sheet by Shadow Moire interferometry.

2. S. Ostapenko, I Tarasov, J. P. Kalejs, C. Haessler and E. U. Reisner 2000 *Semicond. Sci. Technol.* 15, 840-848. Defect monitoring using scanning photoluuminescence spectroscopy in mc-Si wafers.

3. Y. Gogotsi, C. Baek and F. Kirscht 1999 *Semiconductor Science and Technology* 14, 936. Raman micro-spectroscopy study of processing-induced phase transformations and residual stress in silicon.

4. M. Yamada 1985 *Appl. Phys. Lett.* 47, 365-367. Quantitative photoelastic measurement of residual strains in undoped semi-insulating GaAs.

5. R. W. Hoffman 1966 in *Physics of Thin Films* (G. Hass and T. E. Thun, editors) 211. New York: Academic Press.

6. S. Ostapenko and I. Tarasov 2000 *Appl.Phys.Lett*. 76, 2217. Non-linear resonance acoustic vibrations in Cz-Si wafers.

7. A. Belyaev, S. Lulu, I. Tarasov, S. Ostapenko and J. P. Kalejs 2002 *IEEE Proceedings* 332-335. Stress diagnostics in mc-Si wafers using an acoustic technique.

8. J. P. Kalejs 2004 *Diffusion and Defect Data Part B (Solid State Phenomena)* 95-96 159-174. Silicon ribbons for solar cells.

9. R. D. Blevins 2001 *Formulas for Natural Frequency and Mode Shape*. Florida: Krieger Publishing.

10. S. R. Best, D. P. Hess, A. Belyaev, S. Ostapenko and J. P. Kalejs et al. Submitted to *Applied Acoustics*. Audible Vibration Diagnostics of Thermo-Elastic Residual Stress in Multi-Crystalline Silicon Wafers.

APPENDICES

APPENDIX A: M-FILES

dataplot_bb.m

```
%  Dataplot_bb.m          Rev. 8/15/03
%  Retrieves and plots freq response data and coherence over broadband range 400-1800
       Hz from Siglab swept-sine test data files (.vss)
% Type “dataplot_bb”; press enter
% Type “load 13bb.vss –mat” (replace 13 with specimen number of interest) ; press enter
% Type “return” ; press enter

keyboard

%  Coherence vs Frequency Plot
subplot(311)
plot(Fvec,CohDat,'k')
set(gca,'fontname','Arial')
ylabel('Coherence')
axis([400 1800 0 1])
%   xlabel('Frequency [Hz]')

%  Magnitude vs Frequency Plot
subplot(312)
plot(Fvec,(24/10.582)*abs(XferDat),'k')
%set(gca,'fontname','Arial')
ylabel('Magnitude (dB/g)')

axis([400 1800 0 7])
%  xlabel('Frequency [Hz]')

%  Phase vs Frequency Plot
subplot(313)
plot(Fvec,(unwrap(angle(XferDat))).*(180/pi),'k')
%set(gca,'fontname','Arial','fontsize','12')
ylabel('Phase (deg)')
xlabel('Frequency (Hz)')


%  End
```

APPENDIX A (Continued)

dataplot_low.m

```
%  Dataplot_low.m          8/15/03
%  Retrieves and plots freq response data and coherence over narrowband range 600-750
       Hz from Siglab swept-sine test data files (.vss)
% Type “dataplot_low”; press enter
% Type “load 13low_1.vss –mat” (replace 13 with specimen number of interest and 1
       with experimental run number) ; press enter
% Type “return” ; press enter

keyboard

%  Coh vs plot
subplot(311)
plot(Fvec,CohDat,'k')
ylabel('Coherence')
axis([600 750 0 1])
% xlabel('Frequency [Hz]')

%  Mag vs freq plot
subplot(312)
plot(Fvec,(24/10.582)*abs(XferDat),'k')
ylabel('Magnitude (dB/g)')
axis([600 750 0 8])
%  xlabel('Frequency [Hz]')

%  Phase vs freq plot
subplot(313)
plot(Fvec,(unwrap(angle(XferDat))).*(180/pi),'k')
ylabel('Phase (deg)')
xlabel('Frequency (Hz)')

%  End
```

APPENDIX A (Continued)

dataplot_high.m

```
%  Dataplot_high.m          8/15/03
%  Retrieves and plots freq response data and coherence over narrowband range 1200-
       1450 Hz from Siglab swept-sine test data files (.vss)
% Type “dataplot_high”; press enter
% Type “load 13high_1.vss –mat” (replace 13 with specimen number of interest and 1
       with experimental run number) ; press enter
% Type “return” ; press enter

keyboard

%  Coh vs plot
subplot(311)
plot(Fvec,CohDat,'k')
ylabel('Coherence')
axis([1200 1450 0 1])
%   xlabel('Frequency [Hz]')

%  Mag vs freq plot
subplot(312)
plot(Fvec,(24/10.582)*abs(XferDat),'k')
ylabel('Magnitude (dB/g)')
axis([1200 1450 0 7])
%  xlabel('Frequency [Hz]')

%  Phase vs freq plot
subplot(313)
plot(Fvec,(unwrap(angle(XferDat))).*(180/pi),'k')
ylabel('Phase (deg)')
xlabel('Frequency (Hz)')

%  End
```

APPENDIX A (Continued)

new_percent.m

```
%name of file: new_percent
%retrieves desired percent of stress

%Procedure
%Type “new_percent13” (change 13 to desired specimen number) ; press enter
%Type “load stress13” (change 13 to desired specimen number) ; press enter
%Type “return” ; press enter

keyboard

xmin = 11;
xmax = 103;
ymin = 3;
ymax = 101;

%must change stress13 to desired wafer prior to running program
x=stress13(ymin:ymax, xmin:xmax);

%The size of x is an A by B matrix
[a b]=size (x);

c=a*b;

d=9206;

%Now we reshape the original matrix to a matrix with only one row and 'c' columns
r=reshape(x,1,c);

%Sort the matrix in ascending order
s=sort (r);

y=s(1:d);

%This value can be checked with given values to check validity of program
peak_stress=(max (y))/2

% Average of largest (numeric) percent of x

%p is defined as the amount of data points to be taken into account based on a percentage
```

APPENDIX A (Continued)

new_percent.m (Continued)

```
%1 percent
p=round(0.01*d);

high1=0;

for i=1:p
   high1=y(d-i+1)+high1;
end

high1=high1/(2*p)


%5 percent
p=round(0.05*d);

high5=0;

for i=1:p
   high5=y(d-i+1)+high5;
end

high5=high5/(2*p)


%10 percent
p=round(0.10*d);

high10=0;

for i=1:p
   high10=y(d-i+1)+high10;
end

high10=high10/(2*p)


%Average of smallest 10 percent of x

p=round(0.10*d);
```

new_percent.m (Continued)

```
low = 0;

for i = 1:p
   low=y(i)+low;
end

low = low/(2*p)

% Average of stresses

avg = 0;

for i = 1:d
   avg = y(i) + avg;
end

avg = avg/(2*d)

%end
```

APPENDIX A (Continued)

efg_usf.m

```
%name of file: efg_usf.m
%plots stress map of specimens

%Procedure
%Type “efg_usf” ; press enter
%Type “load stress13” (change 13 to desired specimen number) ; press enter
%Type “return” ; press enter

keyboard

xmin = 11;
xmax = 103;
ymin = 3;
ymax = 101;

%change stress13 to wafer of interest
set(surface(stress13/2), 'edgecolor', 'none');
caxis([0 30]);colorbar;

axis([xmin xmax ymin ymax]);
```

APPENDIX B: STRESS MAPS

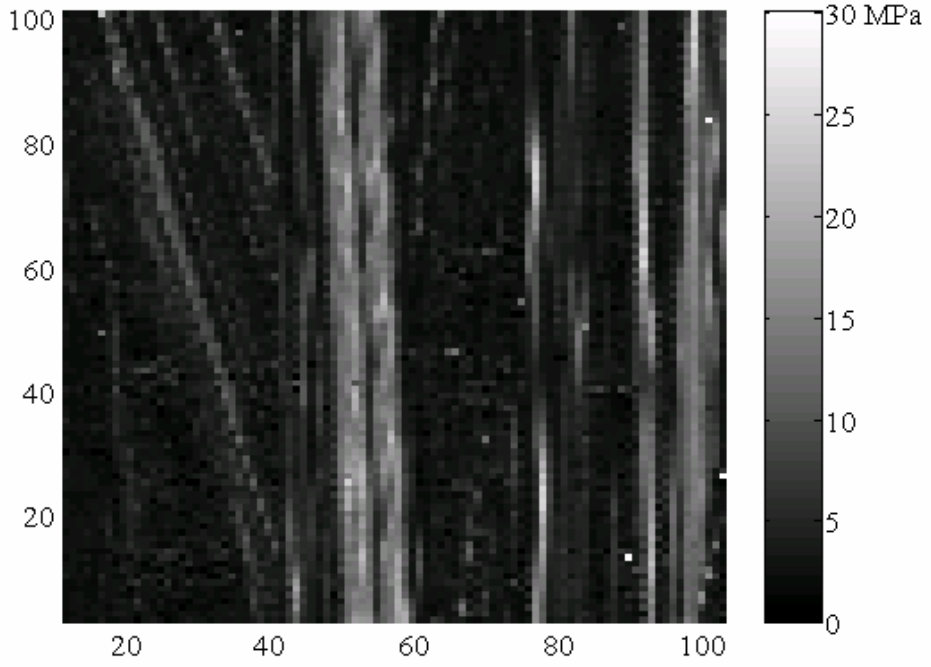

Figure 20. Stress map of solar cell specimen 13 using scanning infrared polariscopy.

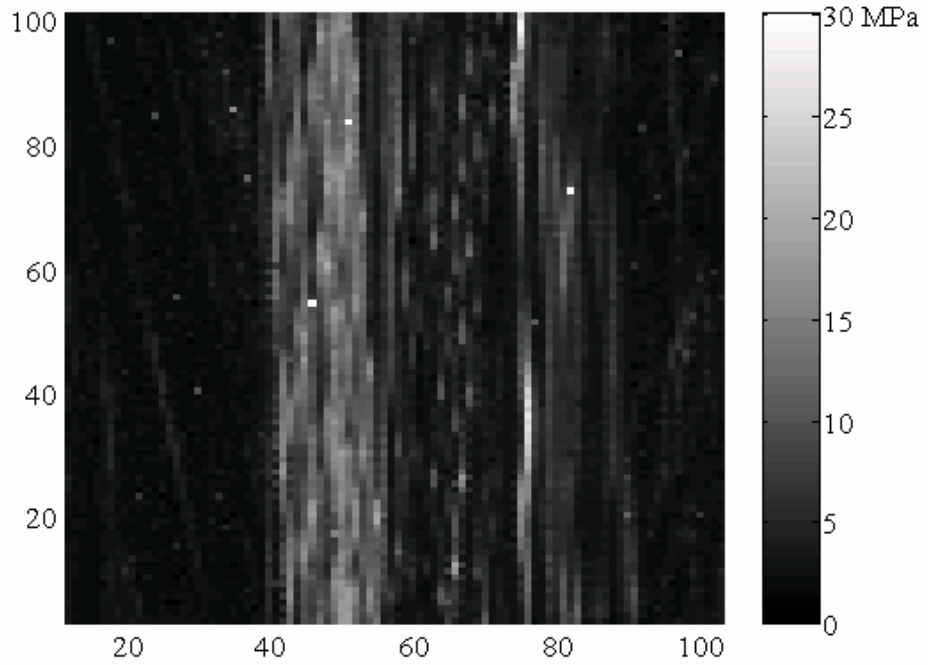

Figure 21. Stress map of solar cell specimen 14 using scanning infrared polariscopy.

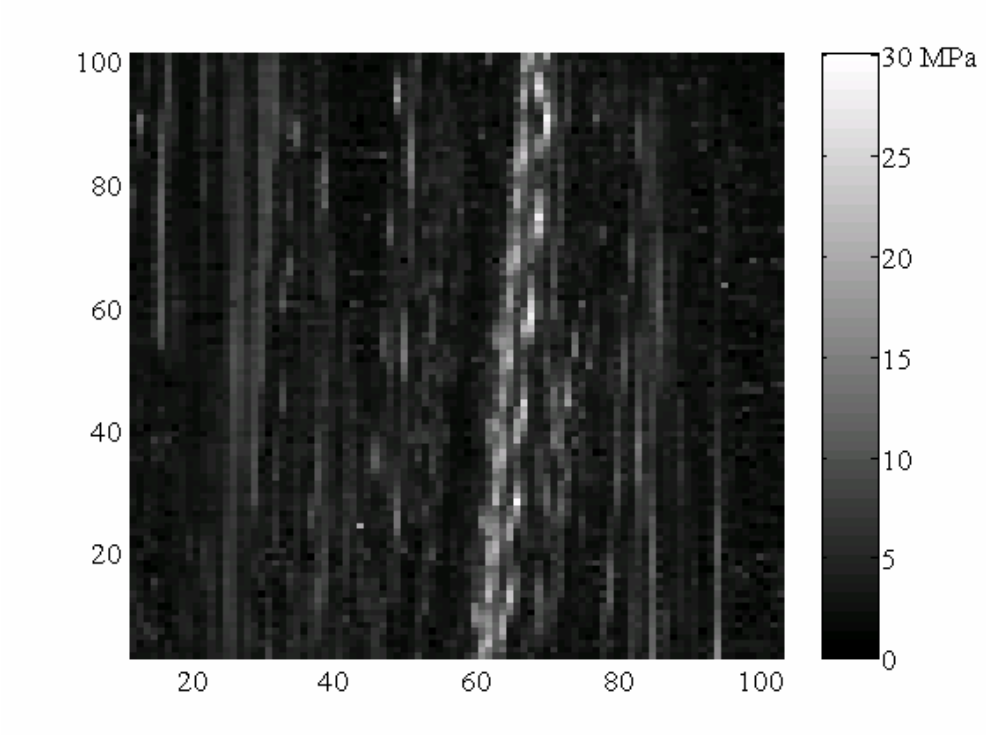

Figure 22. Stress map of solar cell specimen 15 using scanning infrared polariscopy.

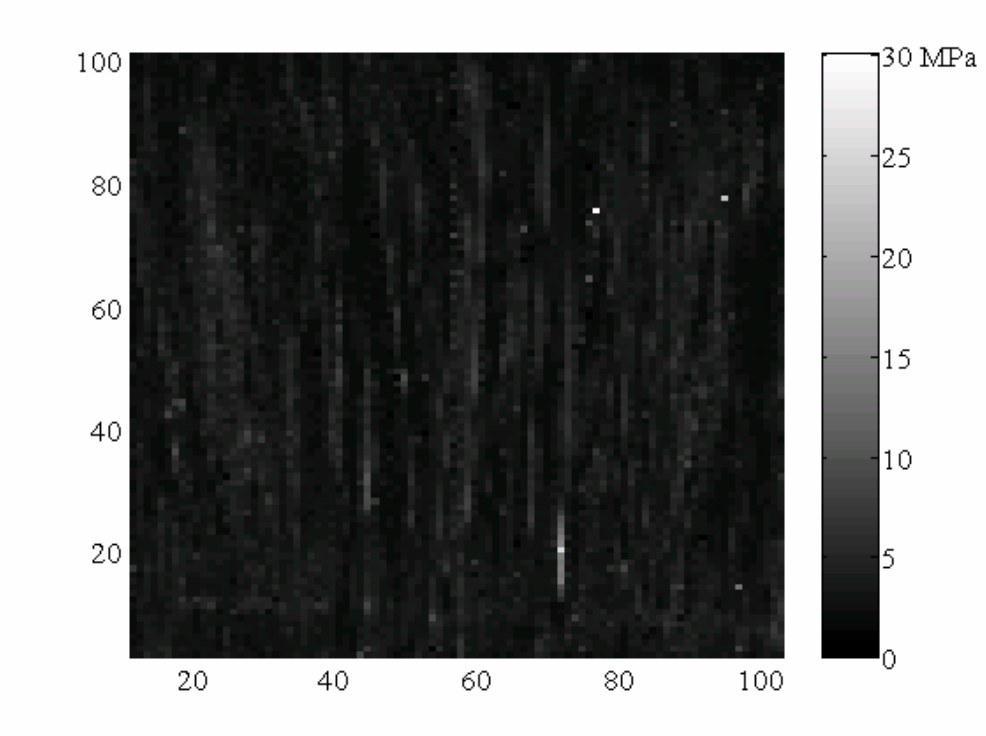

Figure 23. Stress map of solar cell specimen 16 using scanning infrared polariscopy.

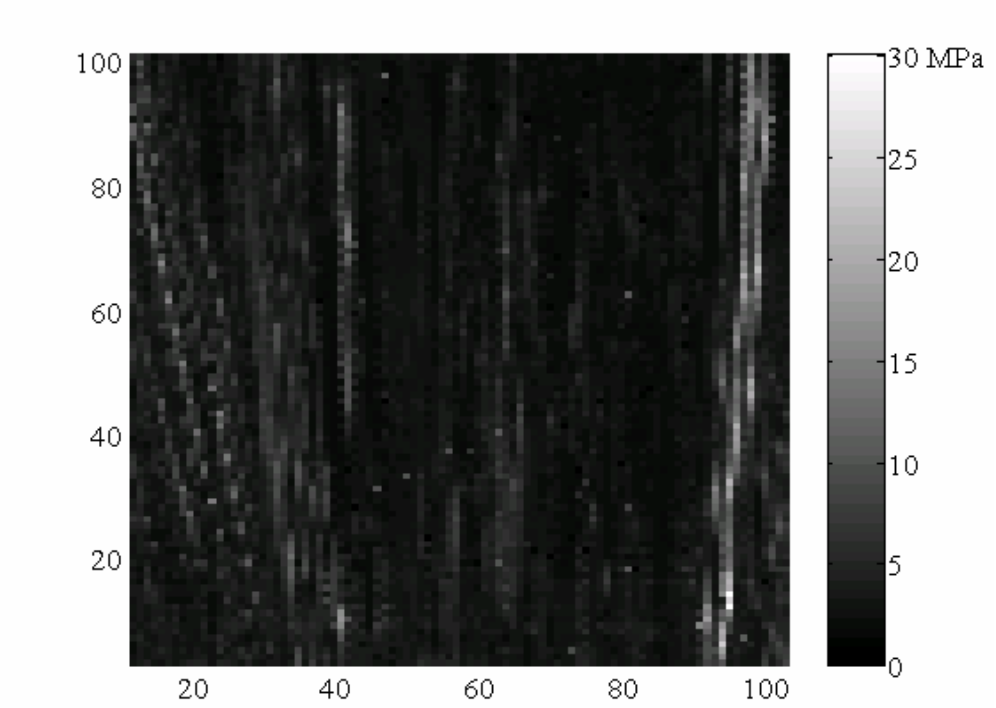

Figure 24. Stress map of solar cell specimen 17 using scanning infrared polariscopy.

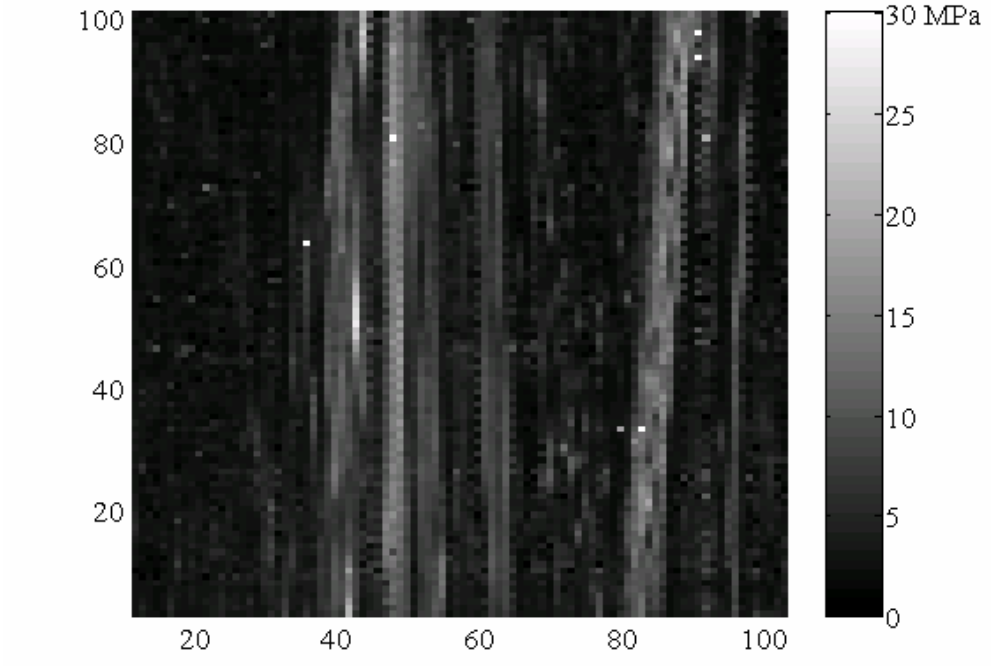

Figure 25. Stress map of solar cell specimen 18 using scanning infrared polariscopy.

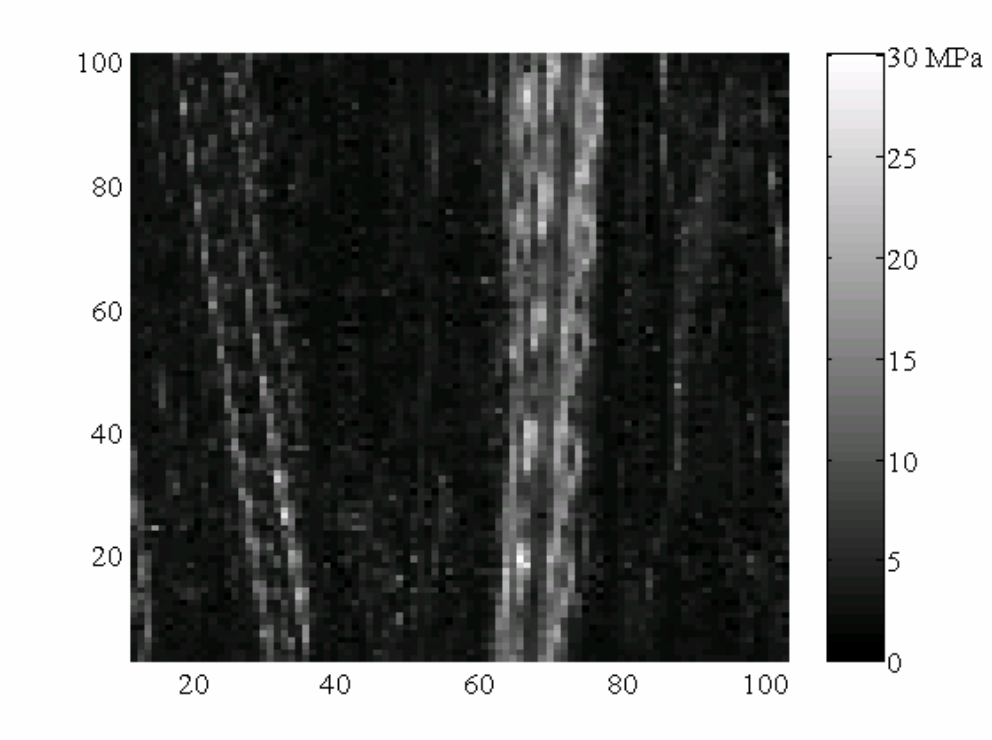

Figure 26. Stress map of solar cell specimen 19 using scanning infrared polariscopy.

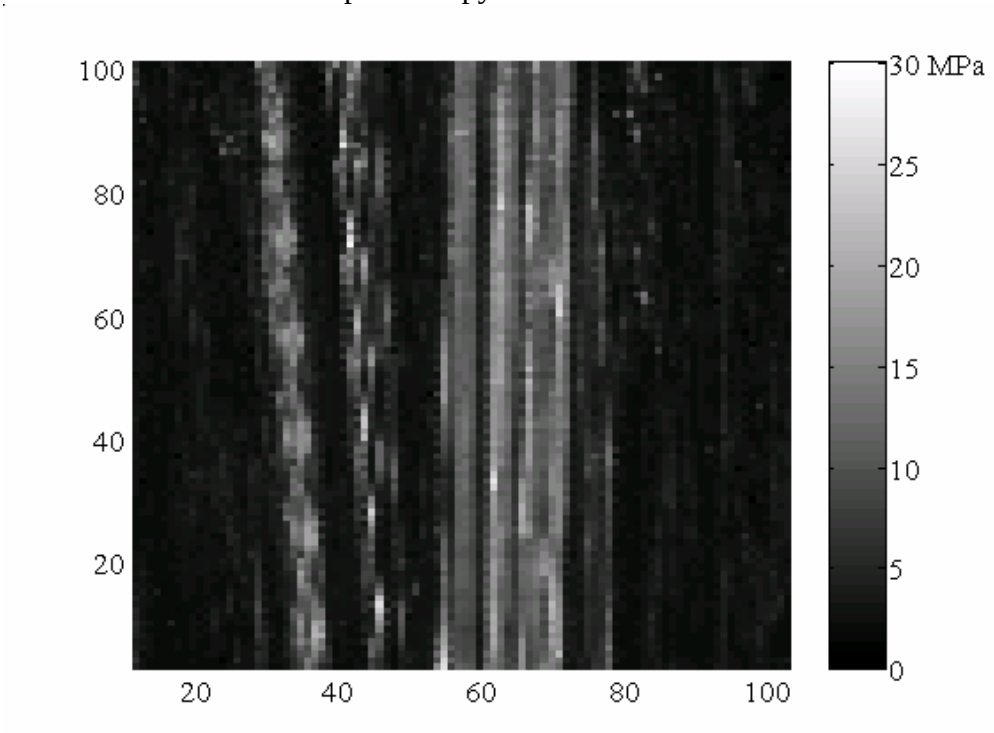

Figure 27. Stress map of solar cell specimen 20 using scanning infrared polariscopy.

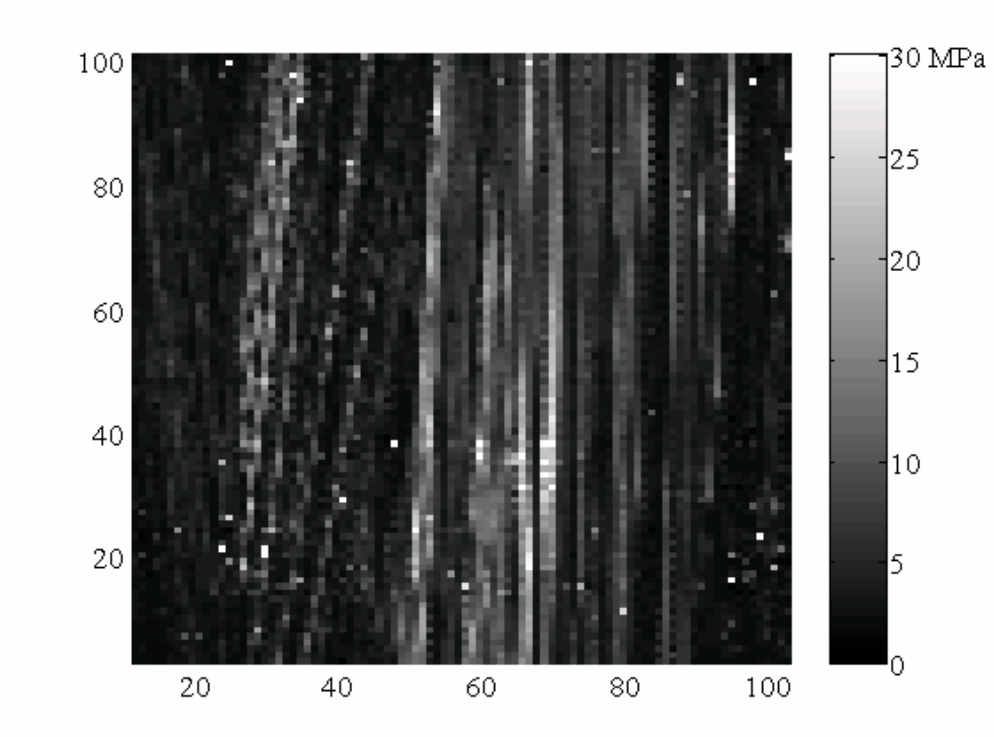

Figure 28. Stress map of solar cell specimen 21 using scanning infrared polariscopy.

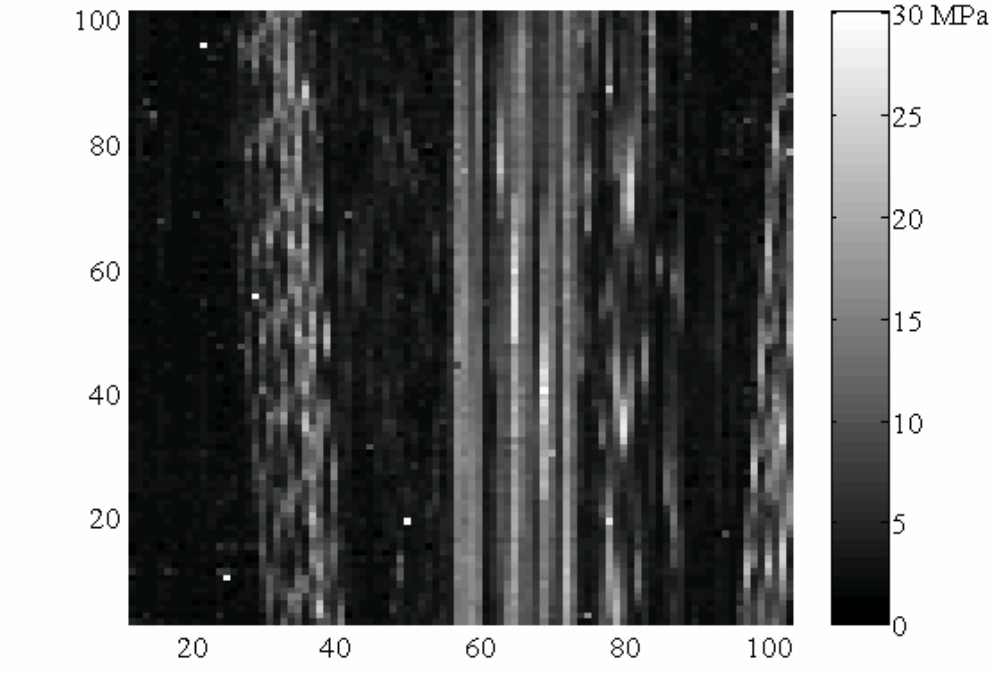

Figure 29. Stress map of solar cell specimen 22 using scanning infrared polariscopy.

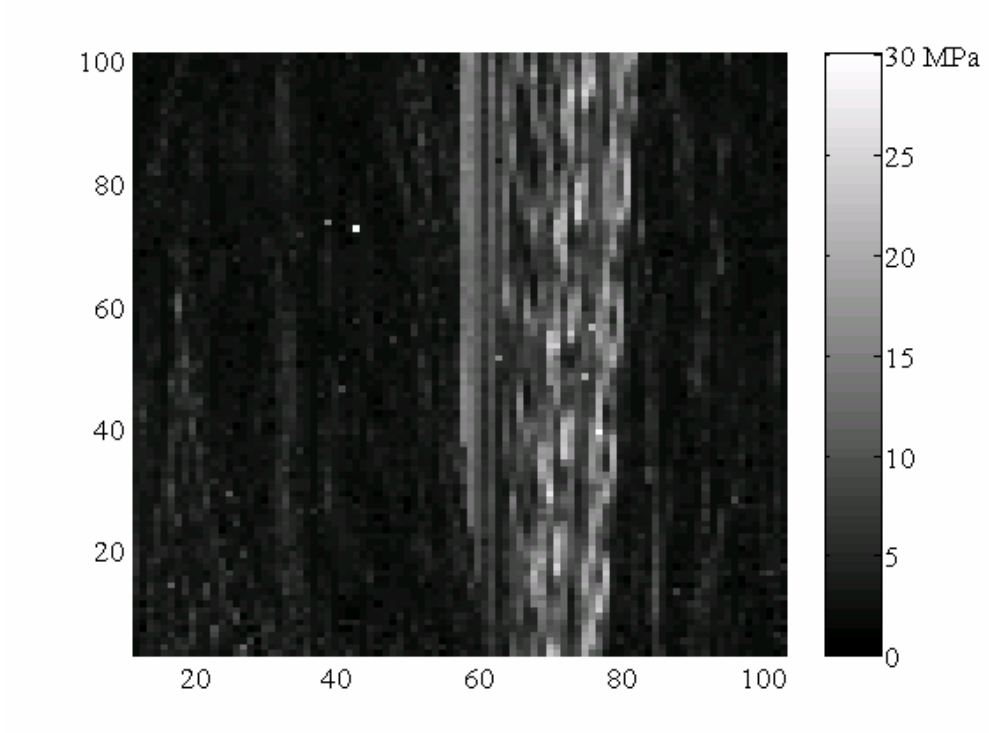

Figure 30. Stress map of solar cell specimen 23 using scanning infrared polariscopy.

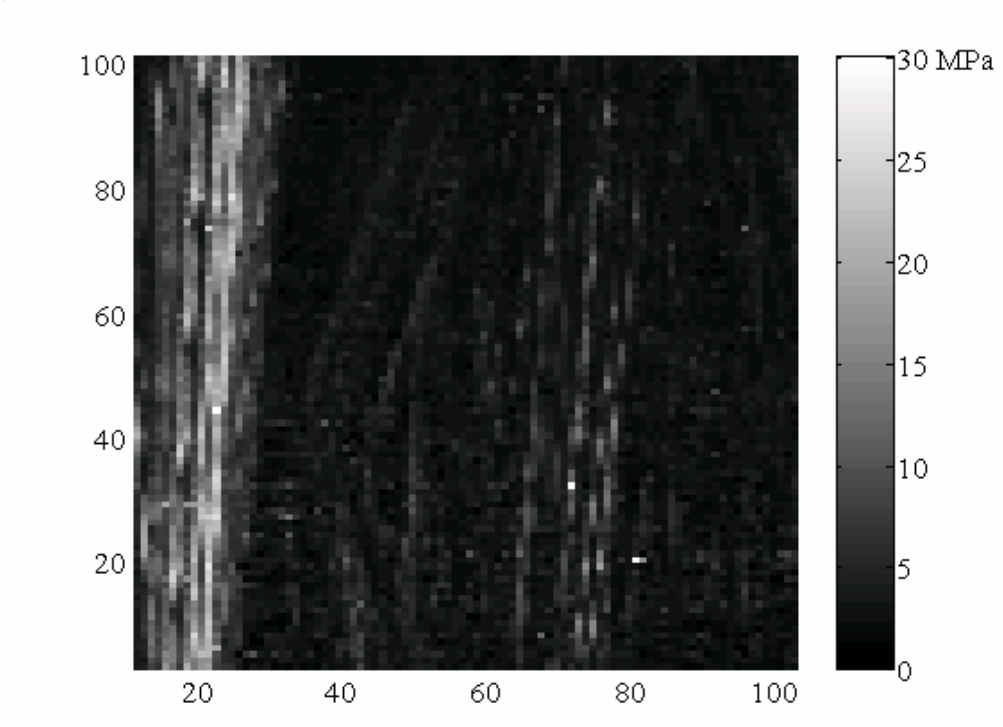

Figure 31. Stress map of solar cell specimen 24 using scanning infrared polariscopy.

APPENDIX C: SIGLAB VSS SETUP FILES

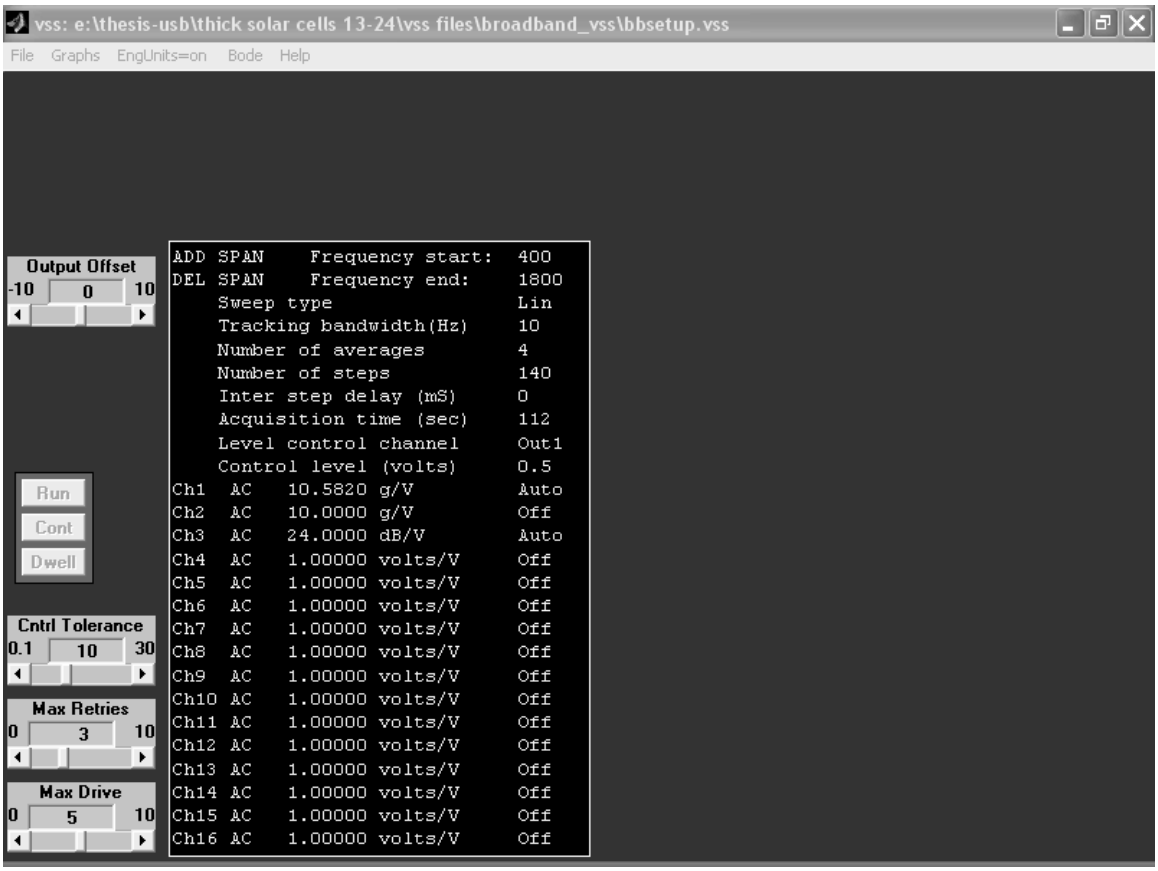

Figure 32. SigLab vss setup file for broadband range 400-1800 Hz.

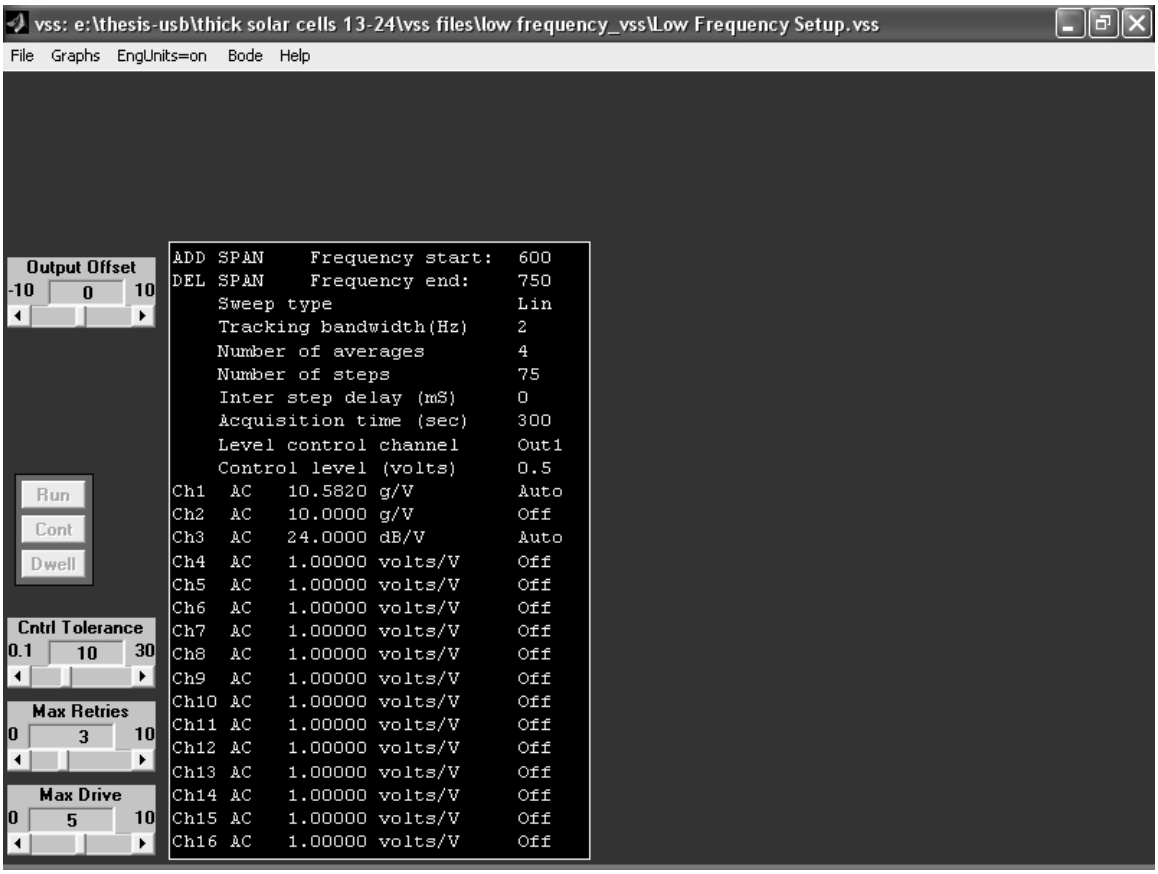

Figure 33. SigLab vss setup file for narrowband range 600-750 Hz.

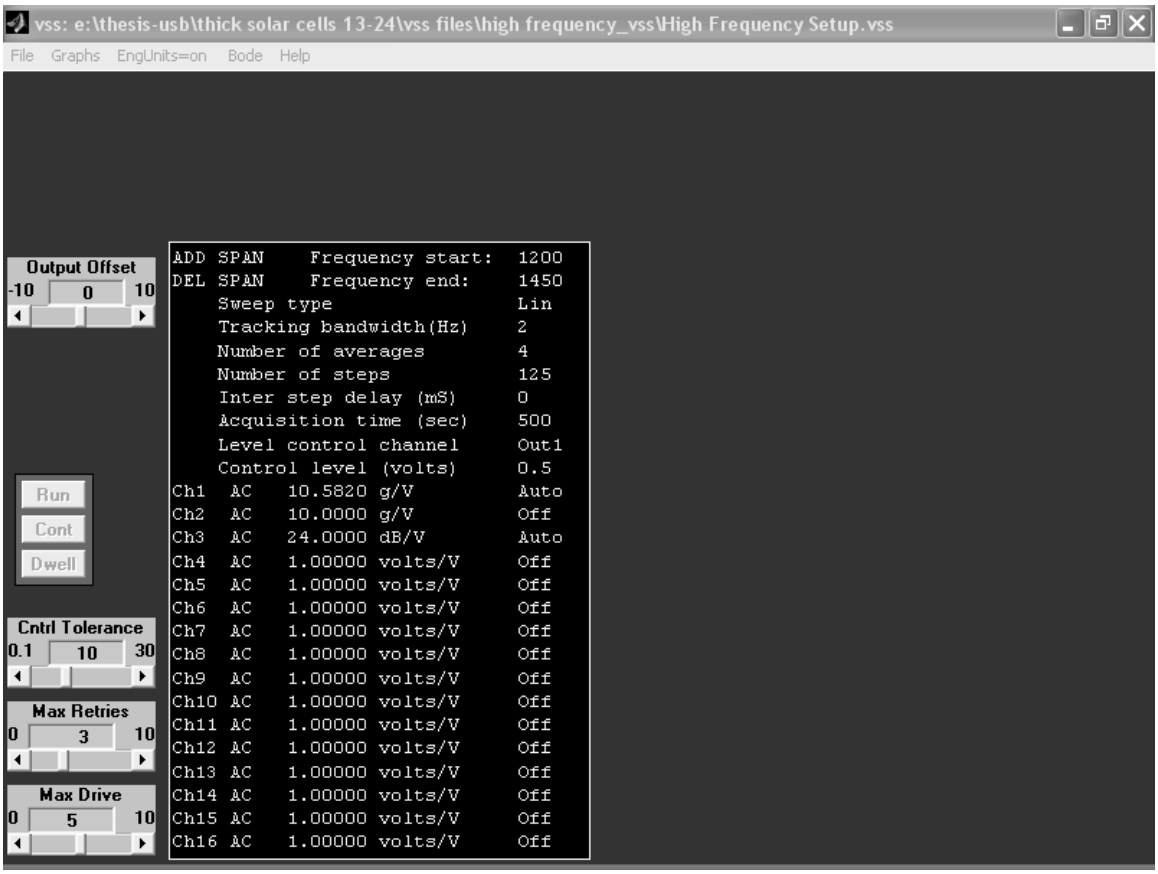

Figure 34. SigLab vss setup file for narrowband range 1200-1450 Hz.

APPENDIX D: RUN ORDER OF SOLAR CELL SPECIMENS OVER THE BROADBAND RANGE OF 1200-1450 HZ

Table 8. Run order of specimens over the broad-band range of 1200-1450 Hz.

Specimen Number	Run Order
13	5
14	4
15	12
16	8
17	6
18	10
19	3
20	1
21	11
22	7
23	9
24	2

APPENDIX E: FREQUENCY RESPONSE PLOTS OF SOLAR CELL SPECIMENS OVER THE BROADBAND RANGE OF 400-1800 HZ

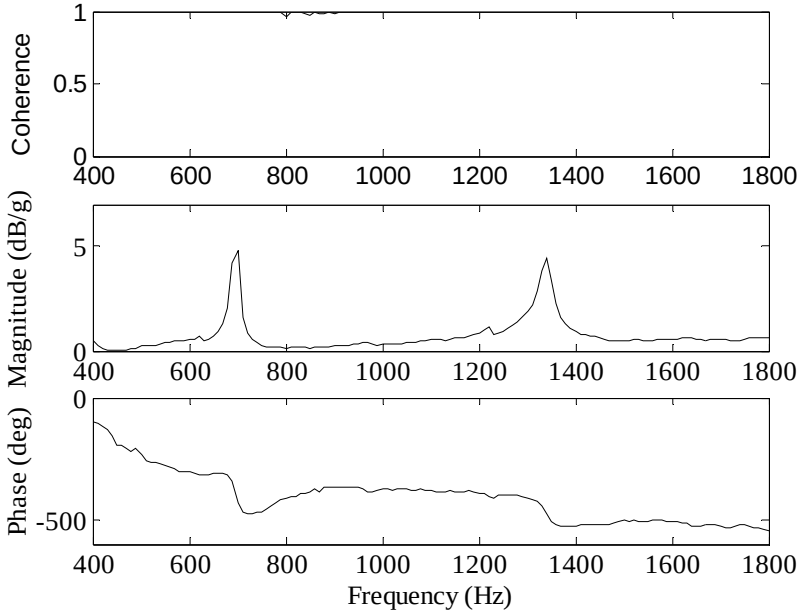

Figure 35. Frequency response plot of solar cell 13 over the broadband range of 1200-1450 Hz.

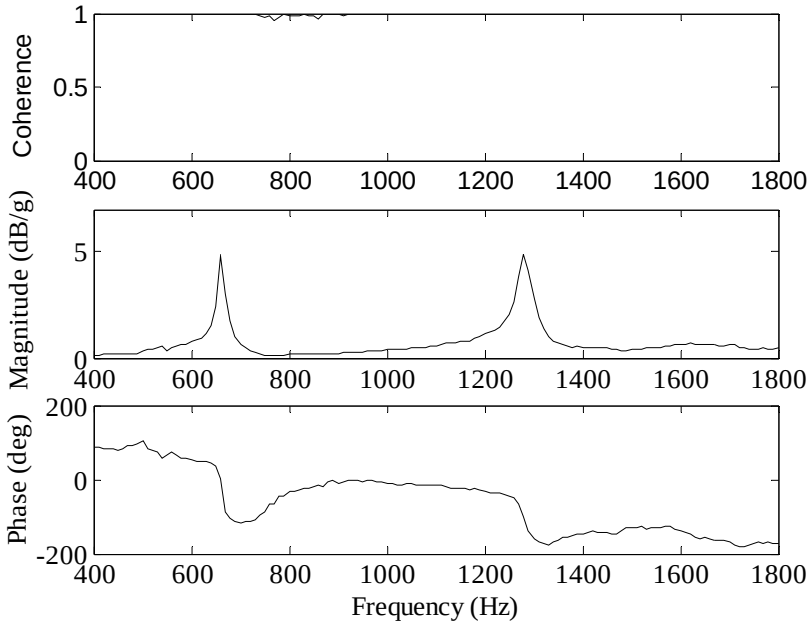

Figure 36. Frequency response plot of solar cell 14 over the broadband range of 1200-1450 Hz.

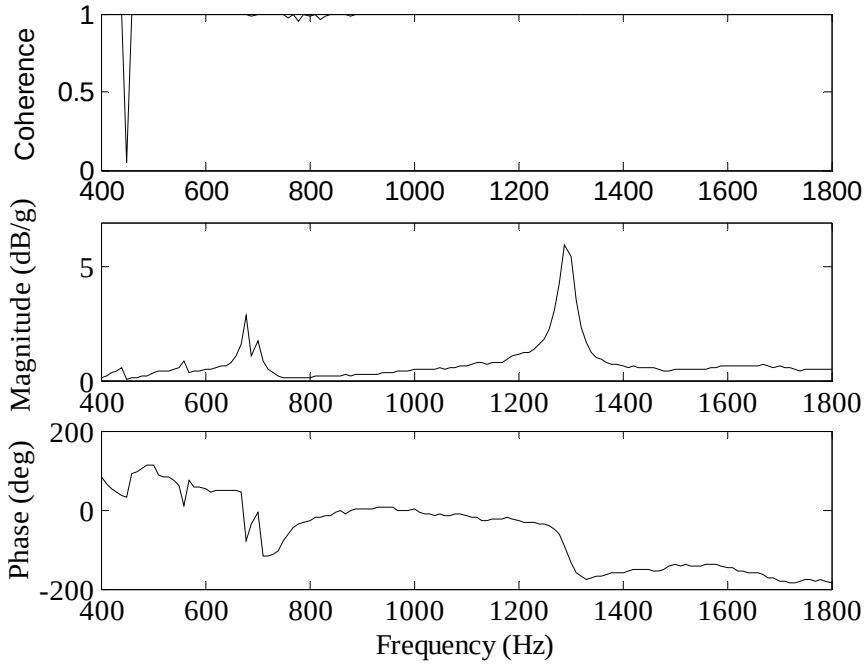

Figure 37. Frequency response plot of solar cell 15 over the broadband range of 1200-1450 Hz.

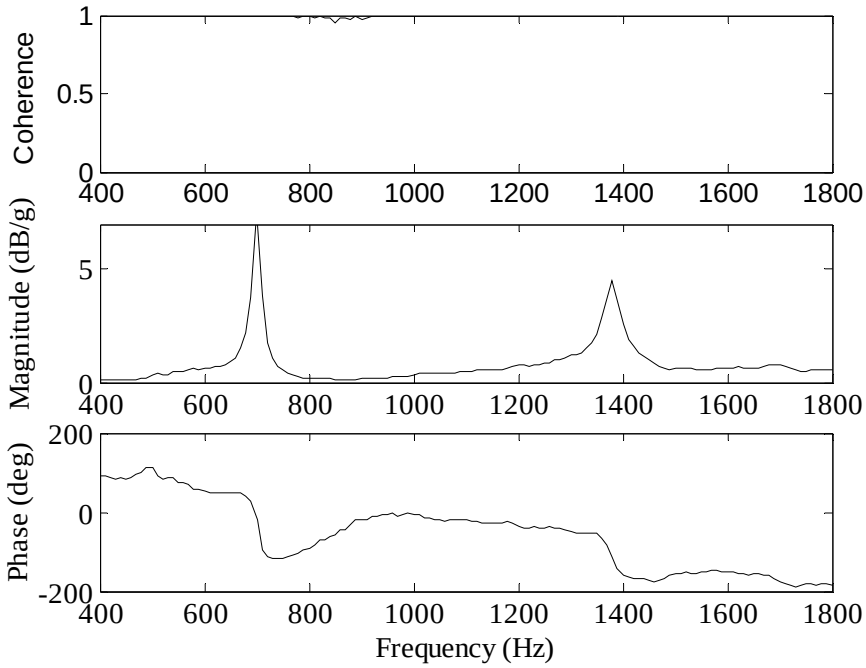

Figure 38. Frequency response plot of solar cell 16 over the broadband range of 1200-1450 Hz.

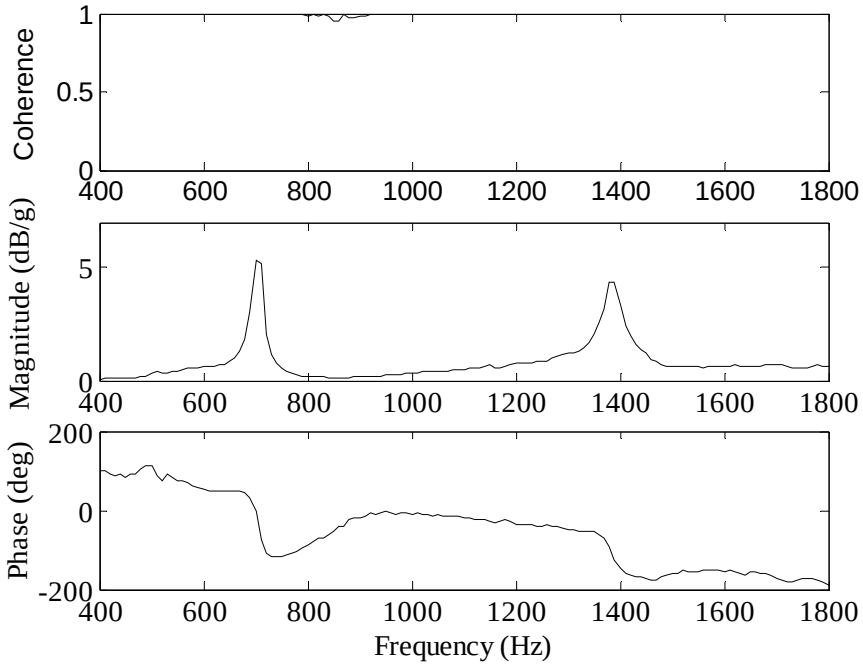

Figure 39. Frequency response plot of solar cell 17 over the broadband range of 1200-1450 Hz.

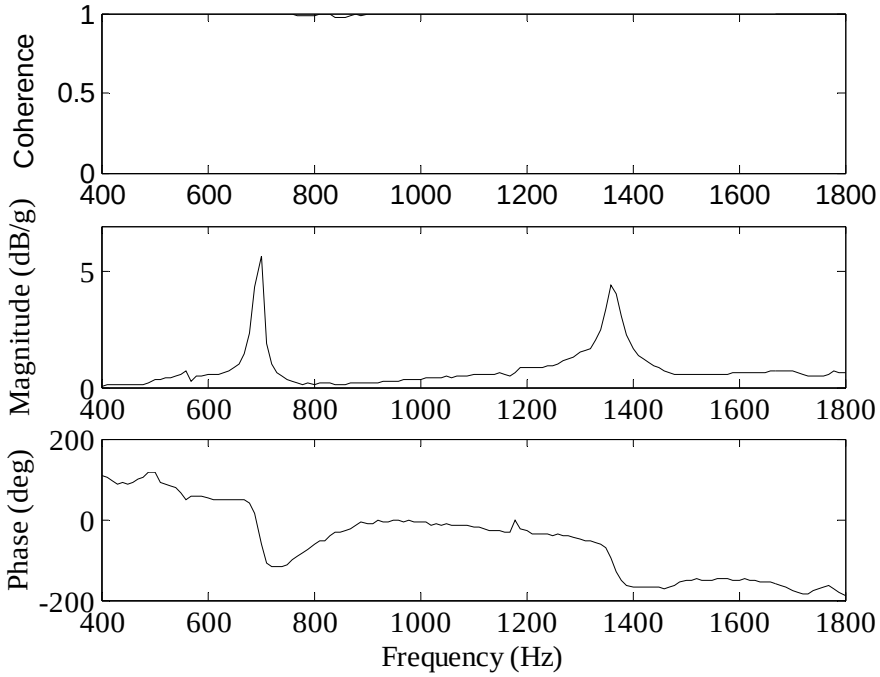

Figure 40. Frequency response plot of solar cell 18 over the broadband range of 1200-1450 Hz.

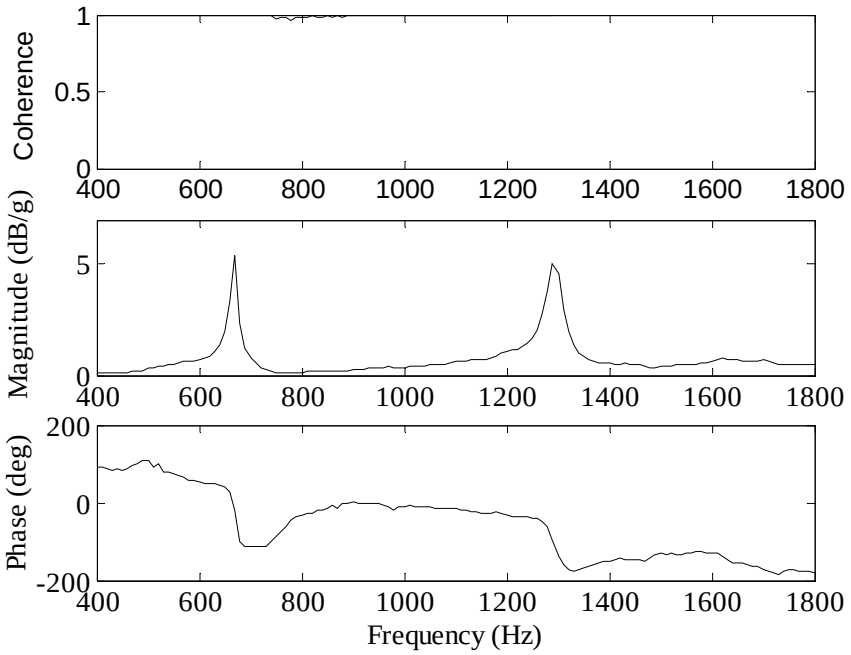

Figure 41. Frequency response plot of solar cell 19 over the broadband range of 1200-1450 Hz.

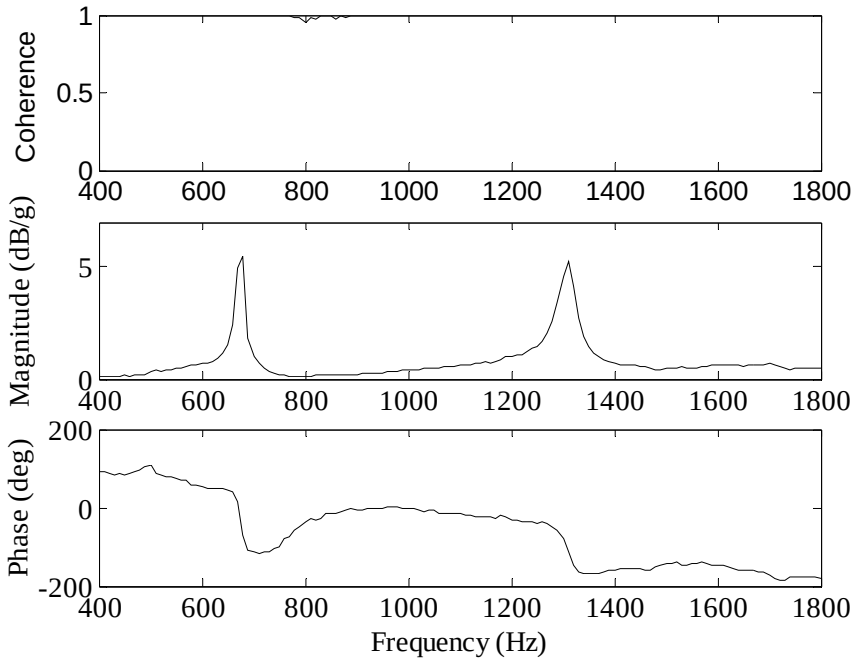

Figure 42. Frequency response plot of solar cell 20 over the broadband range of 1200-1450 Hz.

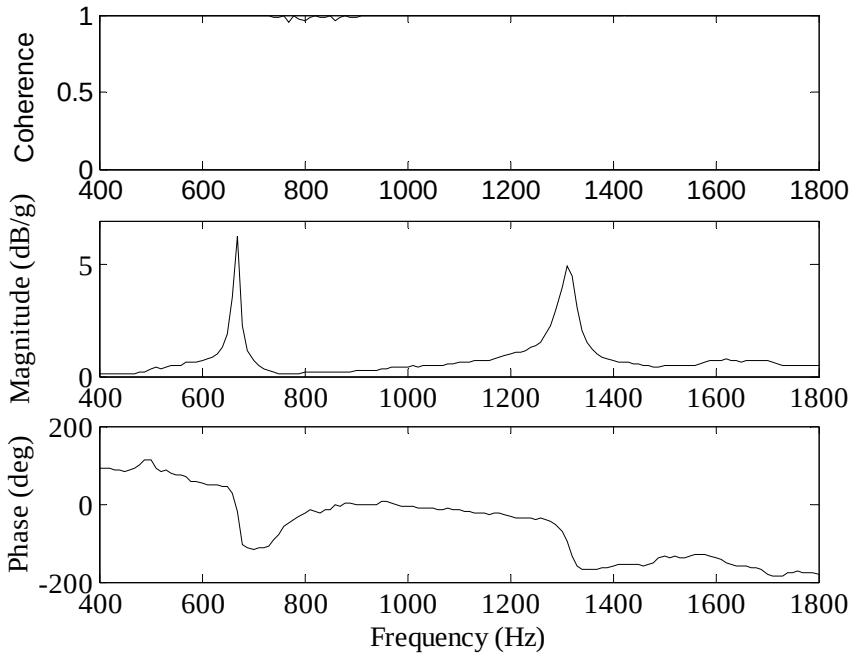

Figure 43. Frequency response plot of solar cell 21 over the broadband range of 1200-1450 Hz.

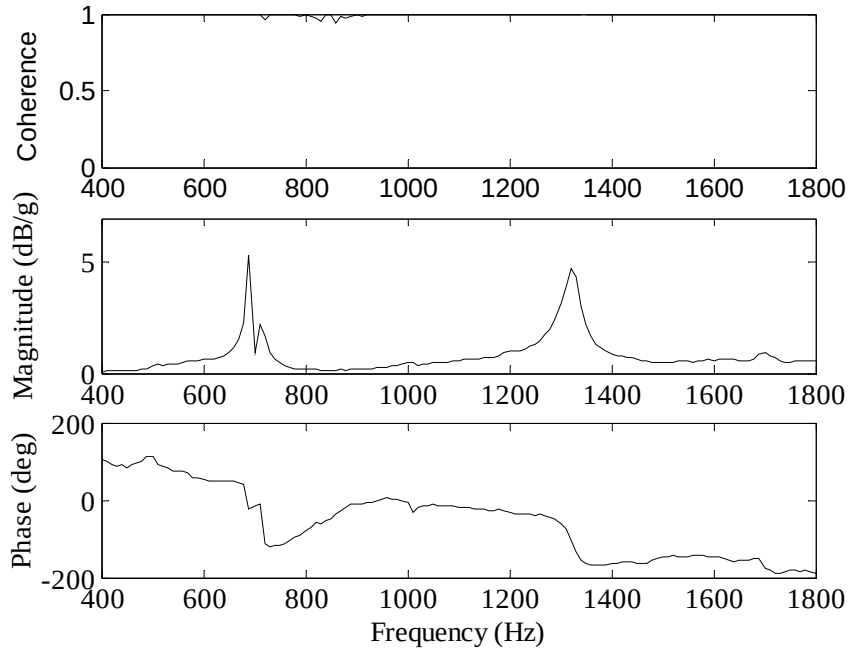

Figure 44. Frequency response plot of solar cell 22 over the broadband range of 1200-1450 Hz.

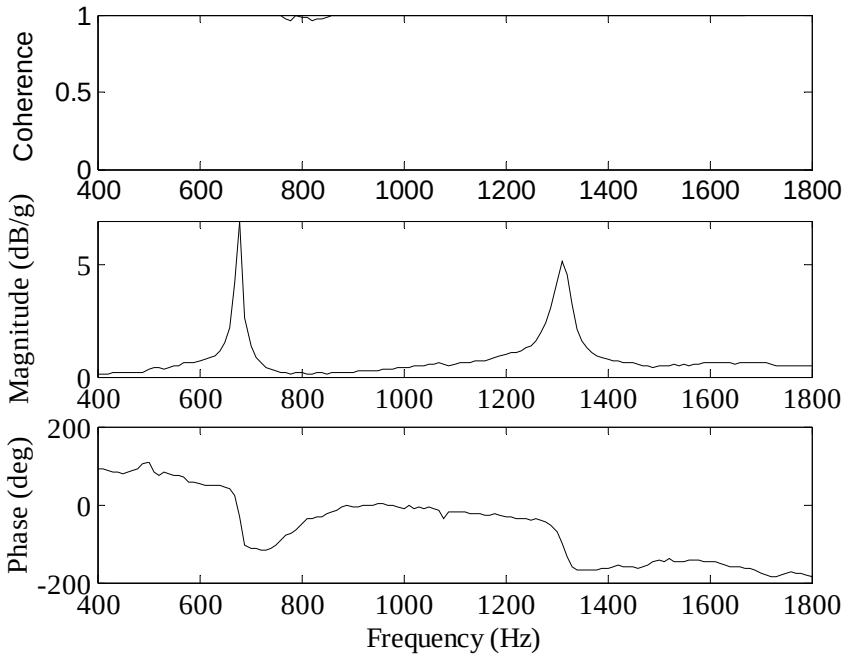

Figure 45. Frequency response plot of solar cell 23 over the broadband range of 1200-1450 Hz.

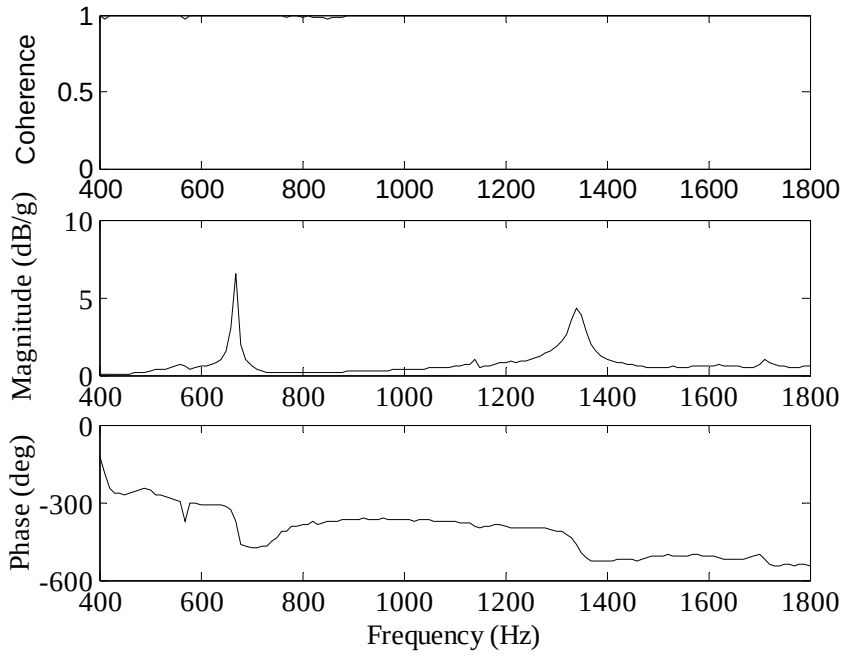

Figure 46. Frequency response plot of solar cell 24 over the broadband range of 1200-1450 Hz.

APPENDIX F: RANDOMIZATION AND RUN ORDER OF SOLAR CELL SPECIMENS OVER THE NARROWBAND RANGES

Table 9. Solar cell specimens with associated run number for narrowband range 600-750 Hz.

Specimen	Experimental Run Number		
13	1	2	3
14	4	5	6
15	7	8	9
16	10	11	12
17	13	14	15
18	16	17	18
19	19	20	21
20	22	23	24
21	25	26	27
22	28	29	30
23	31	32	33
24	34	35	36

APPENDIX F (Continued)

Table 10. Randomized ordering of specimens for the narrowband range of 600-750 Hz.

Experimental Run Number	Random Number in Ascending Order	Run Order	Specimen Number
31	268	1	23
19	285	2	19
5	297	3	14
18	323	4	18
23	466	5	20
12	668	6	16
10	718	7	16
8	746	8	15
13	796	9	17
32	820	10	23
7	829	11	15
16	885	12	18
11	1016	13	16
15	1063	14	17
2	1075	15	13
24	1102	16	20
17	1125	17	18
29	1161	18	22
35	1171	19	24
3	1257	20	13
1	1273	21	13
9	1299	22	15
6	1348	23	14
26	1372	24	21
33	1409	25	23
27	1418	26	21
21	1449	27	19
34	1502	28	24
14	1531	29	17
36	1644	30	24
25	1649	31	21
20	1670	32	19
28	1708	33	22

Table 10. (Continued)

Experimental Run Number	Random Number in Ascending Order	Run Order	Specimen Number
4	1826	34	14
22	1898	35	20
30	1903	36	22

Table 11. Randomized ordering of specimens for the narrowband range of 1200-1450 Hz.

Experimental Run Number	Random Number in Ascending Order	Run Order	Specimen Number
10	1	1	16
36	202	2	24
32	418	3	23
31	455	4	23
20	471	5	19
25	475	6	21
19	649	7	19
7	1016	8	15
29	1023	9	22
21	1115	10	19
30	1193	11	22
26	1321	12	21
24	1412	13	20
2	1416	14	13
12	1711	15	16
28	1722	16	22
34	1796	17	24
15	2180	18	17
18	2228	19	18
16	2395	20	18
5	2508	21	14
17	2734	22	18
11	3122	23	16
27	3572	24	21
8	3663	25	15

Table 11. (Continued)

Experimental Run Number	Random Number in Ascending Order	Run Order	Specimen Number
9	3743	26	15
4	3805	27	14
3	3822	28	13
1	4199	29	13
13	4213	30	17
23	4979	31	20
14	5260	32	17
35	5525	33	24
22	5713	34	20
33	5743	35	23
6	5984	36	14

APPENDIX G: FREQUENCY RESPONSE PLOTS OF SOLAR CELL SPECIMENS OVER THE NARROWBAND RANGE OF 600-750 HZ

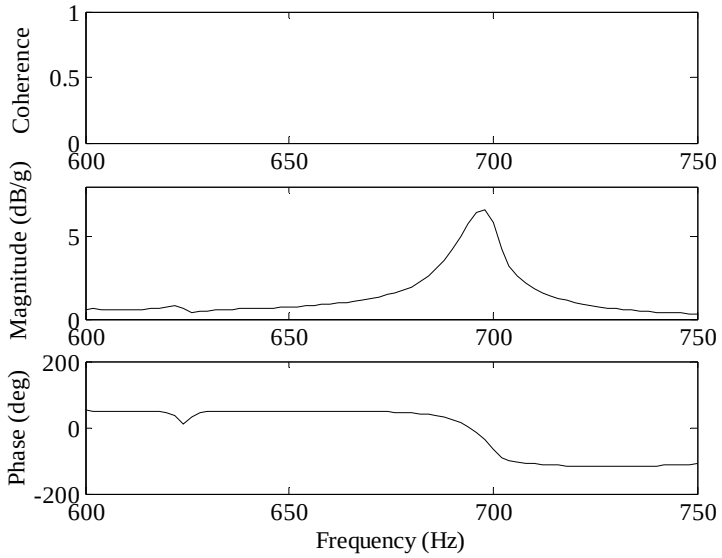

Figure 47. Frequency response plot of solar cell specimen 13 over the narrowband range of 600-750 Hz; experimental run number 1.

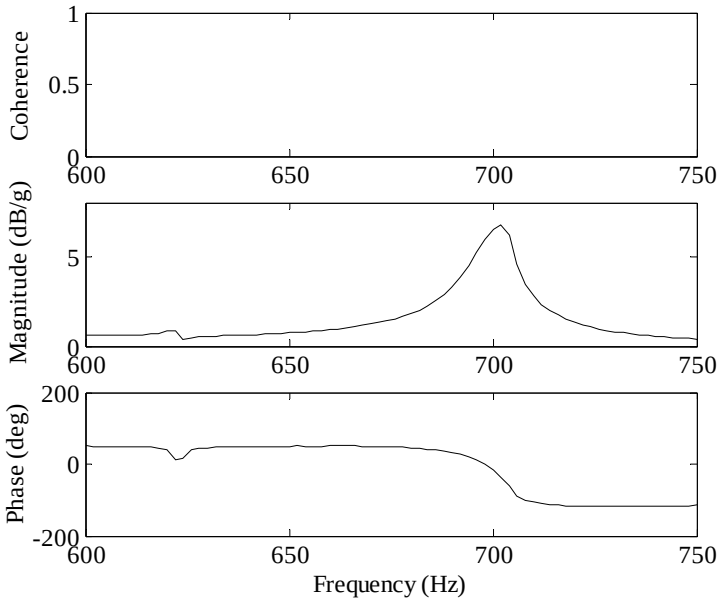

Figure 48. Frequency response plot of solar cell specimen 13 over the narrowband range of 600-750 Hz; experimental run number 2.

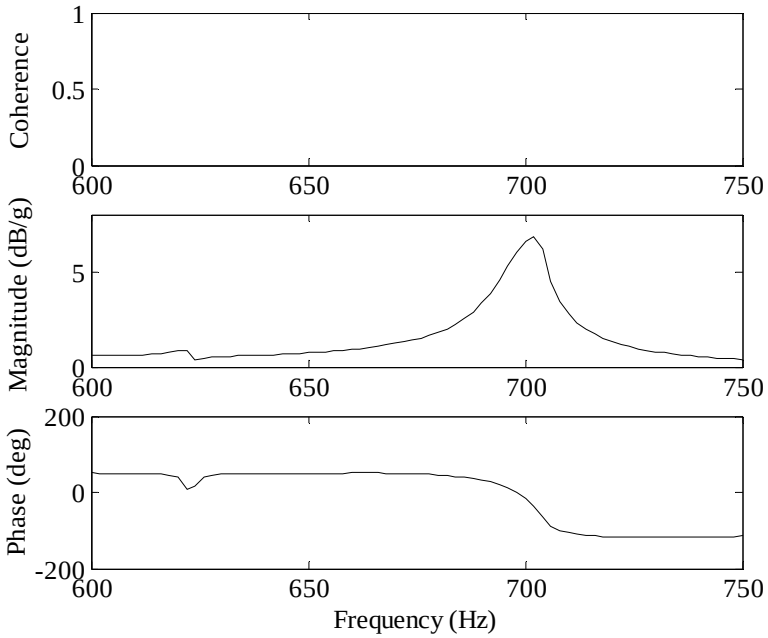

Figure 49. Frequency response plot of solar cell specimen 13 over the narrowband range of 600-750 Hz; experimental run number 3.

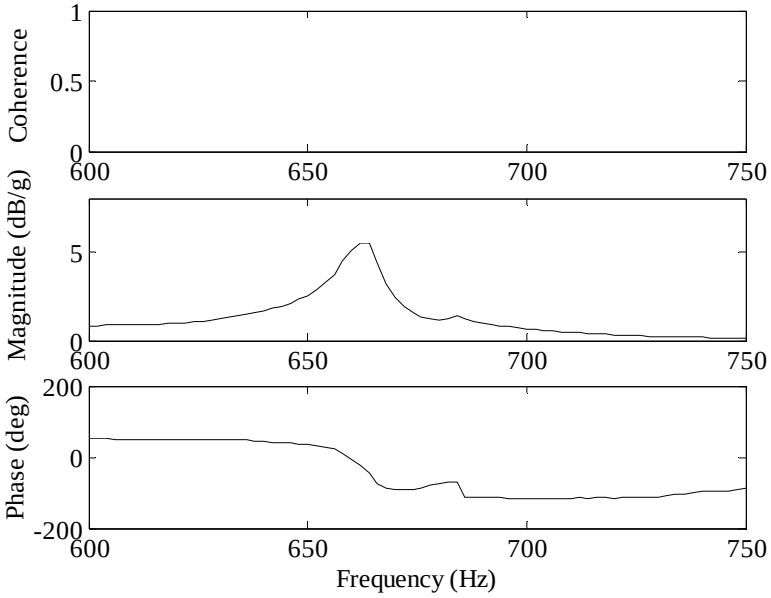

Figure 50. Frequency response plot of solar cell specimen 14 over the narrowband range of 600-750 Hz; experimental run number 4.

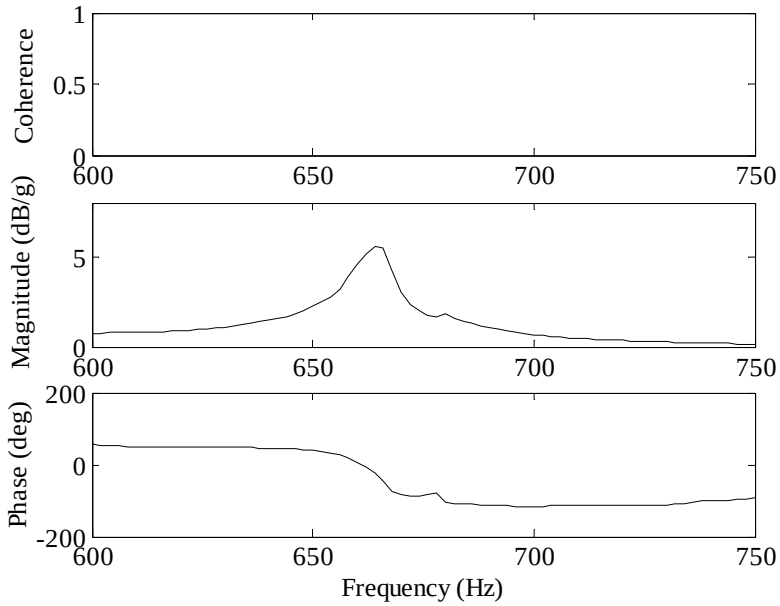

Figure 51. Frequency response plot of solar cell specimen 14 over the narrowband range of 600-750 Hz; experimental run number 5.

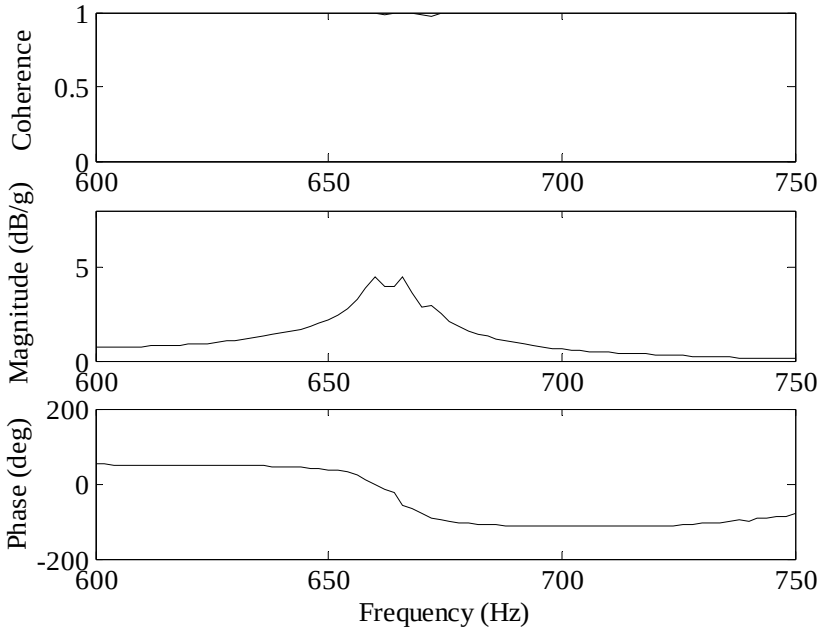

Figure 52. Frequency response plot of solar cell specimen 14 over the narrowband range of 600-750 Hz; experimental run number 6.

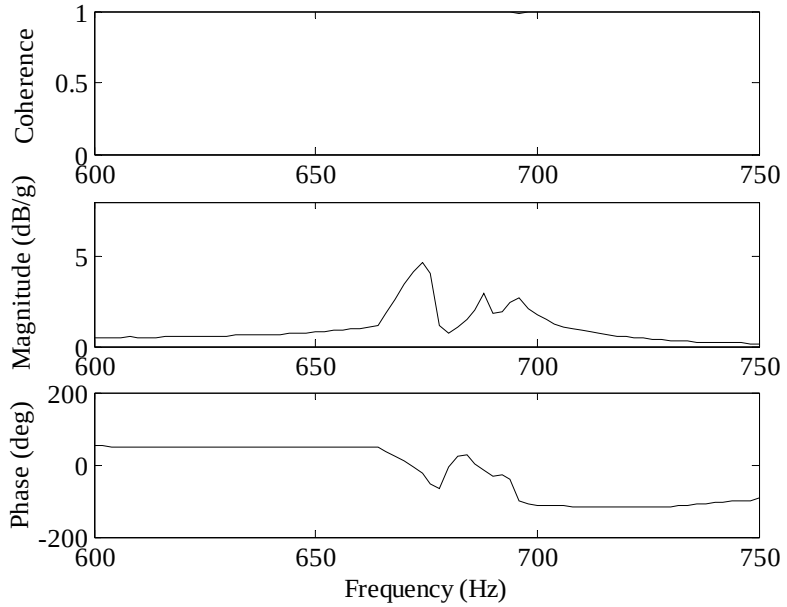

Figure 53. Frequency response plot of solar cell specimen 15 over the narrowband range of 600-750 Hz; experimental run number 7.

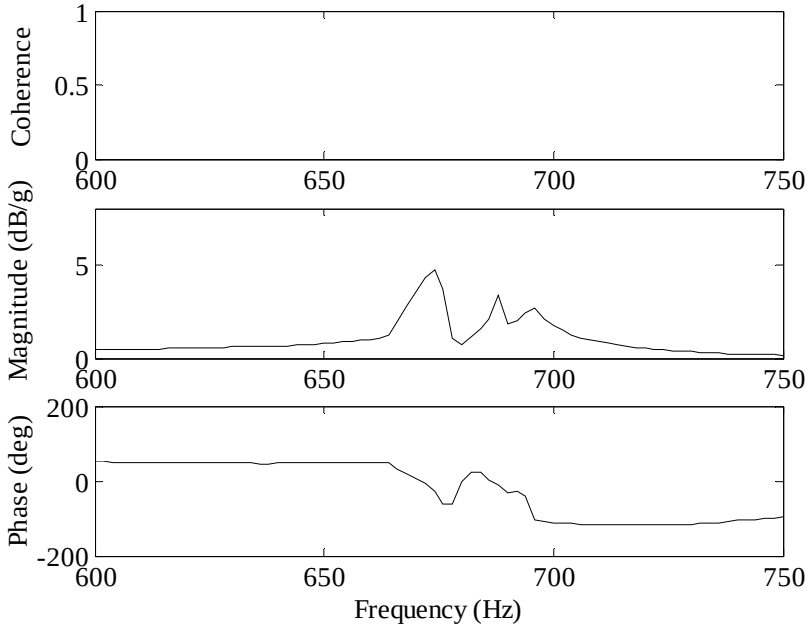

Figure 54. Frequency response plot of solar cell specimen 15 over the narrowband range of 600-750 Hz; experimental run number 8.

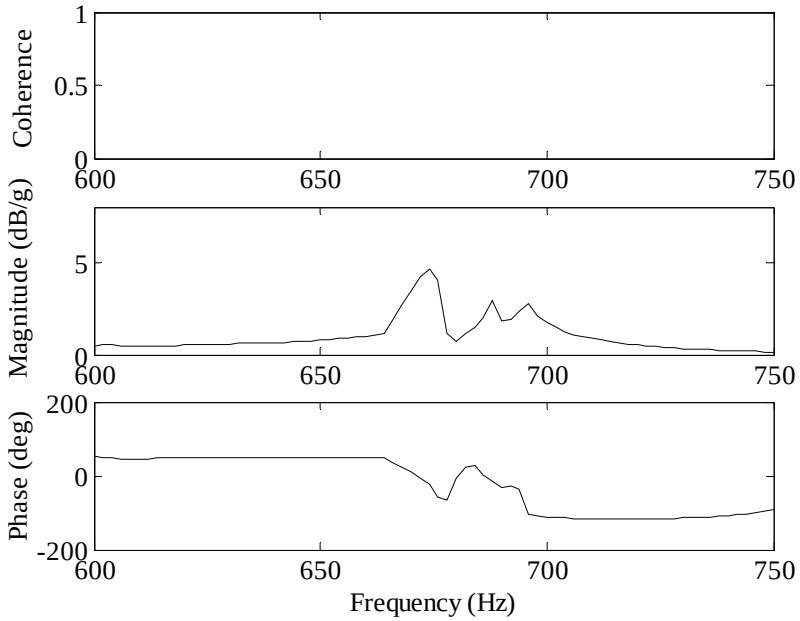

Figure 55. Frequency response plot of solar cell specimen 15 over the narrowband range of 600-750 Hz; experimental run number 9.

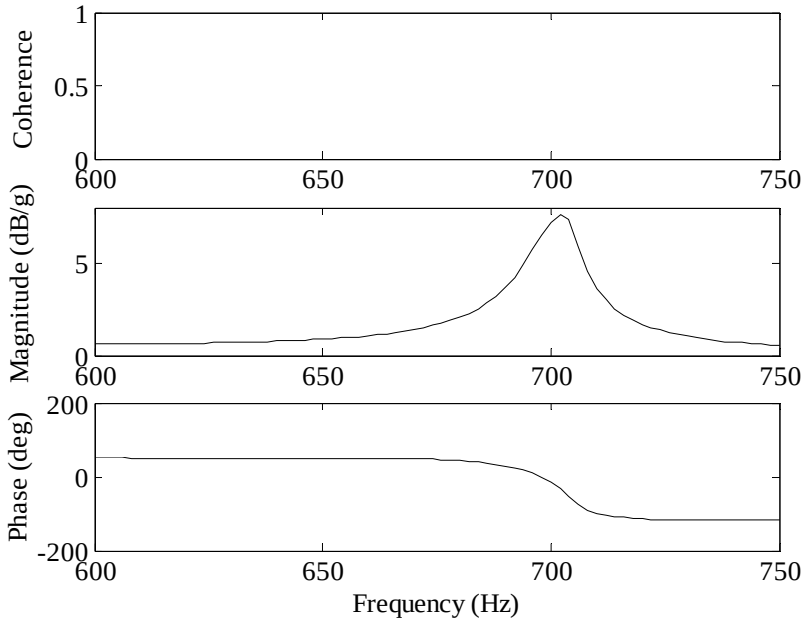

Figure 56. Frequency response plot of solar cell specimen 16 over the narrowband range of 600-750 Hz; experimental run number 10.

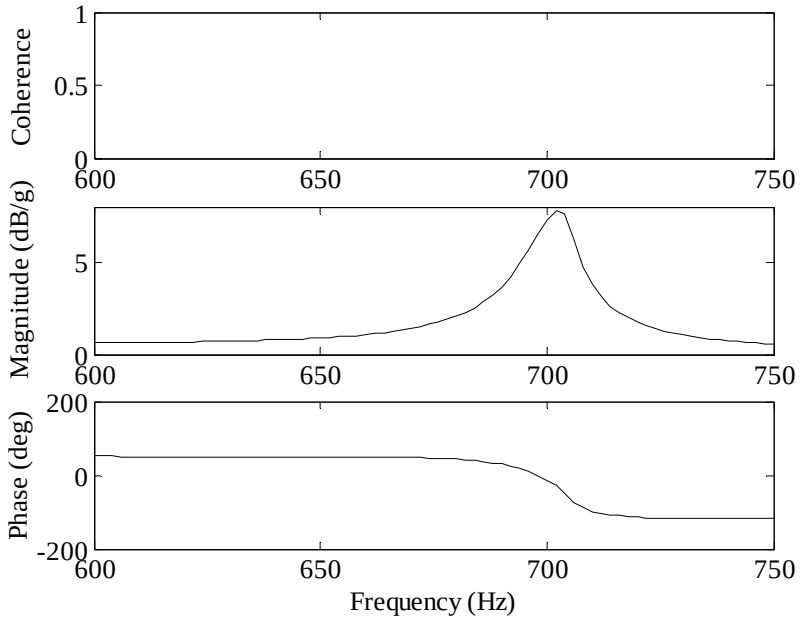

Figure 57. Frequency response plot of solar cell specimen 16 over the narrowband range of 600-750 Hz; experimental run number 11.

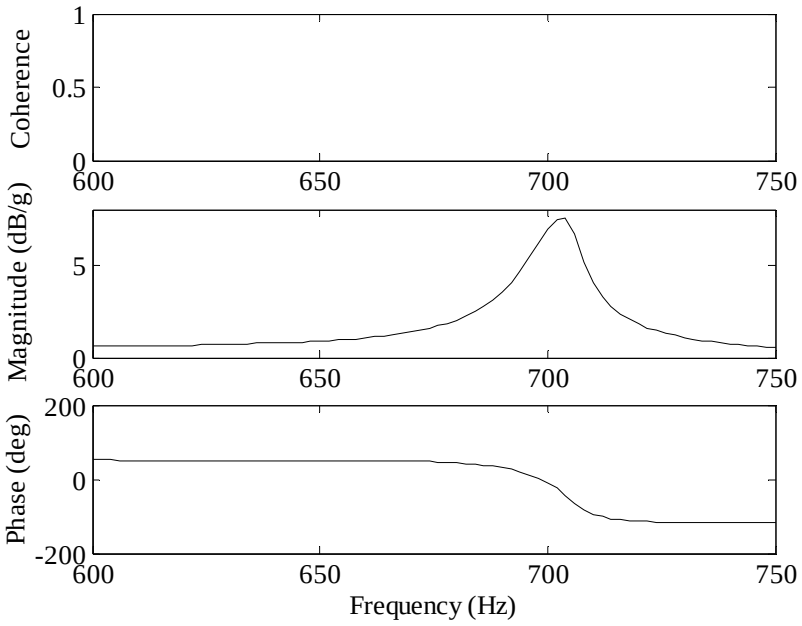

Figure 58. Frequency response plot of solar cell specimen 16 over the narrowband range of 600-750 Hz; experimental run number 12.

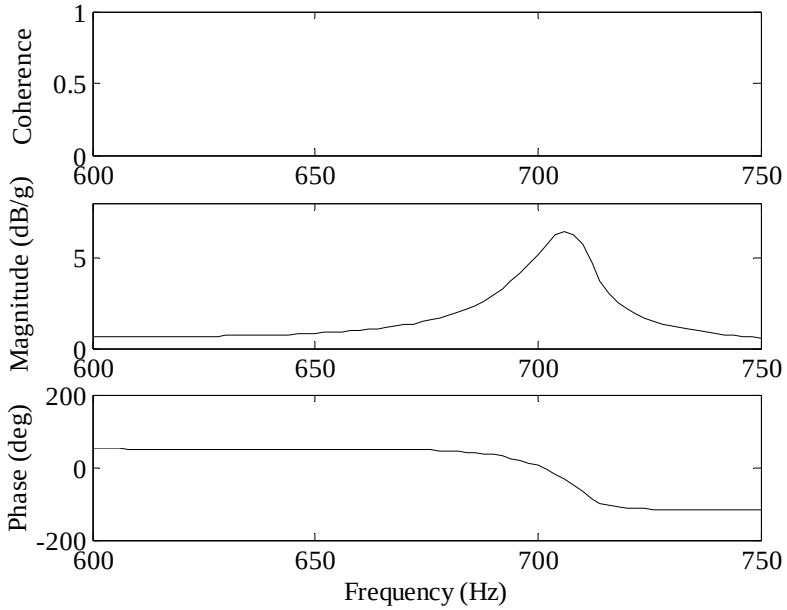

Figure 59. Frequency response plot of solar cell specimen 17 over the narrowband range of 600-750 Hz; experimental run number 13.

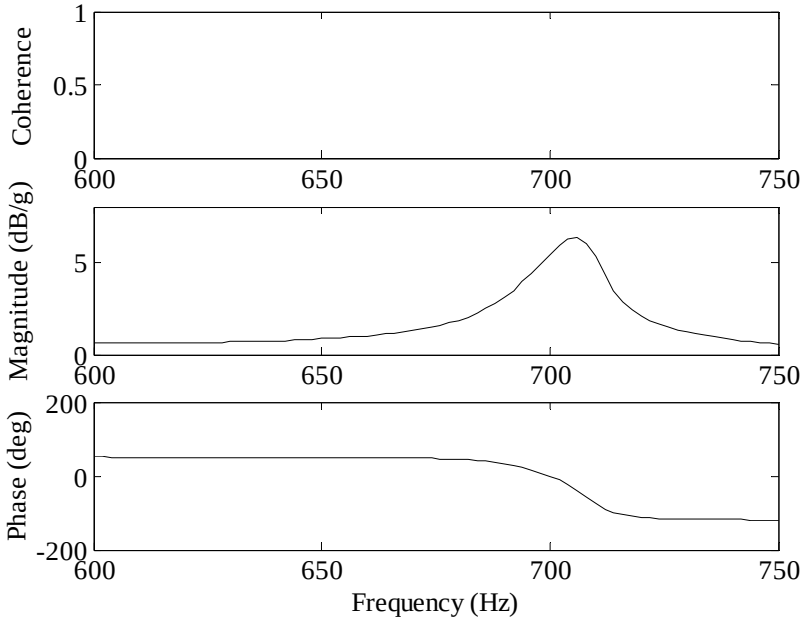

Figure 60. Frequency response plot of solar cell specimen 17 over the narrowband range of 600-750 Hz; experimental run number 14.

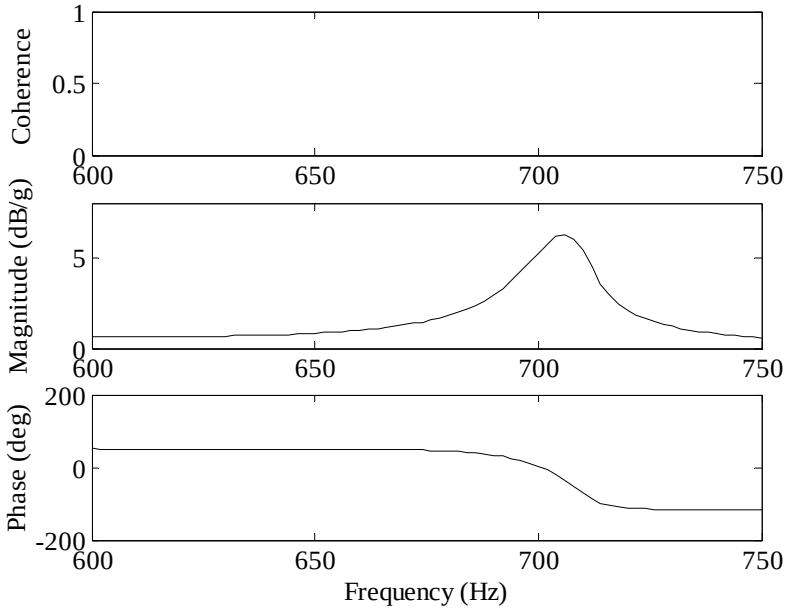

Figure 61. Frequency response plot of solar cell specimen 17 over the narrowband range of 600-750 Hz; experimental run number 15.

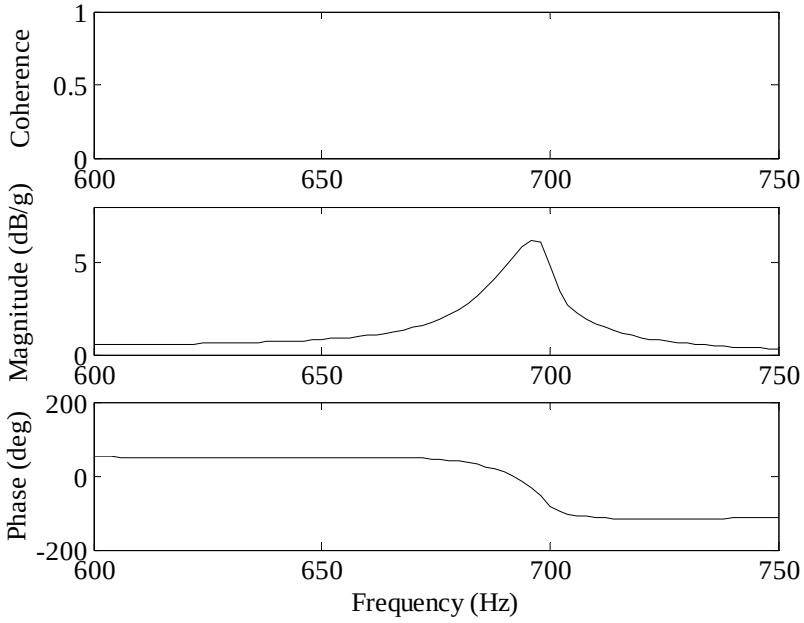

Figure 62. Frequency response plot of solar cell specimen 18 over the narrowband range of 600-750 Hz; experimental run number 16.

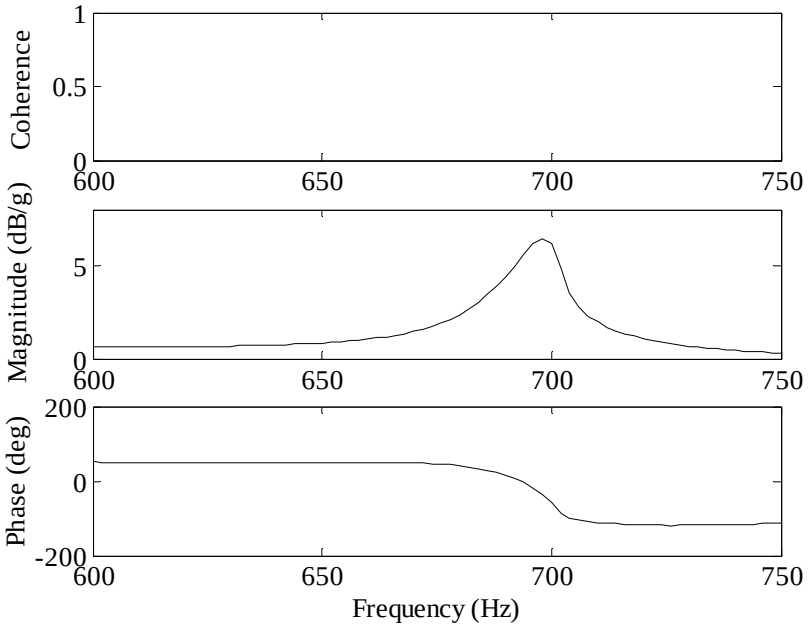

Figure 63. Frequency response plot of solar cell specimen 18 over the narrowband range of 600-750 Hz; experimental run number 17.

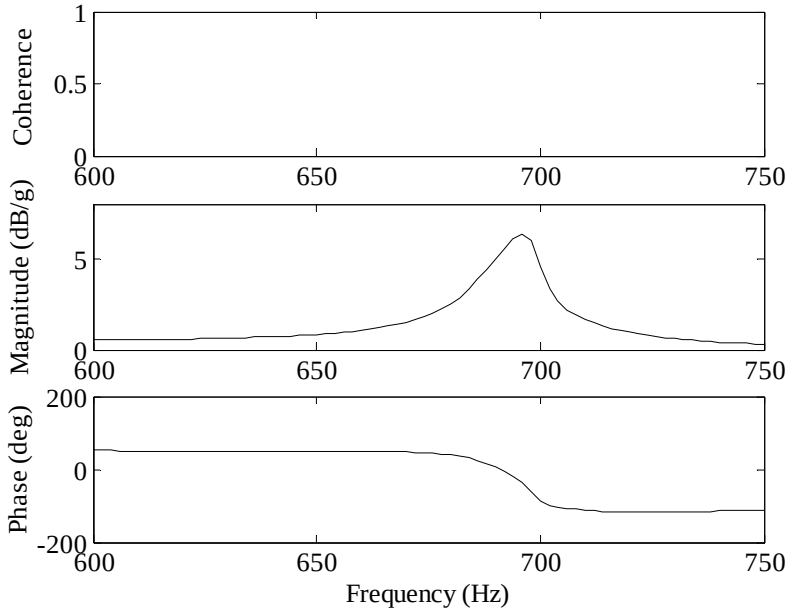

Figure 64. Frequency response plot of solar cell specimen 18 over the narrowband range of 600-750 Hz; experimental run number 18.

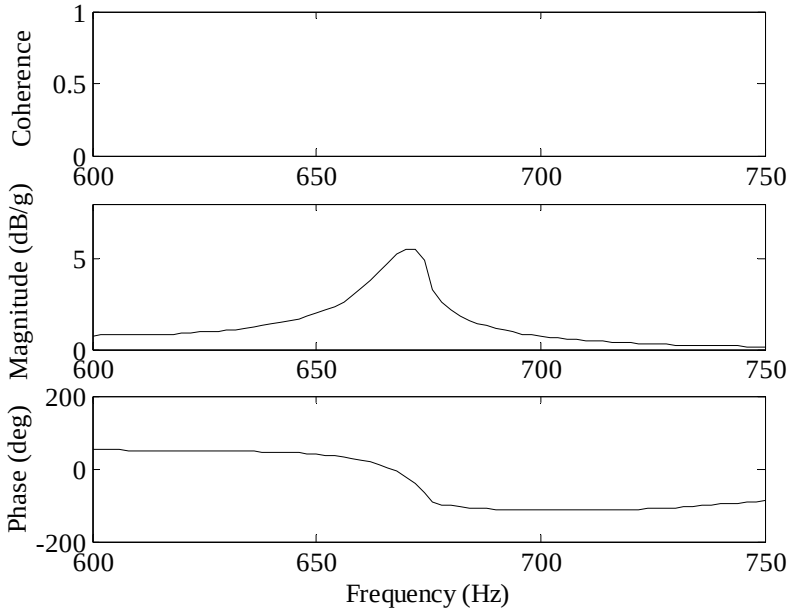

Figure 65. Frequency response plot of solar cell specimen 19 over the narrowband range of 600-750 Hz; experimental run number 19.

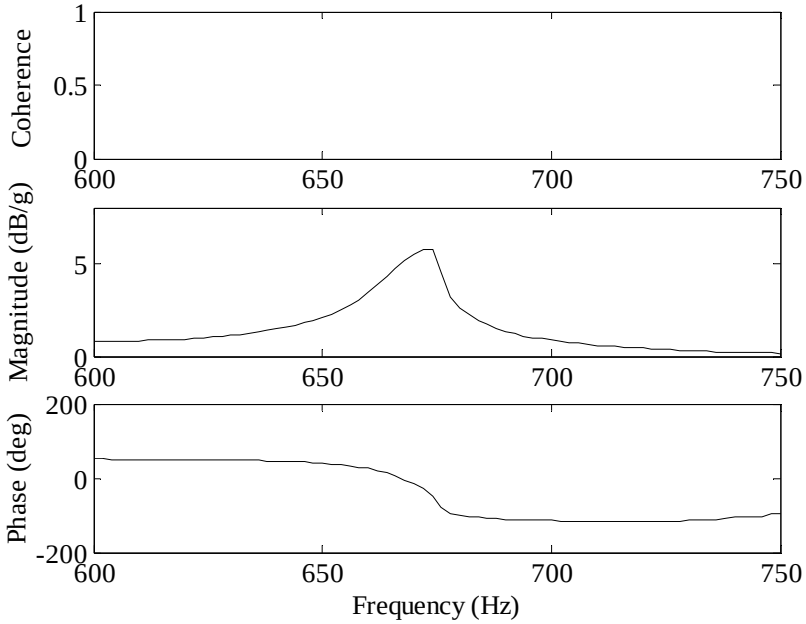

Figure 66. Frequency response plot of solar cell specimen 19 over the narrowband range of 600-750 Hz; experimental run number 20.

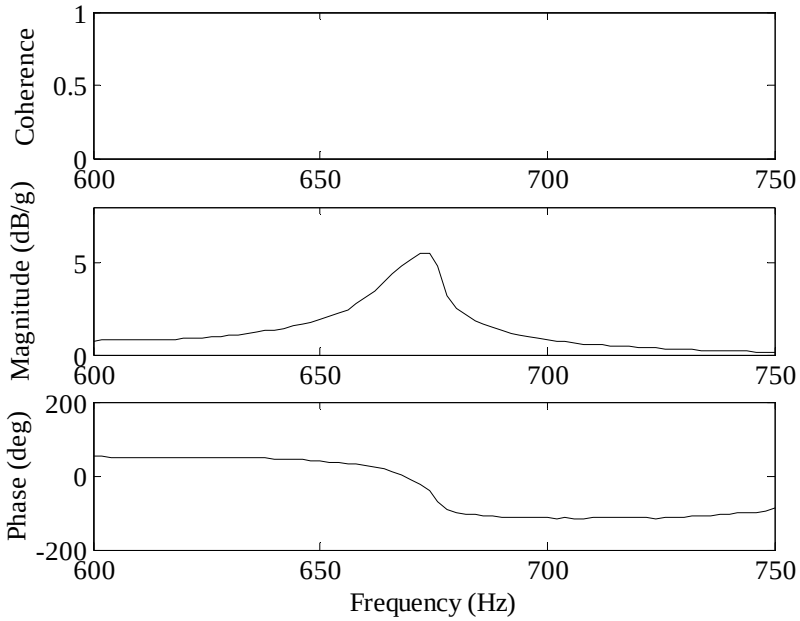

Figure 67. Frequency response plot of solar cell specimen 19 over the narrowband range of 600-750 Hz; experimental run number 21.

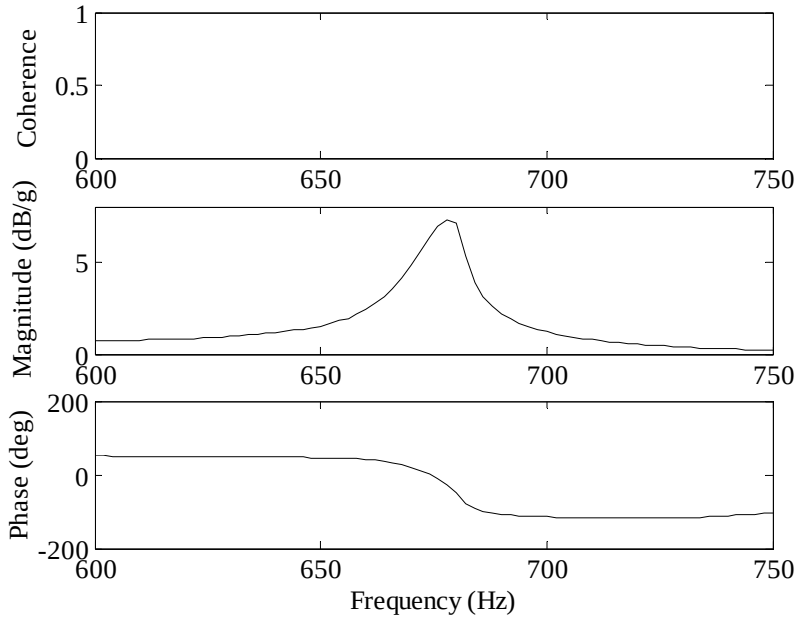

Figure 68. Frequency response plot of solar cell specimen 20 over the narrowband range of 600-750 Hz; experimental run number 22.

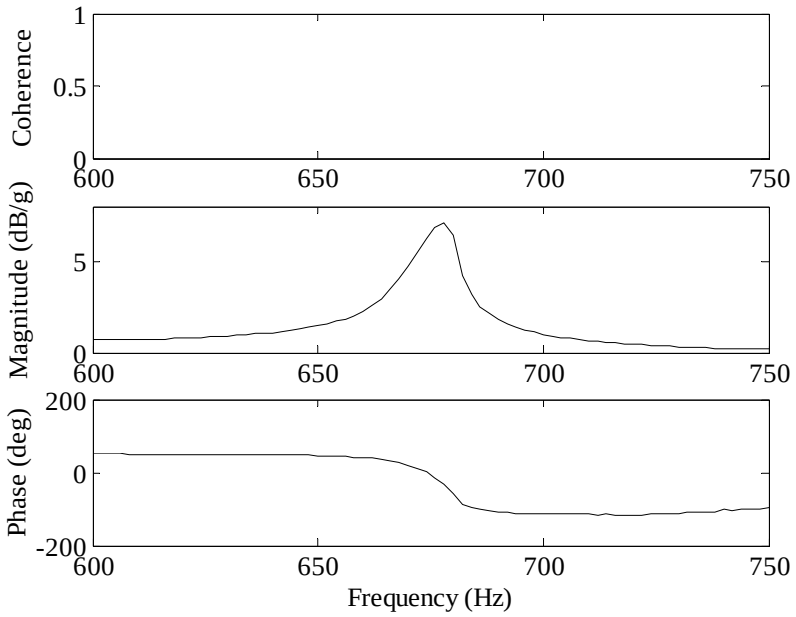

Figure 69. Frequency response plot of solar cell specimen 20 over the narrowband range of 600-750 Hz; experimental run number 23.

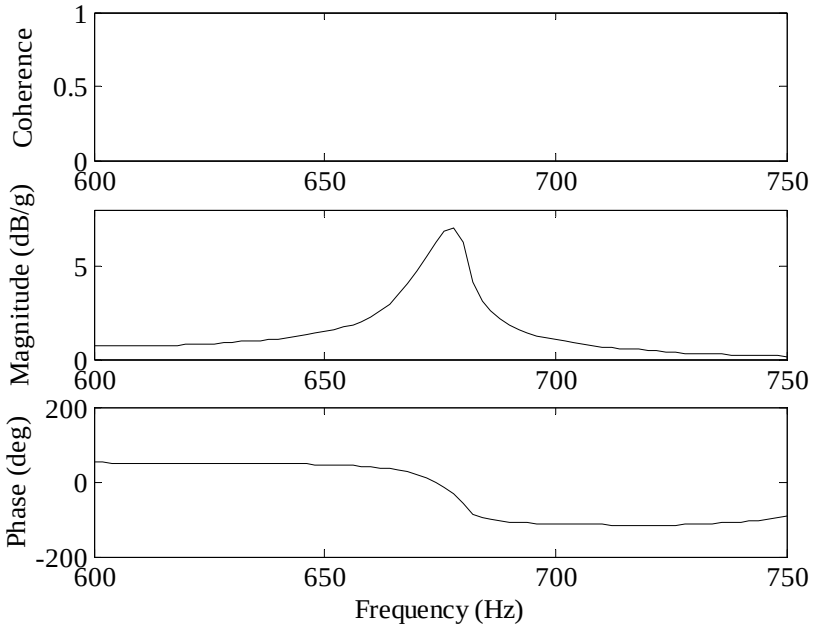

Figure 70. Frequency response plot of solar cell specimen 20 over the narrowband range of 600-750 Hz; experimental run number 24.

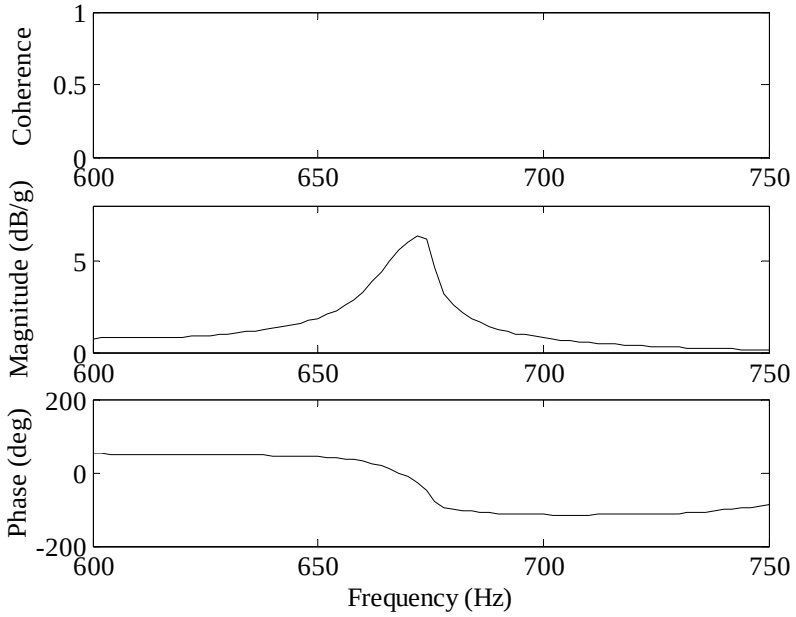

Figure 71. Frequency response plot of solar cell specimen 21 over the narrowband range of 600-750 Hz; experimental run number 25.

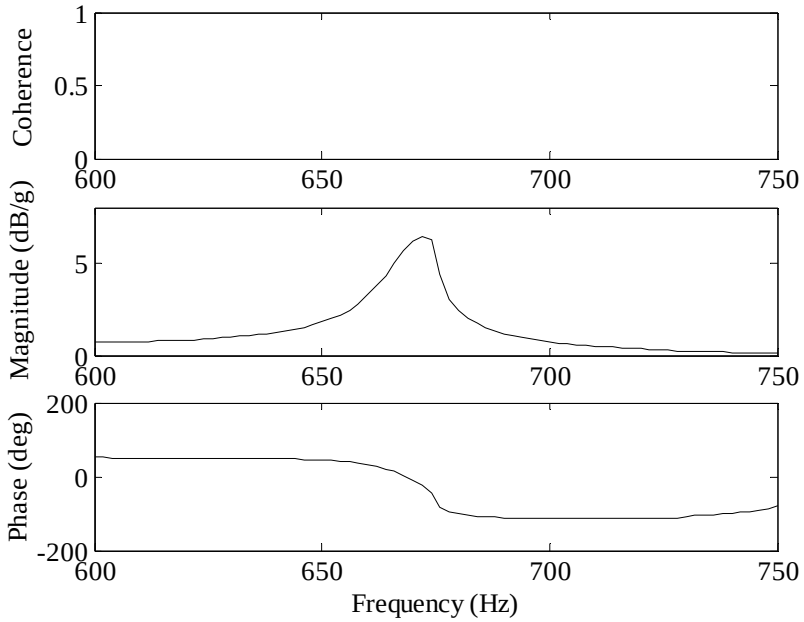

Figure 72. Frequency response plot of solar cell specimen 21 over the narrowband range of 600-750 Hz; experimental run number 26.

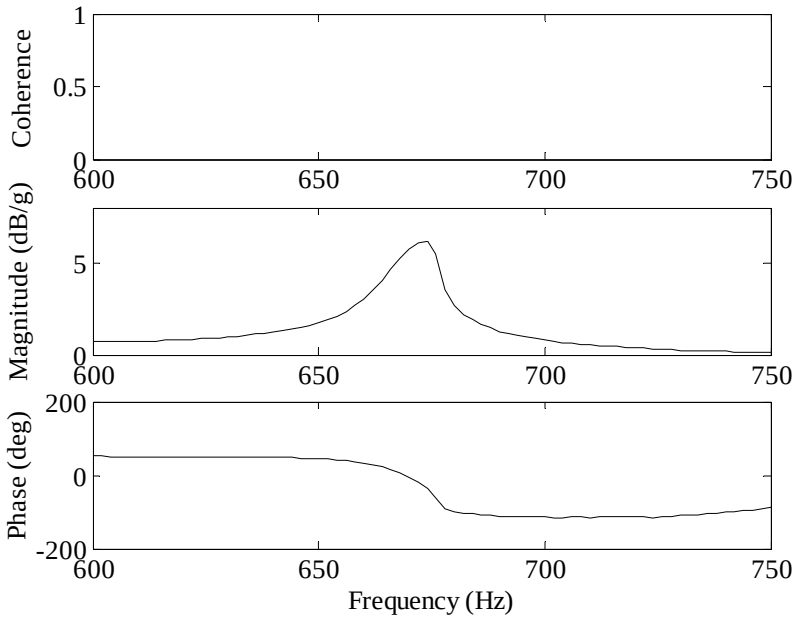

Figure 73. Frequency response plot of solar cell specimen 21 over the narrowband range of 600-750 Hz; experimental run number 27.

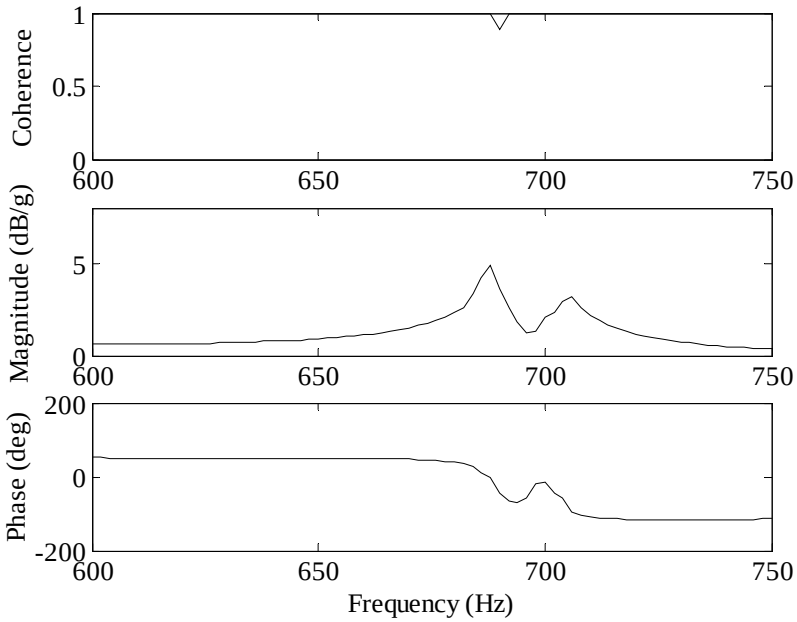

Figure 74. Frequency response plot of solar cell specimen 22 over the narrowband range of 600-750 Hz; experimental run number 28.

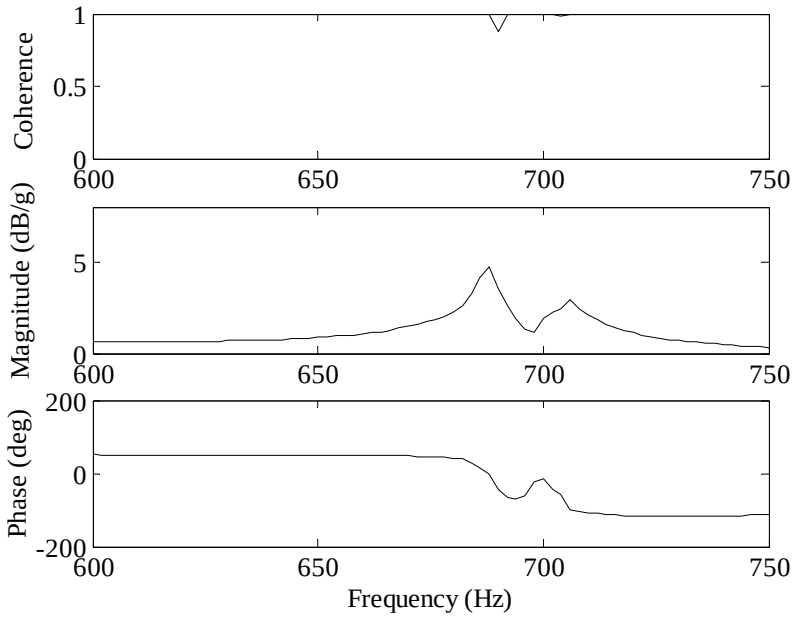

Figure 75. Frequency response plot of solar cell specimen 22 over the narrowband range of 600-750 Hz; experimental run number 29.

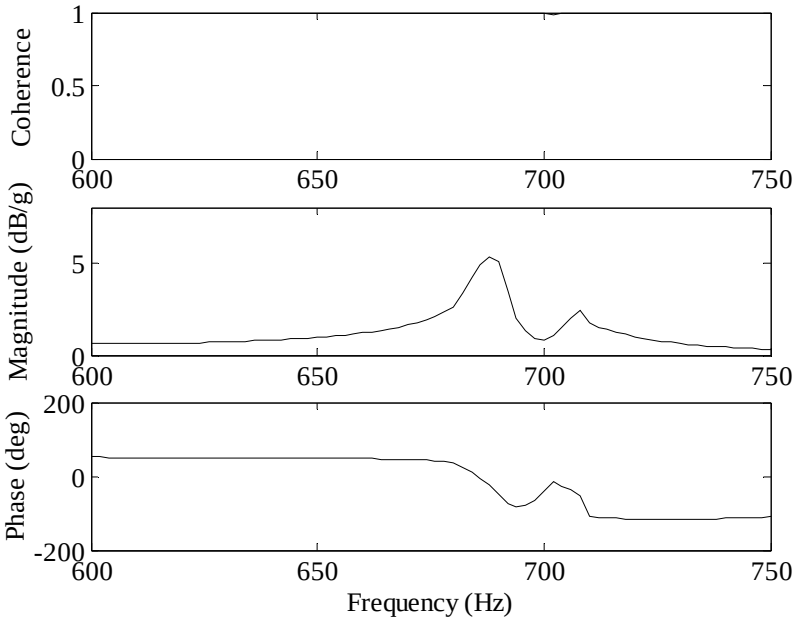

Figure 76. Frequency response plot of solar cell specimen 22 over the narrowband range of 600-750 Hz; experimental run number 30.

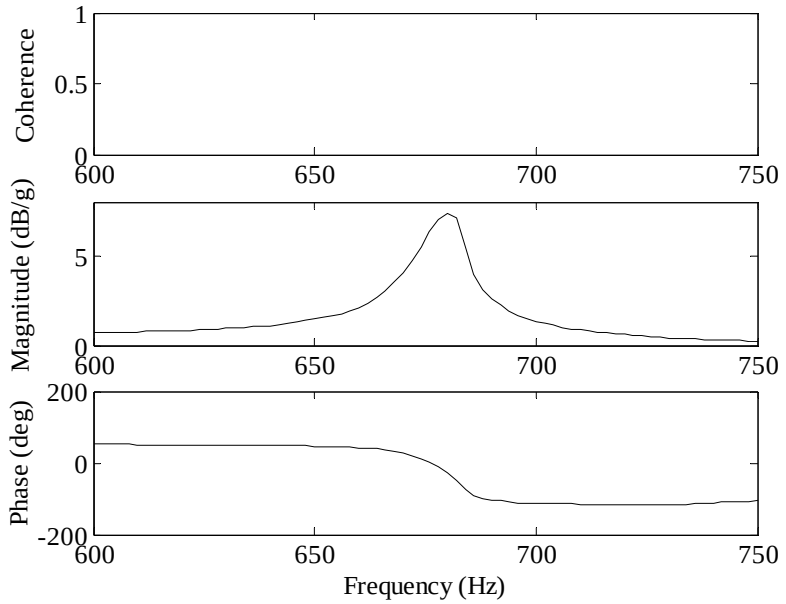

Figure 77. Frequency response plot of solar cell specimen 23 over the narrowband range of 600-750 Hz; experimental run number 31.

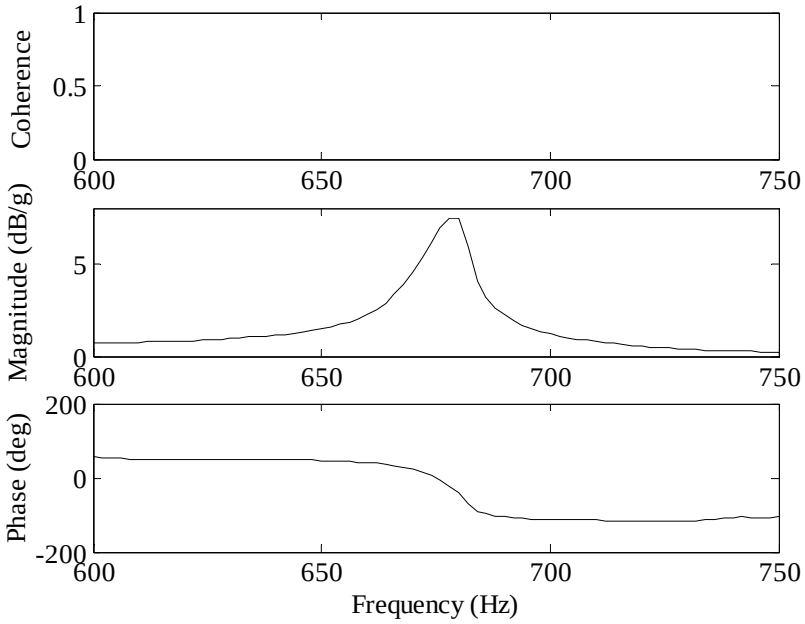

Figure 78. Frequency response plot of solar cell specimen 23 over the narrowband range of 600-750 Hz; experimental run number 32.

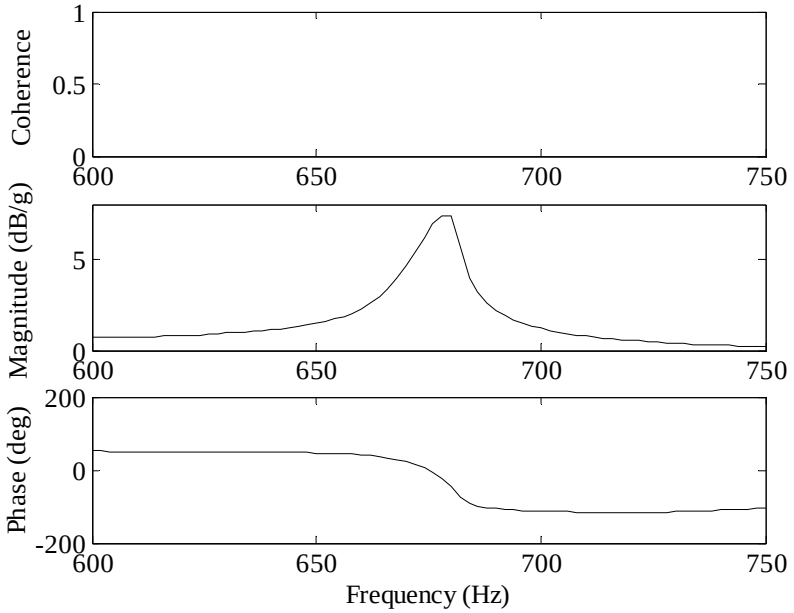

Figure 79. Frequency response plot of solar cell specimen 23 over the narrowband range of 600-750 Hz; experimental run number 33.

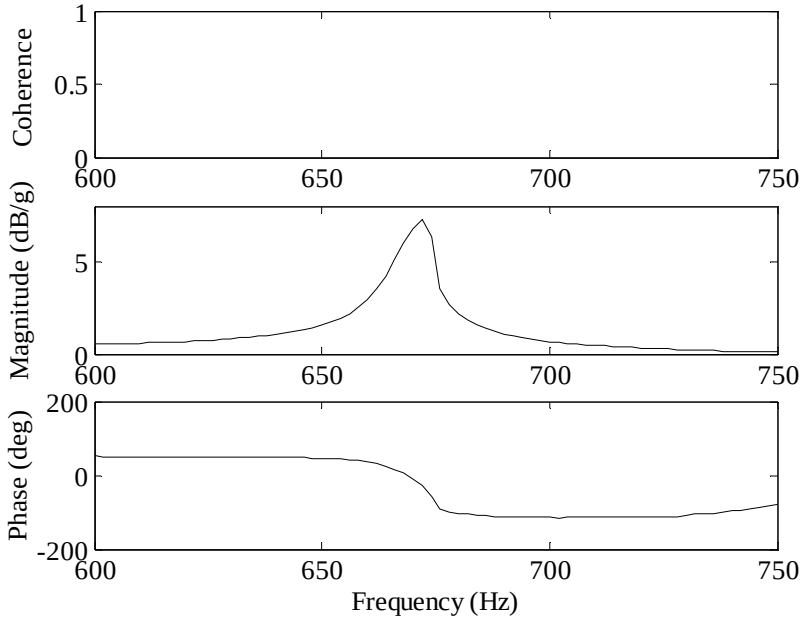

Figure 80. Frequency response plot of solar cell specimen 24 over the narrowband range of 600-750 Hz; experimental run number 34.

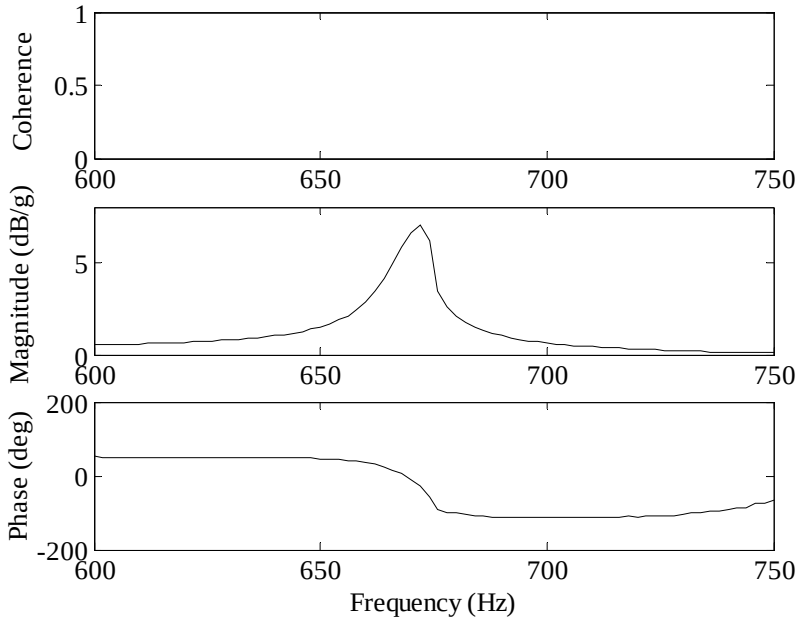

Figure 81. Frequency response plot of solar cell specimen 24 over the narrowband range of 600-750 Hz; experimental run number 35.

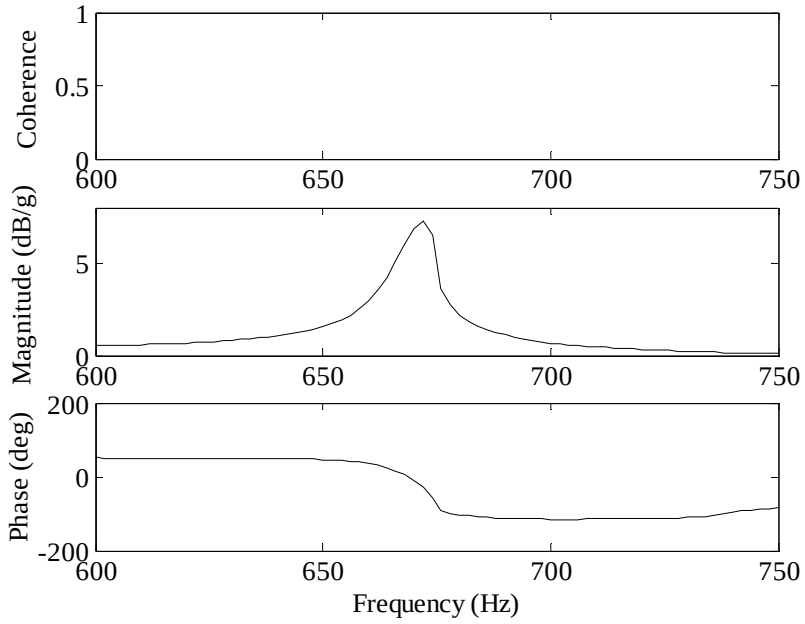

Figure 82. Frequency response plot of solar cell specimen 24 over the narrowband range of 600-750 Hz; experimental run number 36.

APPENDIX H: FREQUENCY RESPONSE PLOTS OF SOLAR CELL SPECIMENS OVER THE NARROWBAND RANGE OF 1200-1450 HZ

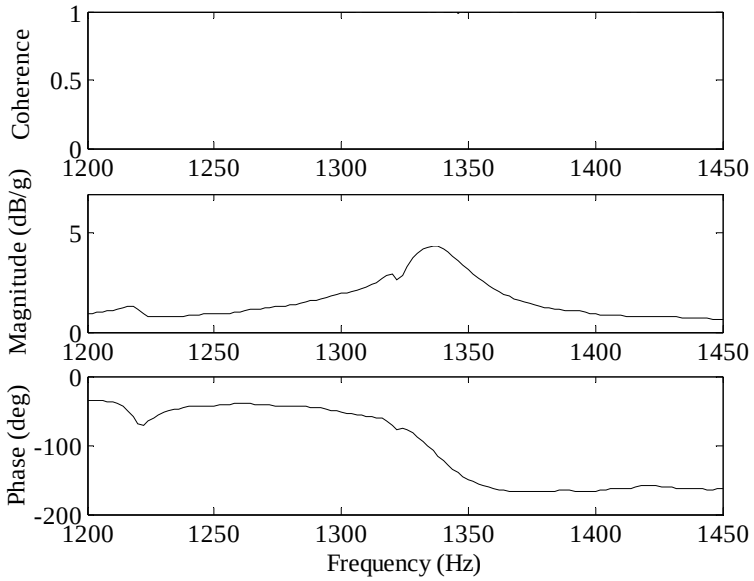

Figure 83. Frequency response plot of solar cell specimen 13 over the narrowband range of 1200-1450 Hz; experimental run number 1.

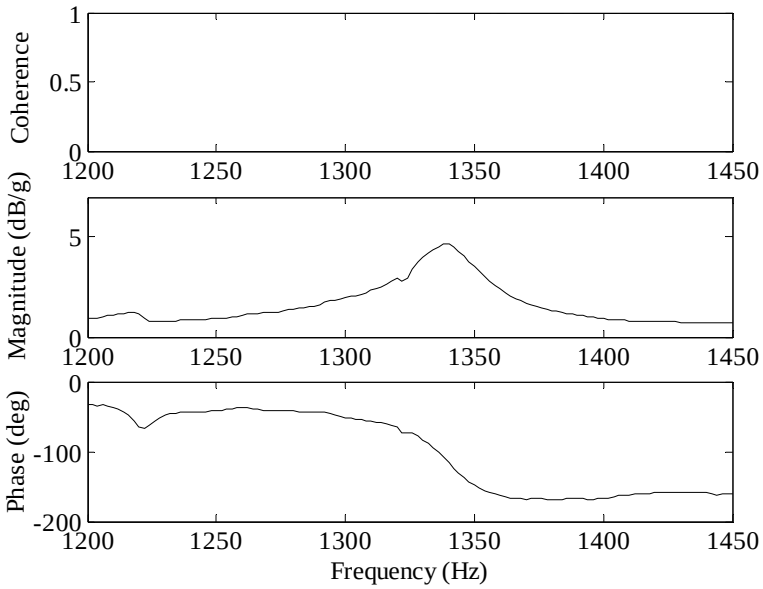

Figure 84. Frequency response plot of solar cell specimen 13 over the narrowband range of 1200-1450 Hz; experimental run number 2.

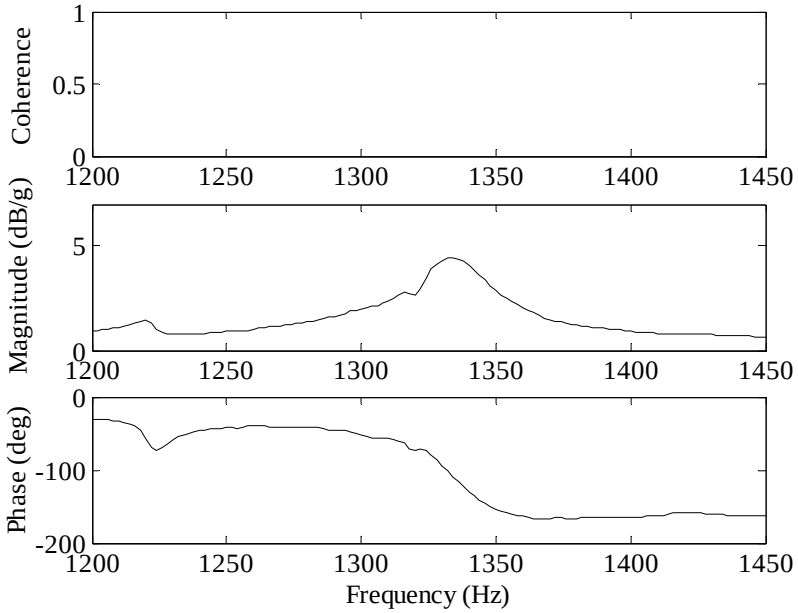

Figure 85. Frequency response plot of solar cell specimen 13 over the narrowband range of 1200-1450 Hz; experimental run number 3.

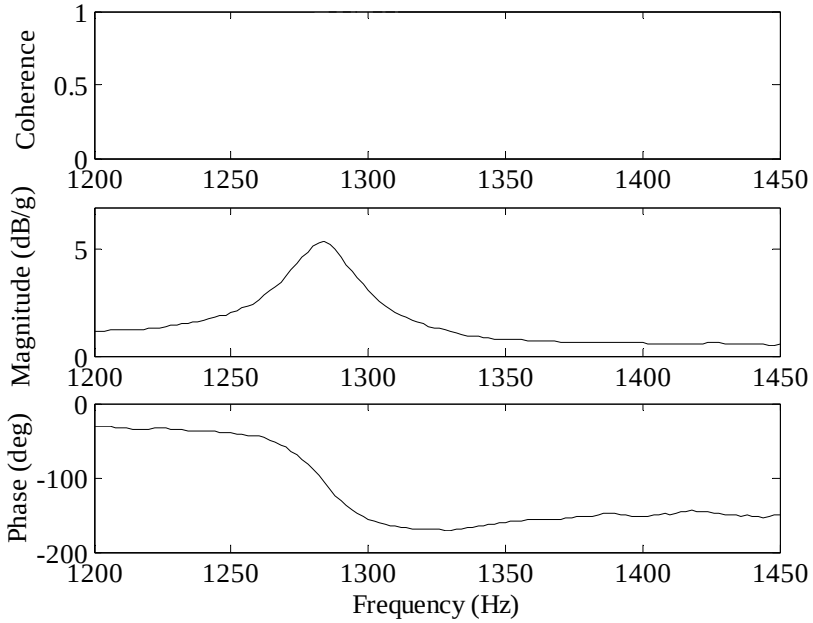

Figure 86. Frequency response plot of solar cell specimen 14 over the narrowband range of 1200-1450 Hz; experimental run number 4.

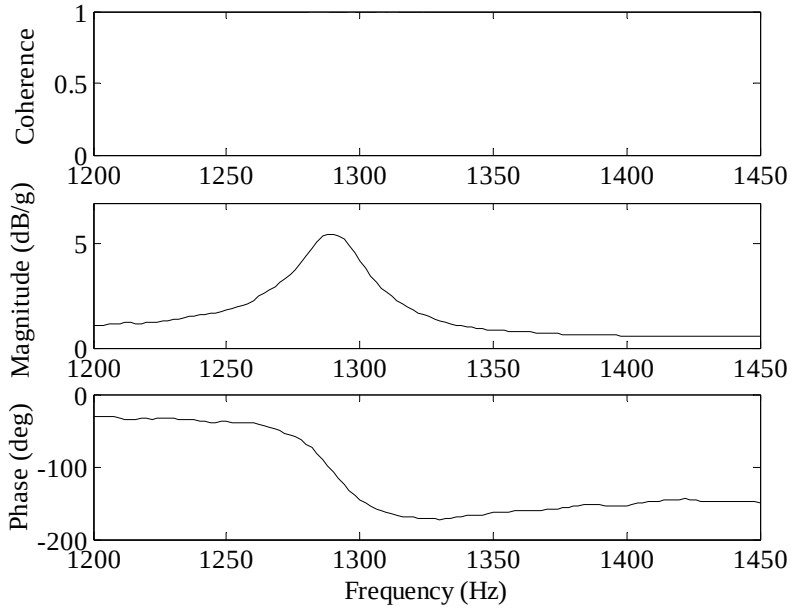

Figure 87. Frequency response plot of solar cell specimen 14 over the narrowband range of 1200-1450 Hz; experimental run number 5.

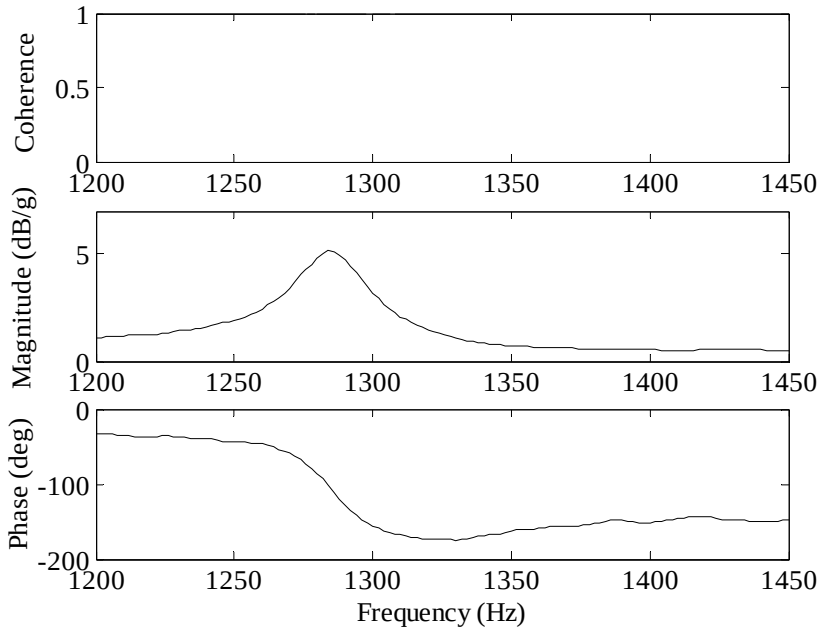

Figure 88. Frequency response plot of solar cell specimen 14 over the narrowband range of 1200-1450 Hz; experimental run number 6.

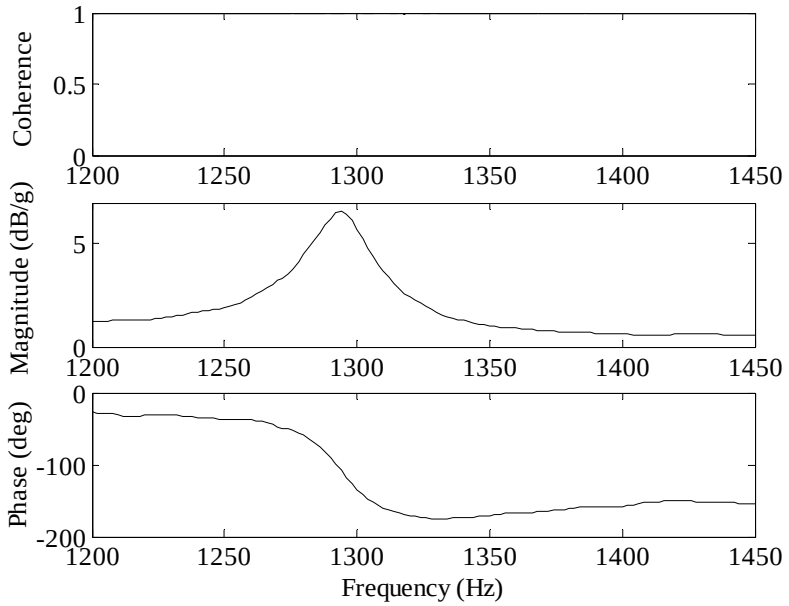

Figure 89. Frequency response plot of solar cell specimen 15 over the narrowband range of 1200-1450 Hz; experimental run number 7.

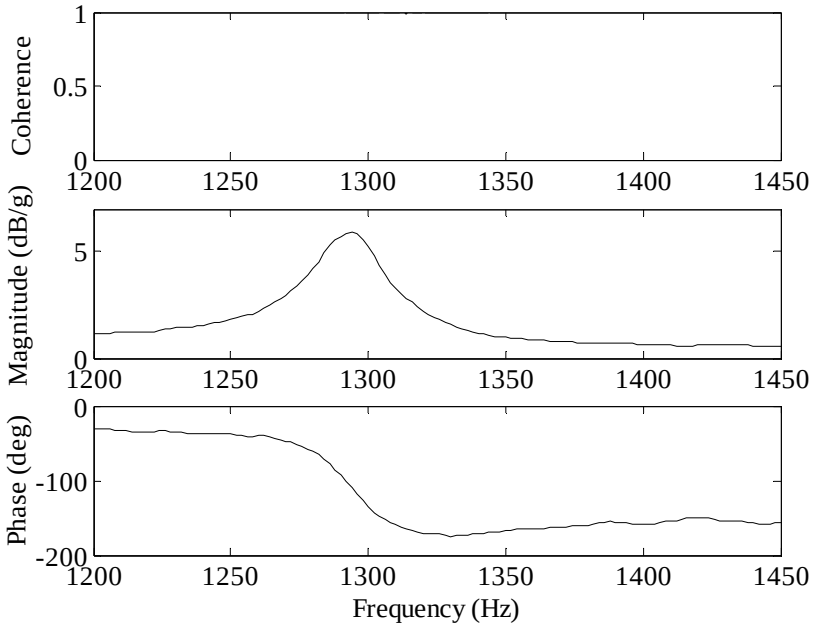

Figure 90. Frequency response plot of solar cell specimen 15 over the narrowband range of 1200-1450 Hz; experimental run number 8.

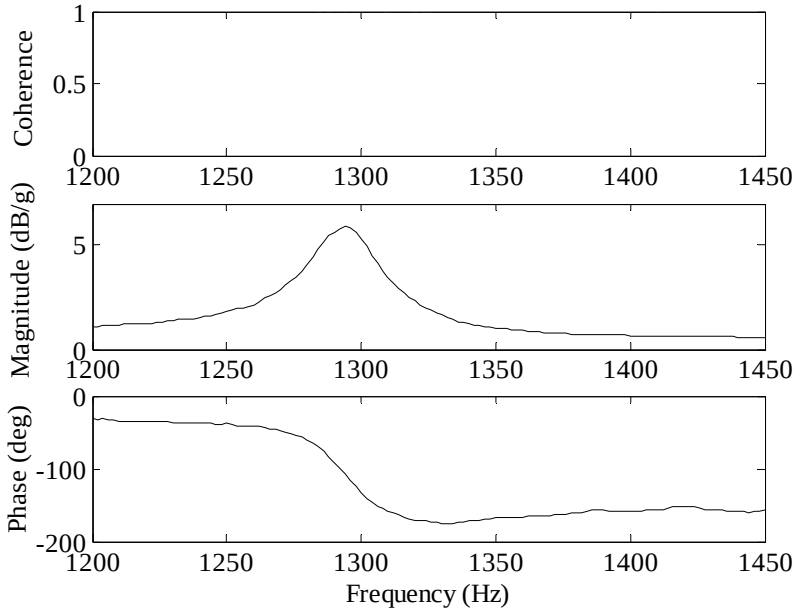

Figure 91. Frequency response plot of solar cell specimen 15 over the narrowband range of 1200-1450 Hz; experimental run number 9.

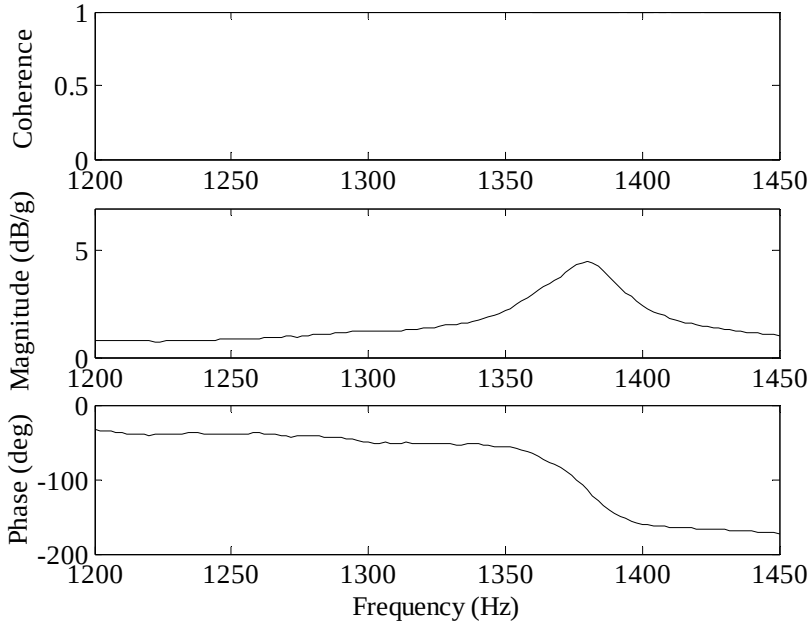

Figure 92. Frequency response plot of solar cell specimen 16 over the narrowband range of 1200-1450 Hz; experimental run number 10.

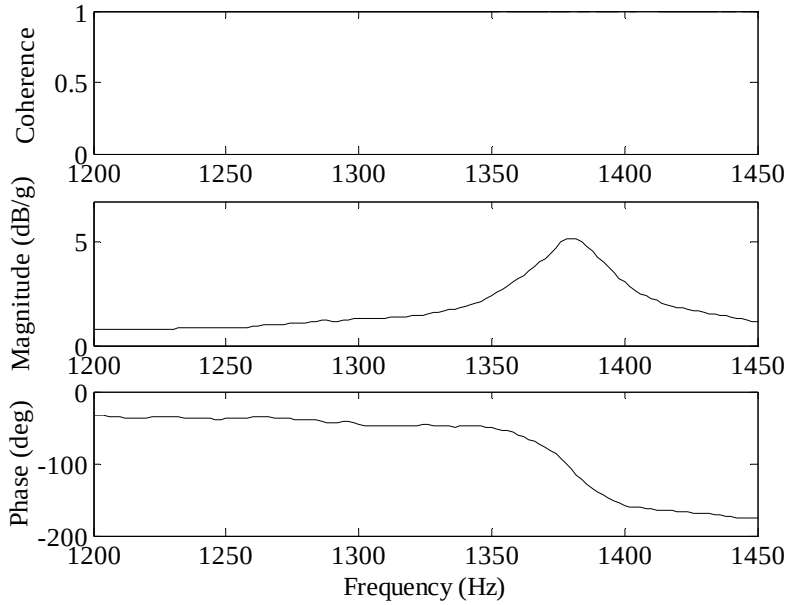

Figure 93. Frequency response plot of solar cell specimen 16 over the narrowband range of 1200-1450 Hz; experimental run number 11.

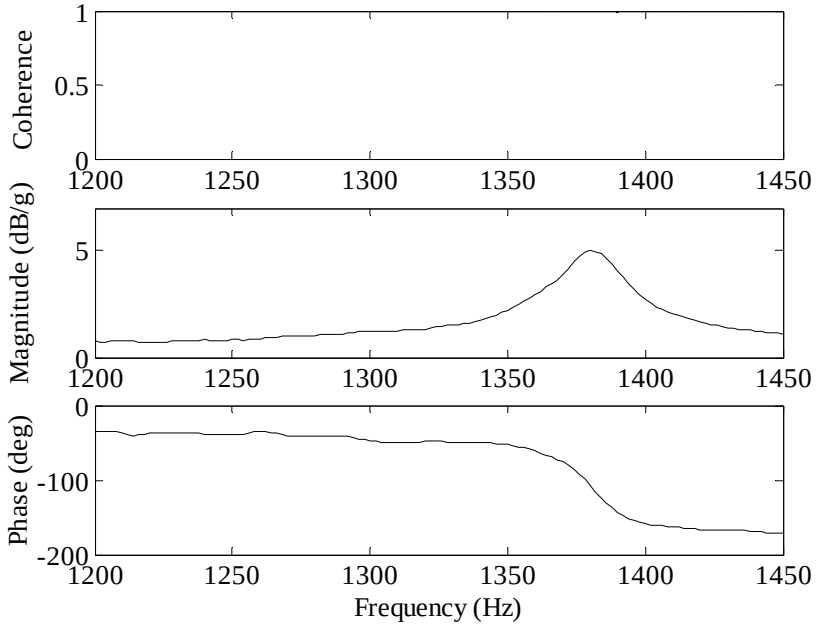

Figure 94. Frequency response plot of solar cell specimen 16 over the narrowband range of 1200-1450 Hz; experimental run number 12.

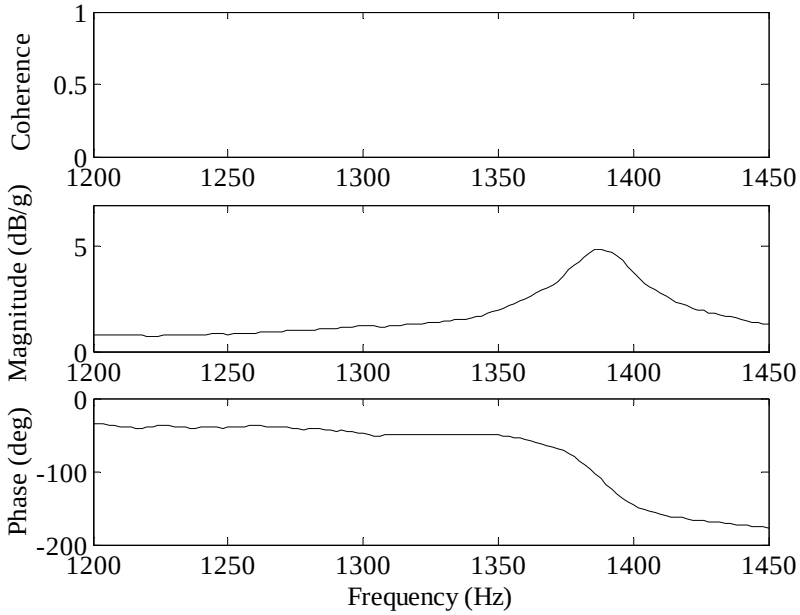

Figure 95. Frequency response plot of solar cell specimen 17 over the narrowband range of 1200-1450 Hz; experimental run number 13.

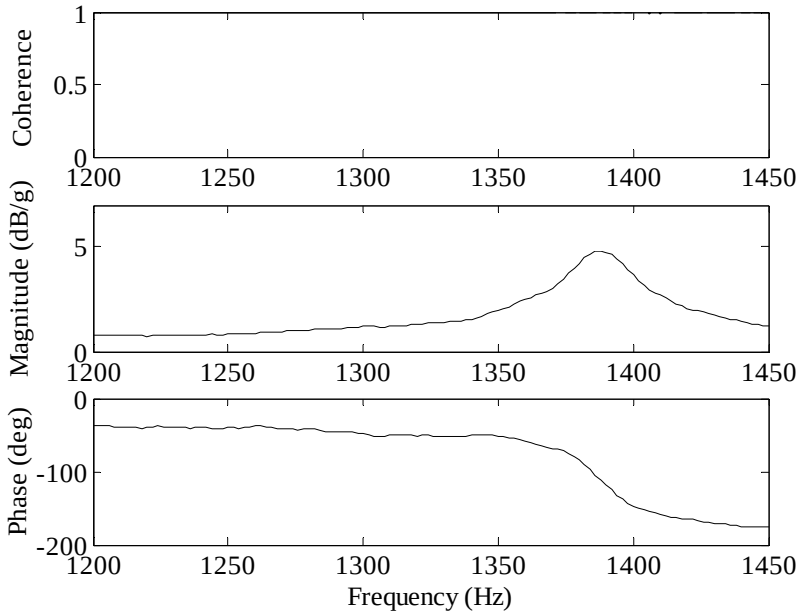

Figure 96. Frequency response plot of solar cell specimen 17 over the narrow-band range of 1200-1450 Hz; experimental run number 14.

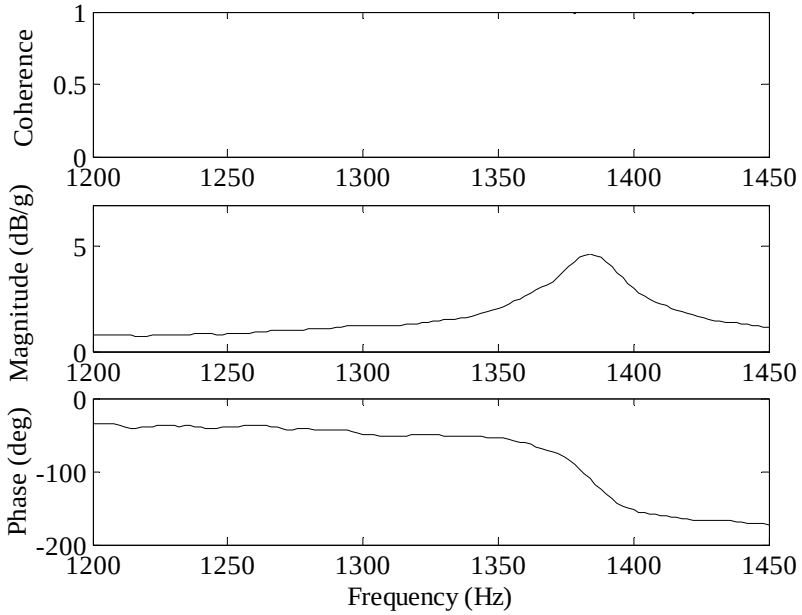

Figure 97. Frequency response plot of solar cell specimen 17 over the narrowband range of 1200-1450 Hz; experimental run number 15.

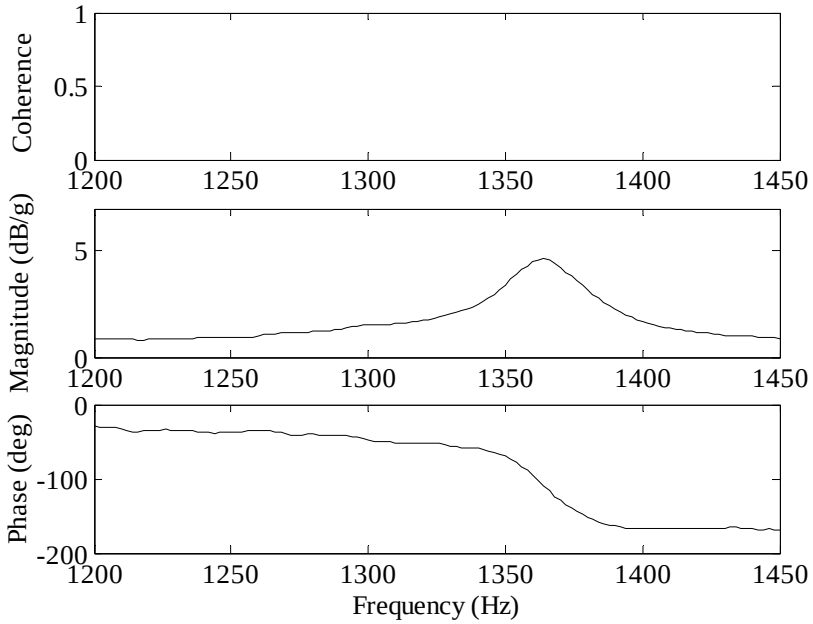

Figure 98. Frequency response plot of solar cell specimen 18 over the narrowband range of 1200-1450 Hz; experimental run number 16.

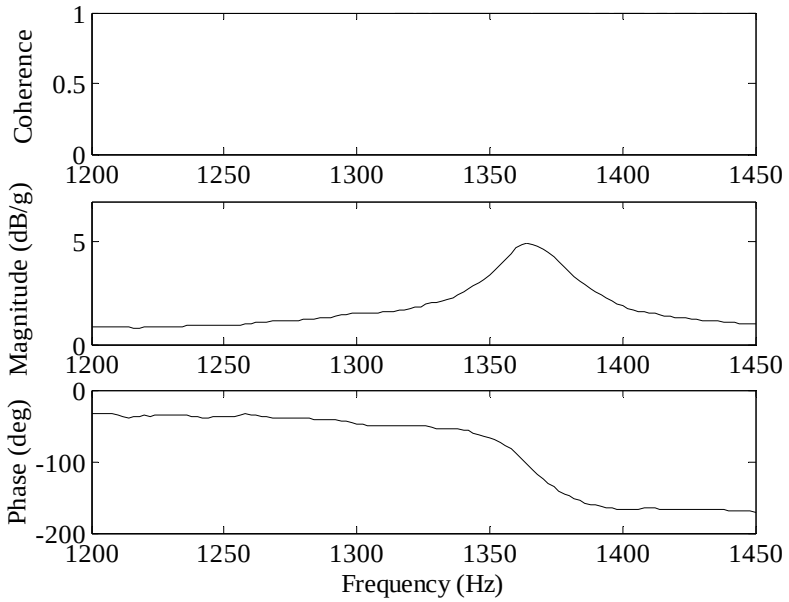

Figure 99. Frequency response plot of solar cell specimen 18 over the narrowband range of 1200-1450 Hz; experimental run number 17.

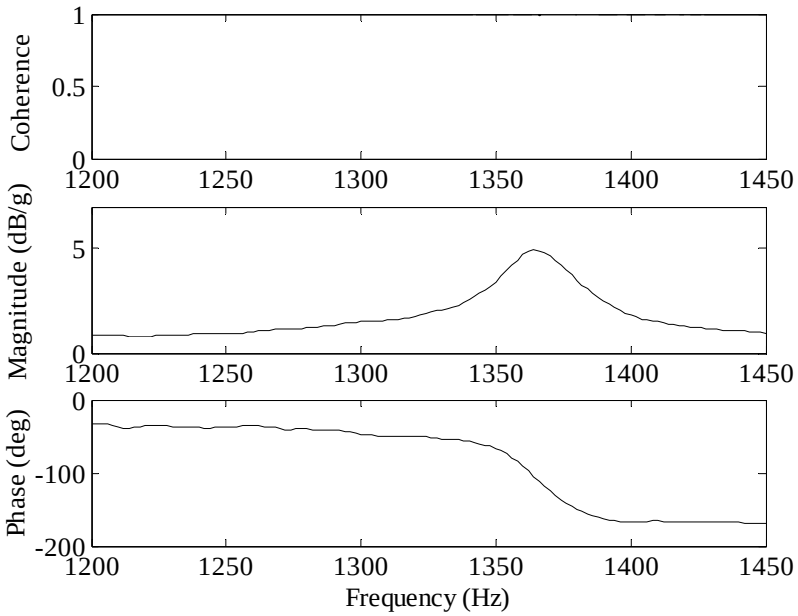

Figure 100. Frequency response plot of solar cell specimen 18 over the narrowband range of 1200-1450 Hz; experimental run number 18.

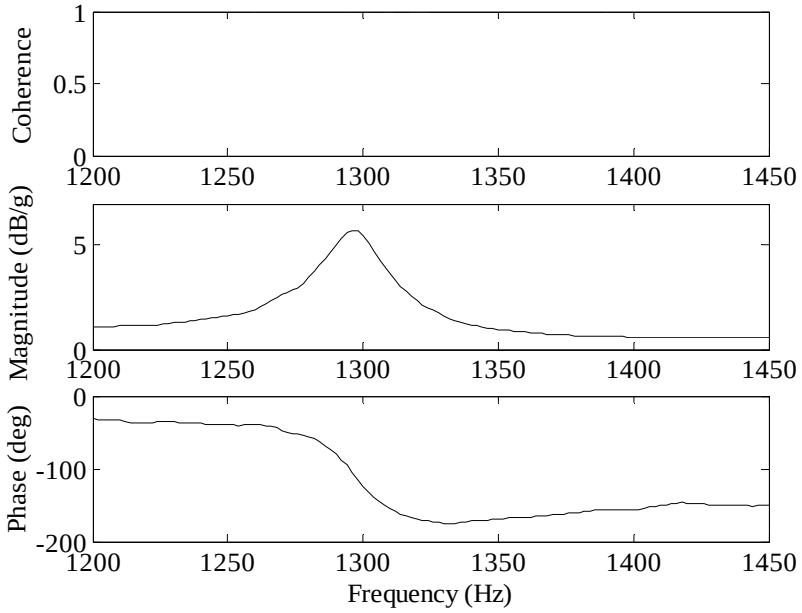

Figure 101. Frequency response plot of solar cell specimen 19 over the narrowband range of 1200-1450 Hz; experimental run number 19.

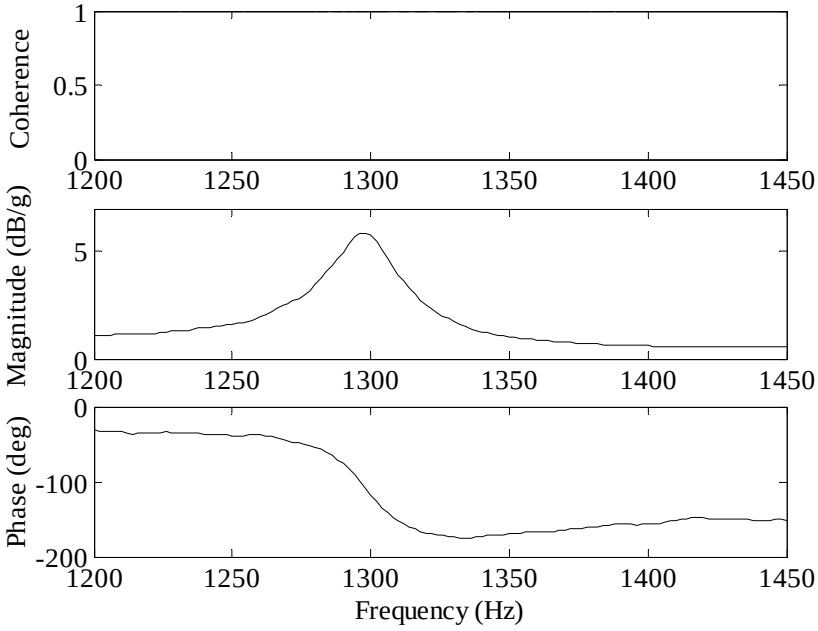

Figure 102. Frequency response plot of solar cell specimen 19 over the narrowband range of 1200-1450 Hz; experimental run number 20.

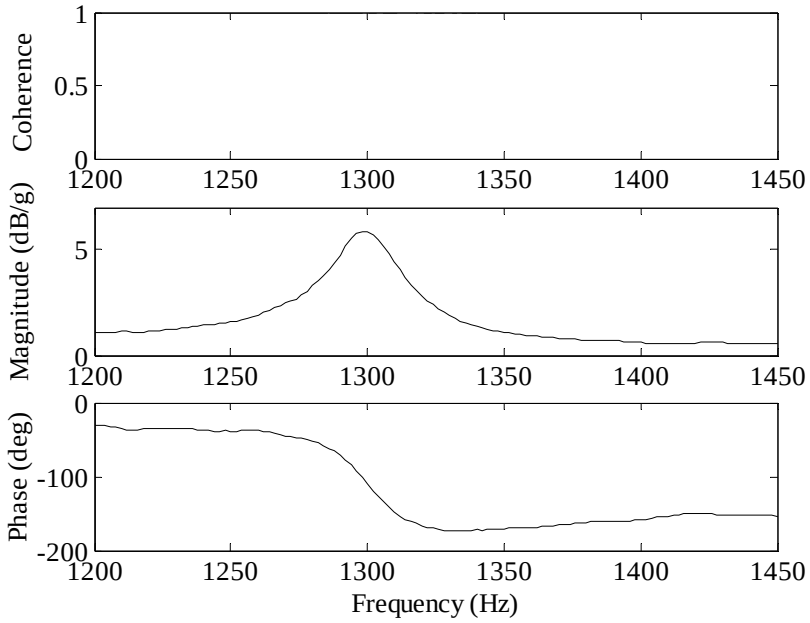

Figure 103. Frequency response plot of solar cell specimen 19 over the narrowband range of 1200-1450 Hz; experimental run number 21.

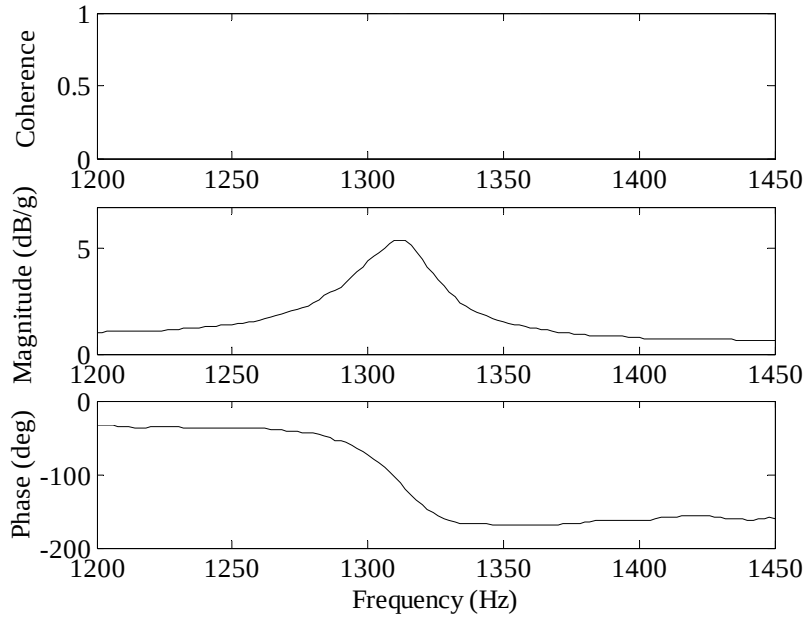

Figure 104. Frequency response plot of solar cell specimen 20 over the narrowband range of 1200-1450 Hz; experimental run number 22.

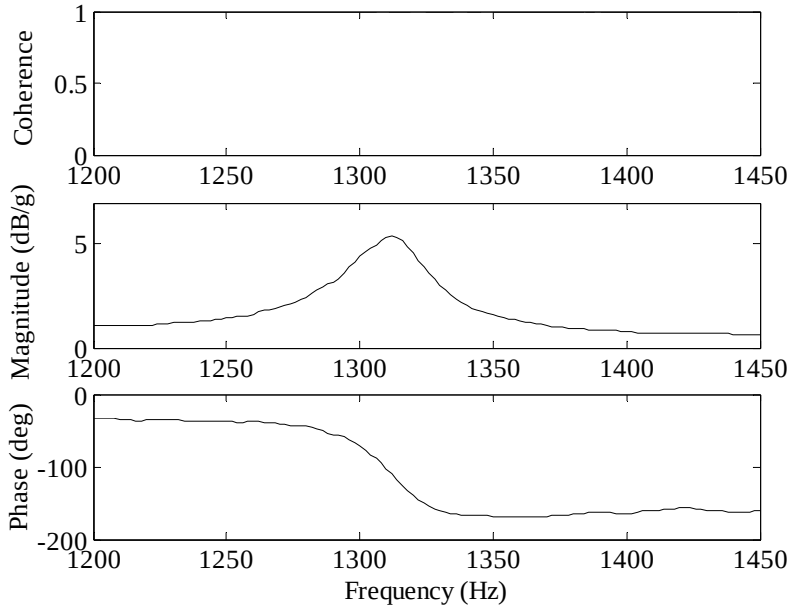

Figure 105. Frequency response plot of solar cell specimen 20 over the narrowband range of 1200-1450 Hz; experimental run number 23.

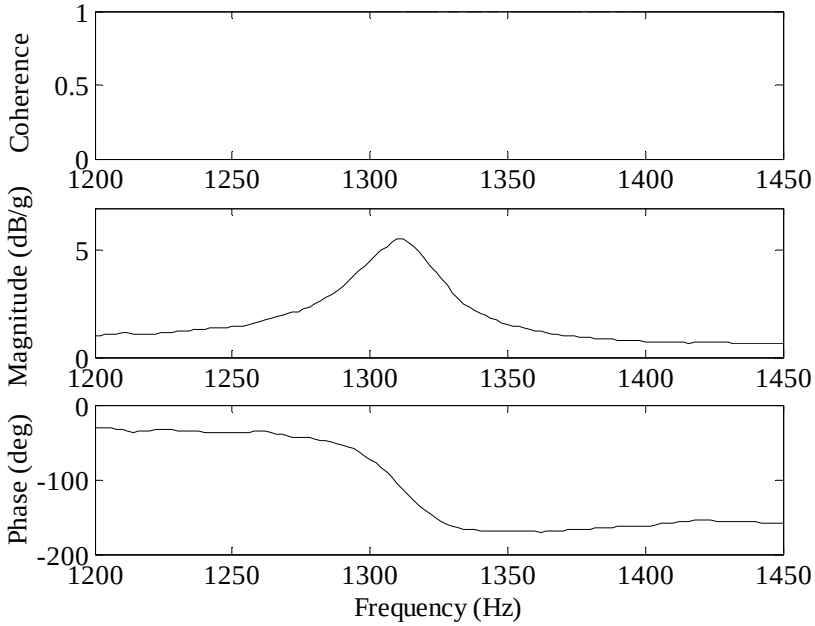

Figure 106. Frequency response plot of solar cell specimen 20 over the narrowband range of 1200-1450 Hz; experimental run number 24.

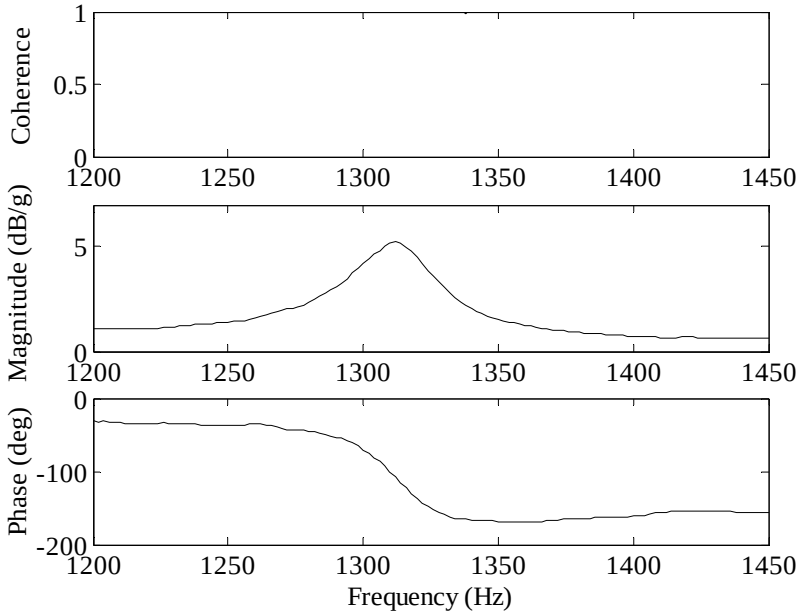

Figure 107. Frequency response plot of solar cell specimen 21 over the narrowband range of 1200-1450 Hz; experimental run number 25.

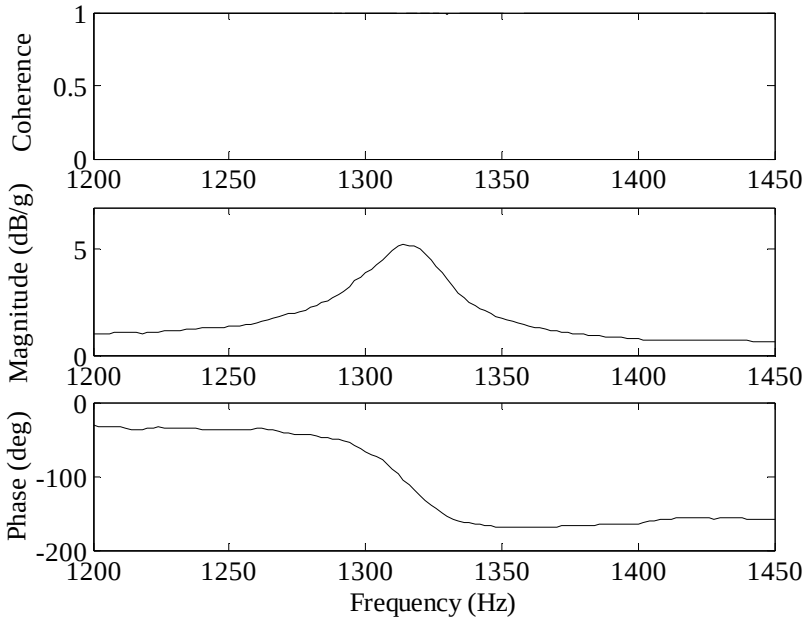

Figure 108. Frequency response plot of solar cell specimen 21 over the narrowband range of 1200-1450 Hz; experimental run number 26.

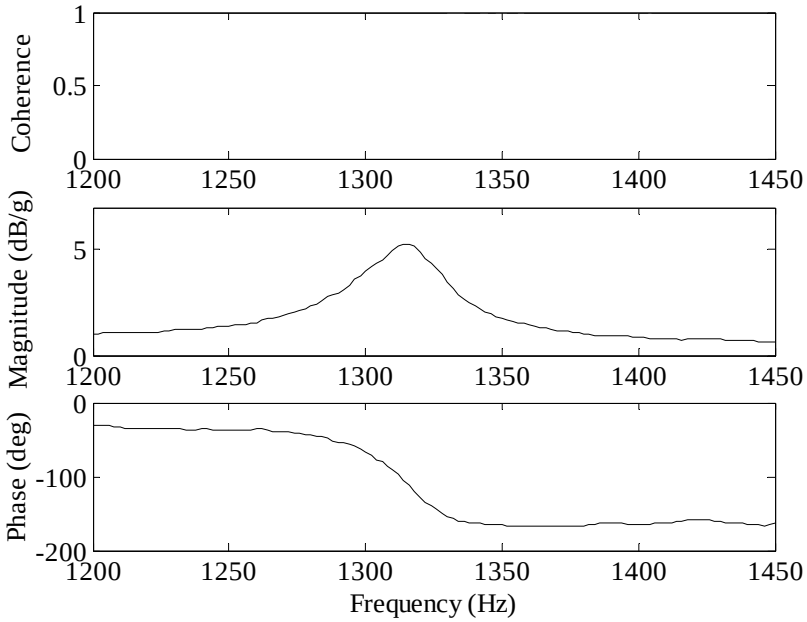

Figure 109. Frequency response plot of solar cell specimen 21 over the narrowband range of 1200-1450 Hz; experimental run number 27.

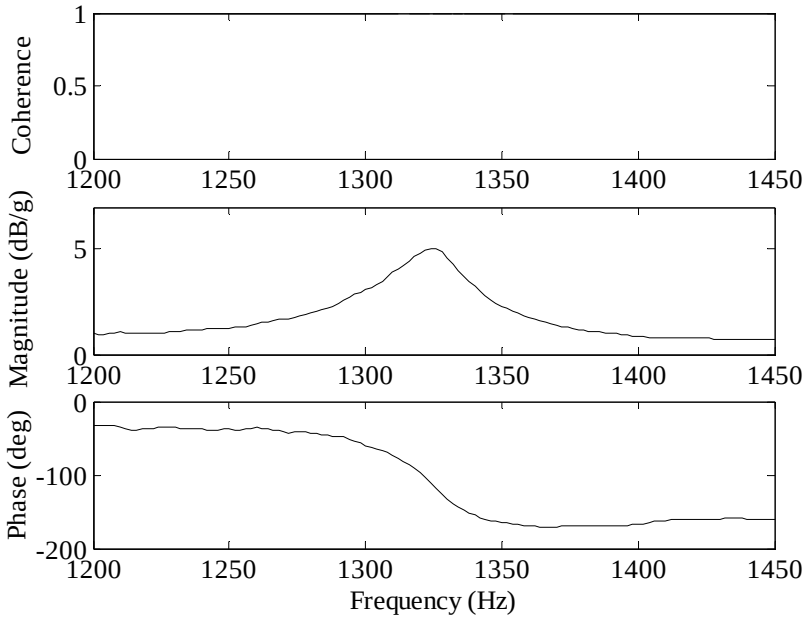

Figure 110. Frequency response plot of solar cell specimen 22 over the narrowband range of 1200-1450 Hz; experimental run number 28.

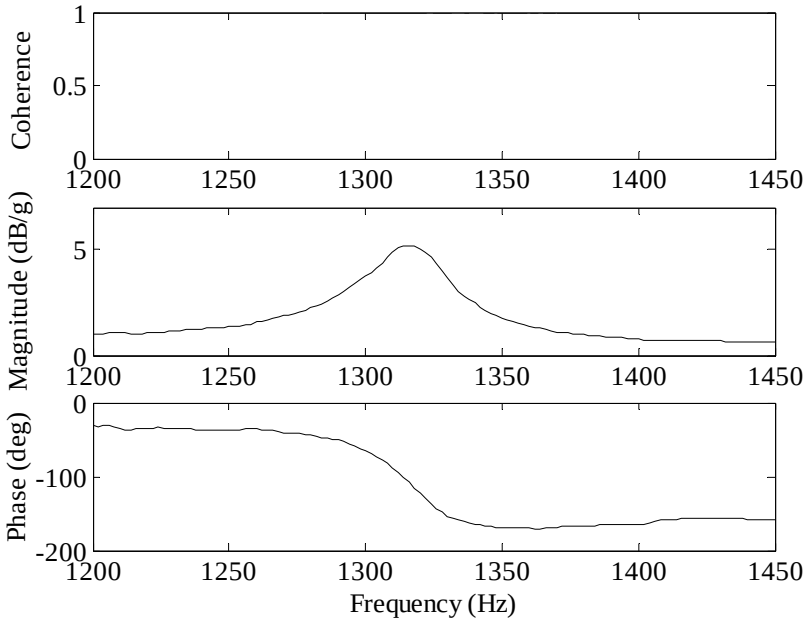

Figure 111. Frequency response plot of solar cell specimen 22 over the narrowband range of 1200-1450 Hz; experimental run number 29.

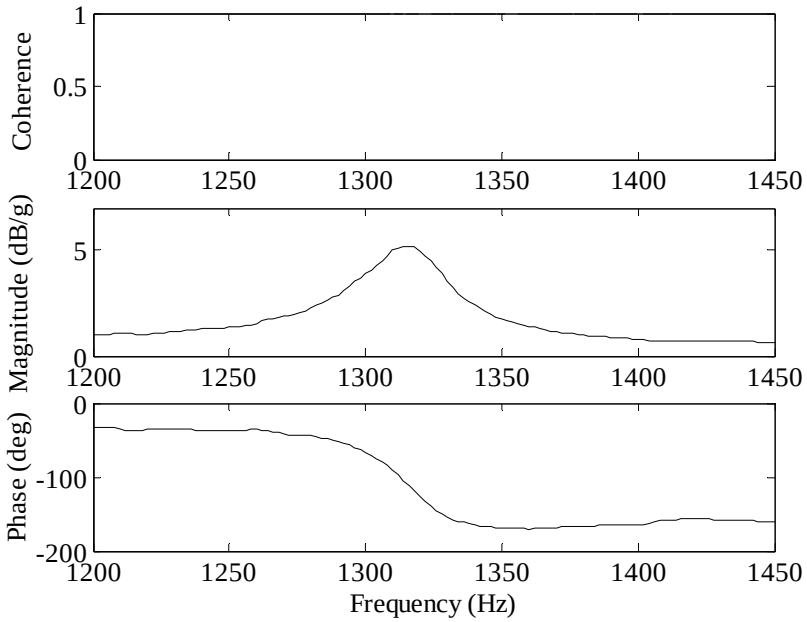

Figure 112. Frequency response plot of solar cell specimen 22 over the narrowband range of 1200-1450 Hz; experimental run number 30.

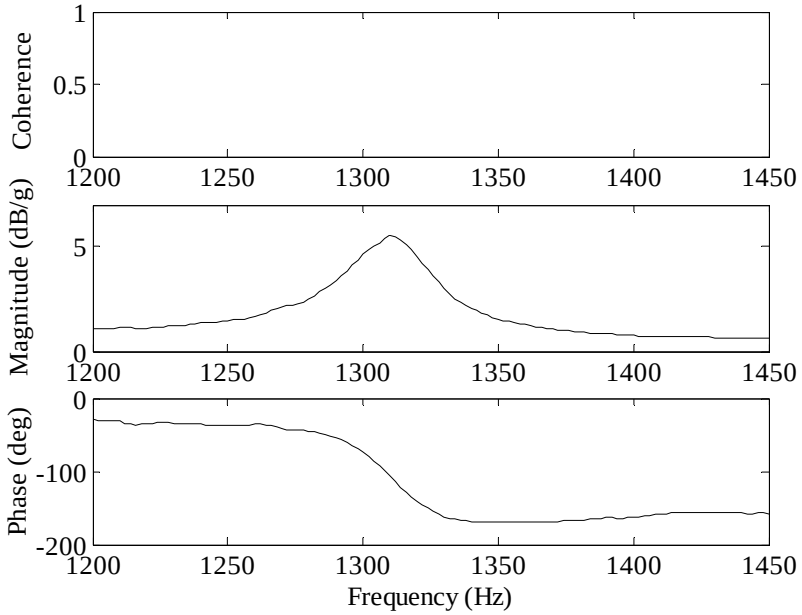

Figure 113. Frequency response plot of solar cell specimen 23 over the narrowband range of 1200-1450 Hz; experimental run number 31.

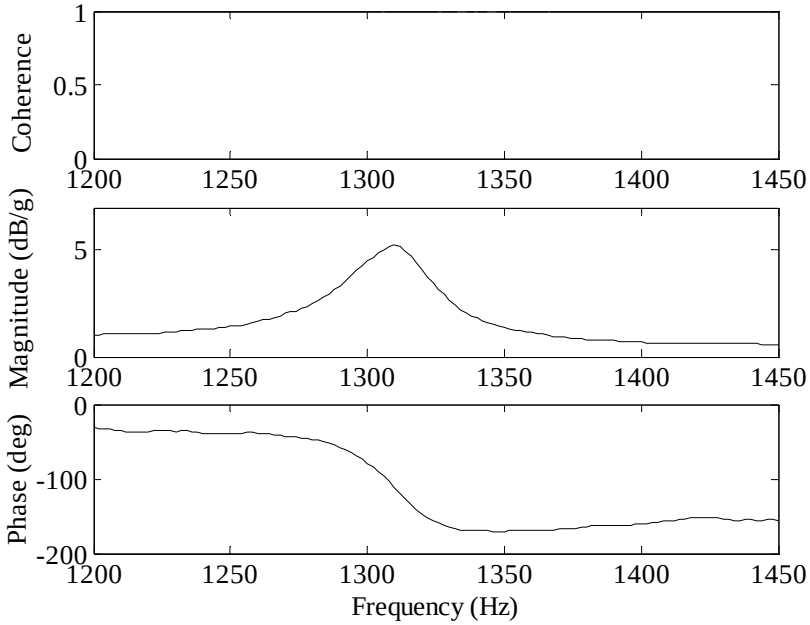

Figure 114. Frequency response plot of solar cell specimen 23 over the narrowband range of 1200-1450 Hz; experimental run number 32.

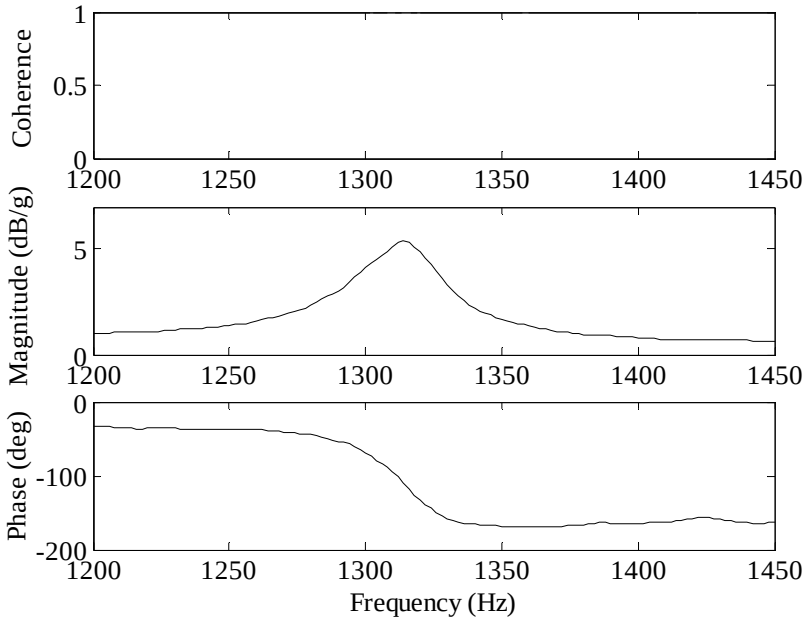

Figure 115. Frequency response plot of solar cell specimen 23 over the narrowband range of 1200-1450 Hz; experimental run number 33.

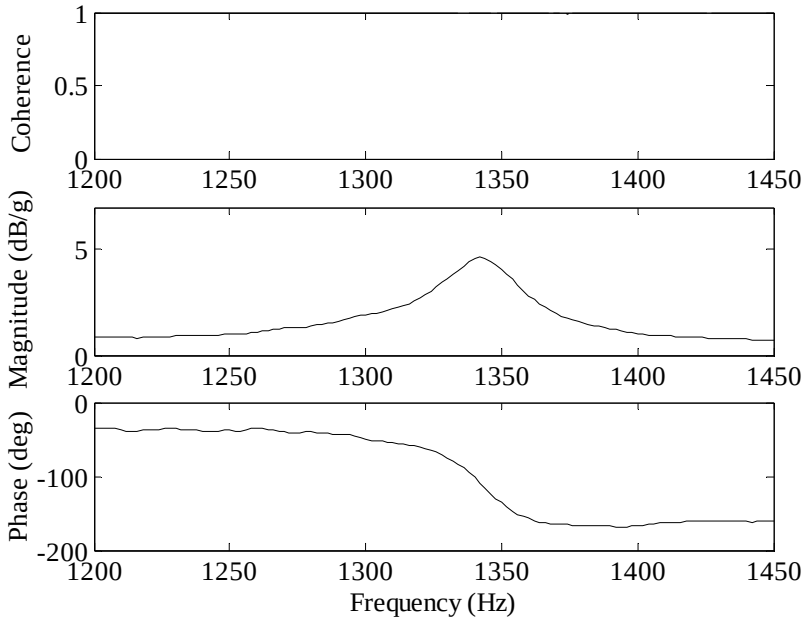

Figure 116. Frequency response plot of solar cell specimen 24 over the narrowband range of 1200-1450 Hz; experimental run number 34.

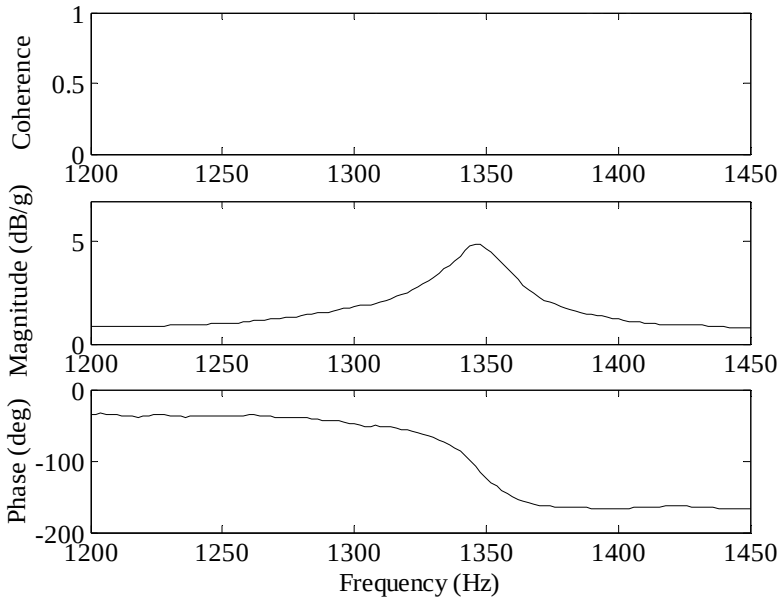

Figure 117. Frequency response plot of solar cell specimen 24 over the narrowband range of 1200-1450 Hz; experimental run number 35.

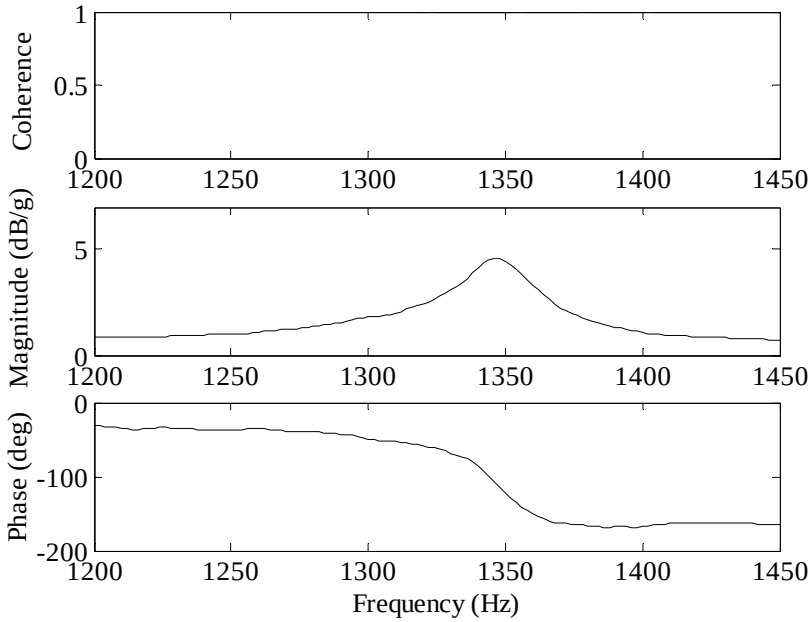

Figure 118. Frequency response plot of solar cell specimen 24 over the narrowband range of 1200-1450 Hz; experimental run number 36.